ABSTRACT

A NEAR-INFRARED FILTER SYSTEM AND STUDY OF SOLAR UMBRAL DOTS AT 1.56 μm

by
Jingshan Wang

The observations of solar magnetic fields are very important because they influence events on the sun. Almost all of magnetographs in the world work in the visible wavelength and they are powerful instruments for measuring strong magnetic fields (above 1000 Gauss) on the sun. To measure the weak solar magnetic fields (below 1000 Gauss), a new filter system (magnetograph) working in near-IR wavelength has been developed in this work. This system includes an interference prefilter (FWHM ~ 40Å), a liquid crystal magnetic analyzer, a near-IR birefringent filter (FWHM ~ 2.5Å), a near-IR Fabry-Perot filter (FWHM ~ 0.12Å), a near-IR InGaAs camera and an image processing computer. The most important part in this system is the near-IR birefringent filter. A new method of wavelength tuning is developed with combination of calcite and liquid crystal variable retarder. The liquid crystal variable retarder is the wavelength tunable device in every element of the filter. This is the first original design for a tunable Lyot birefringent filter in near-IR wavelengths. The optical design and test results of this near-IR birefringent filter are presented in this dissertation.

The birefringent index of calcite in the near-IR range, $\mu = n_e - n_o$, is a critical parameter in the design of the birefringent filter. The values of μ in the literature have been found to be unreliable in the near-IR range. A new method is developed to accurately measure the birefringent indices from 1.0 to 1.65 μm using sunlight as the light source, a spectrograph as spectrum analyzer and the InGaAs camera as the detector.

The temperature coefficient of μat 1.56 μm is also measured. The value of μat 1.56 μm was used in the design of the near-IR birefringent filter and the filter specifications are found to be satisfactory.

The optical components including the four pairs of calcite and the half waveplates have been tested. The results show that the optical components satisfy the specifications of the filter system. The basic theory of a Fabry-Perot filter is presented and the test procedures of the near-IR Fabry-Perot filter, ET70FS-104, are also considered.

In this dissertation, the first observations and studies of umbral dots at 1.56 μm are made. The image data are obtained with a 50Å wide interference filter centered at 1.56μm with the near-infrared InGaAs camera as the detector. The image data include two sequences of images of a complicated sunspot and a simple sunspot. The dynamic motion properties of umbral dots are studied from the movies of the two sunspots. From the data analysis, the contrast distribution, size distribution and lifetime of umbral dots are presented.

A NEAR-INFRARED FILTER SYSTEM AND STUDY OF SOLAR UMBRAL DOTS AT 1.56 μm

by
Jingshan Wang

A Dissertation
Submitted to the Faculty of
New Jersey Institute of Technology and
Rutgers, The State University of New Jersey - Newark
In Partial Fulfillment of Requirement for the Degree of
Doctor of Philosophy in Applied Physics

Federated Department of Physics

May 2001

APPROVAL PAGE

A NEAR-INFRARED FILTER SYSTEM AND STUDY OF SOLAR UMBRAL DOTS AT 1.56 μm

Jingshan Wang

Dr. Haimin Wang, Dissertation Advisor — Date
Professor of Physics, NJIT

Dr. Nuggehalli M. Ravindra, Committee Member — Date
Professor of Physics, NJIT

Dr. Philip R. Goode, Committee Member — Date
Professor of Physics, NJIT

Dr. Dale E. Gary, Committee Member — Date
Associate Professor of Physics, NJIT

Dr. Ken K. Chin, Committee Member — Date
Professor of Physics, NJIT

Dr. Zhen Wu, Committee Member — Date
Associate Professor of Physics, Rutgers University, Newark

BIOGRAPHICAL SKETCH

Author: Jingshan Wang

Degree: Doctor of Philosophy

Date: May 2001

Undergraduate and Graduate Education:

- Doctor of Philosophy in Applied Physics,
  New Jersey Institute of Technology, Newark, NJ, 2001
- Master of Science in Physics,
  Peking University, Beijing, P. R. China, 1987
- Bachelor of Science in Physics,
  Shandong Normal University, Jinan, P. R. China, 1984

Major: Applied Physics

Presentations and Publications:

Jingshan Wang, Haimin Wang, Thomas J. Spirock, Chik-yin Lee, N. M. Ravindra, Jun Ma, Philip R. Goode and Carsten Denker,
"Optical Design of a Near-Infrared Birefringent Filter System and Measurement of Birefringent Index of Calcite at 1.56μm", Optical Engineering, vol. **40**, no. 6, 2001, in press.

Jingshan Wang, Haimin Wang, Thomas J. Spirock, Chik-yin Lee, N. M. Ravindra, Jun Ma, Philip R. Goode and Carsten Denker,
"Optical Design of a Near-Infrared Birefringent Filter System and Measurement on Birefringent Index of Calcite at 1.56μm", Proceedings of SPIE's 45th Annual Meeting, vol. **4093B**, pp. 481-489, 2000.

Jingshan Wang, Haimin Wang, Carsten Denker, Thomas J. Spirock, Philip R. Goode,
"Study of Umbral Dots at 1.56 Micron", 194th Meeting of the American Astronomical Society, #93.04, Chicago, May, 1999.

Thomas J. Spirock, Carsten Denker, Jingshan Wang, Hangjun Chen, Haimin Wang and Philip R. Goode,
"New vectormagnetographs at the Big Bear Solar Observatory", 194th Meeting of the American Astronomical Society, #76.07, Chicago, May, 1999.

Jingshan Wang, Haimin Wang, Nuggehalli M. Ravindra, Philip R. Goode, Feiming Tong, Shu Yang and T. Spirock,
"Solar Near-Infrared Filter System", AGU Spring Meeting, SH21C-03, Boston, May, 1998.

Yuanyong Deng, Guoxiang Ai and Jingshan Wang,
"Inhomogeneous distribution of brightness in the split-element filter (Technical Note)", Applied optics, vol. **36**, pp. 1576, 1997.

Jingshan Wang, Guoxiang Ai, Guofeng Song, Bin Zhang, Xiangming Ye, Yingpin Nie, Tzihong Chieveh, Weanshun Tsay and Huanshin Li,
"Universal Birefringent Filter with a New Double Passband Mode", Solar Physics, vol. **161**, pp. 229-239, 1995.

Jingshan Wang, Guoxiang Ai, Fengbao He, Yuanyong Deng, Weijun Mao, Guofeng Song, Bin Zhang and Xiangming Ye,
"Solar Multichannel Birefringent Filter", Optical Technology, Supplement, pp. 41-65, 1995.

Jingshan Wang and Shangwu Qian,
"Gauge Invariance Transition Probability Amplitudes of a Time-dependent Harmonic Oscillator in Magnetic Dipole Approximation", Acta Scientiarum Naturalium, Universitatis Pekinensis, vol. **30**, pp. 347, 1994.

Jingshan Wang, Guoxiang Ai and Yuanyong Deng,
"Supplementary Retardation of the Total Reflection Prism in Multichannel Birefringent Filter", Publ. Beijing Astr. Obs., vol. **24**, pp. 191, 1994.

Jingshan Wang, Guoxiang Ai and Guofeng Song,
"Wavelength-tunable Apparatus in Equal Fourier Coefficient Birefringent Filter", Proceedings of Chongqing Solar Physics Workshop, China, pp. 200, 1993.

Jingshan Wang, Guoxiang Ai, Guofeng Song
"Universal Birefringent Filter", Proceedings of Chongqing Solar Physics Workshop, China, pp. 209, 1993.

Jingshan Wang and Guoxiang Ai,
"High Quality PVA Plastic Achromatic Waveplate", Proceedings of Chongqing Solar Physics Workshop, China, pp. 225, 1993.

Yuanyong Deng, Guoxiang Ai and Jingshan Wang,
"The Development of High Quality Crystal Achromatic Waveplate", Acta Astrophysica Sinica, vol. **13**, pp. 283, 1993.

Yuanyong Deng, Guoxiang Ai and Jingshan Wang,
"The Disadvantage of Evans Filter's Field of View", Acta Astromica Sinica, vol. **34**, pp. 38, 1993.

Yuanyong Deng, Guoxiang Ai and Jingshan Wang,
"10cm Full Disc Magnetic Field Telescope", Frontiers of Astronomy in 1990s, Beijing, China, pp. 198, 1993.

Yang Liu, Guofeng Song, Jingshan Wang and Jingxiu Wang,
"A Study of Data Obtained a Full Disc Magnetograph", Acta Astrophysica Sinica, vol. **14**, pp. 191, 1994.

Guofeng Song, Guoxiang Ai and Jingshan Wang,
"HeI (10830Å) Solar Magnetic Field Observing System",Proceedings of Chongqing Solar Physics Workshop, China, pp. 238, 1993.

Guofeng Song, Guoxiang Ai and Jingshan Wang,
"Mechanical Design of the Universal Birefringent Filter",Proceedings of Chongqing Solar Physics Workshop, China, pp. 246, 1993.

Yang Liu, Guofeng Song, Jingshan Wang and Jingxiu Wang,
"Preliminary Reduction of Data Obtained with a Full Disc Magnetograph", Proceedings of Kofu Symposium, Kofu, pp. 413, 1993.

Jingshan Wang, Guoxiang Ai and Yuanyong Deng,
"Determination of the Crystal Elements' Orientation Arrangement in Wavelength-tunable Birefringent Filter", Acta Astrophysica Sinica, vol. **11**, pp. 383, 1991.

Jingshan Wanga and Guoxiang Ai,
"9-Channel Birefringent Filter", The First China-Soviet Union Solar Physics Workshop, Irkusk, USSR, May, 1991.

Shangwu Qian, Hu Yeteng and Jingshan Wang,
"Time-dependent Harmonic Oscillators in an Electromagnetic Field", J. of Phys. A: Math. Gen., vol. **20**, pp. 2833, 1987.

Shangwu Qian, Huang Xiangyou and Jingshan Wang,
"Double Wave Description of a Single Relativistic Free Electron", J. of Phys. A: Math. Gen., vol. **19**, pp. L849, 1986.

This dissertation is dedicated
to my beloved family

ACKNOWLEDGMENT

I wish to express my deepest appreciation to my advisor, Professor Haimin Wang, for his great guidance, friendship, and moral support throughout the whole research project. Without his support I could never complete this hard research project. I would like to thank Professor Nuggehalli M. Ravindra, for his support, helpful suggestions, careful review of the dissertation and encouragement.

Special thanks to the other members of committee: Dr. Philip R. Goode, Dr. Dale E. Gary, Dr. Ken K. Chin and Dr. Zhen Wu for their helpful comments.

I would like to thank Thomas J. Spirock for the electronic control system in the test and measurement instrument, data acquisition of umbral dots and other helpful suggestions. I would also like to thank Dr. Chik-Yin Lee for the productive discussions about the measurement of birefringent index of calcite, Jun Ma for the mechanical design of the heat insulation container.

I am grateful to the staff of the Big Bear Solar Observatory for their support and suggestions during the measurement and observations, especially Jeff Nenow, Randy Fear, Bill Marquette and Owen Phairis. I would also thank Dr. Jong Qiu, Shu Yang and other fellow students for helpful discussions during the study.

Finally, I would like to thank my parents and my family for their continuous support, encouragement and best wishes that were very important to pursue my doctoral study.

This work was supported partially by NASA SRT program (NAG5-9682), NSF Solar-Terretrial program (ATM-9628862), Airforce Office for Scientific Research, and New Jersey Commission on Science and Technology (NJCST).

TABLE OF CONTENTS

TABLE OF CONTENTS
(Continued)

Chapter **Page**

LIST OF TABLES

LIST OF FIGURES

LIST OF FIGURES
(Continued)

Figure **Page**

LIST OF FIGURES
(Continued)

Figure **Page**

LIST OF FIGURES
(Continued)

LIST OF FIGURES
(Continued)

CHAPTER 1

INTRODUCTION

The sun is a star that is extremely important for us because it provides light and energy, for life on Earth. There are a lot of physical phenomena occurring on the sun, such as, solar flares, sunspots, prominences, etc, in active regions and quiet regions. The sudden occurrence of some of these kinds of phenomena may very much affect us. For example, when a large solar flare occurs on the sun, a huge number of highly energy particles emitted from the sun will arrive to the earth; and power systems, radio and satellite communications may be interrupted in some areas in the world. On the other hand, the sun is the nearest star to us and hence it is the only star that we can observe in detail. Research studies of the sun can provide much information that can be useful for studies of other stars. Therefore, the sun could be called " a laboratory for astrophysics"[1]. Thus, solar observations and studies in solar physics are very important, not only for predicting solar events and avoiding any damage to our technological society, but also for astronomical research.

Solar magnetic fields are fundamentally important for many solar events. One of the methods to measure solar magnetic fields uses the Zeeman effect. According to the Zeeman effect, the splitting of solar spectral lines, $\Delta\lambda$, which is due to the solar magnetic field, is proportional to $g\lambda^2 B$, where, λ is the wavelength of the Zeeman sensitive line, g is the Lande factor of the line and B is the magnetic field strength. Usually, large sunspots possess strong magnetic fields - on the order of 2000 to 3000 Gauss. However, in other solar features, such as plages, the magnetic fields are only about 1000 to 1500 Gauss, and there exist weak, sub-kilogauss, fields in other structures, such as the intranetwor

magnetic fields[2]. The Zeeman splitting induced by a sub-kilogauss field is too small to be measured[3-4] in the visible spectrum. For example, if $\lambda = 5250.2$Å (with $g = 3.0$) and $B = 1000$G, then the splitting is given by $\Delta\lambda = 4.7\times10^{-13}\, g\lambda^2 B \cong 0.039$Å.

However, for a near infrared line, e.g., FeI15648.5Å (with $g = 3.0$), the Zeeman splitting $\Delta\lambda$ ($\propto g\lambda^2 B$) would be much larger for the same magnetic field strength, ~ 0.35Å. The Zeeman splitting of an infrared line is almost ten times as great as that of a visible line for a given B field. Therefore, weaker magnetic field strengths can be more precisely measured using near infrared lines.

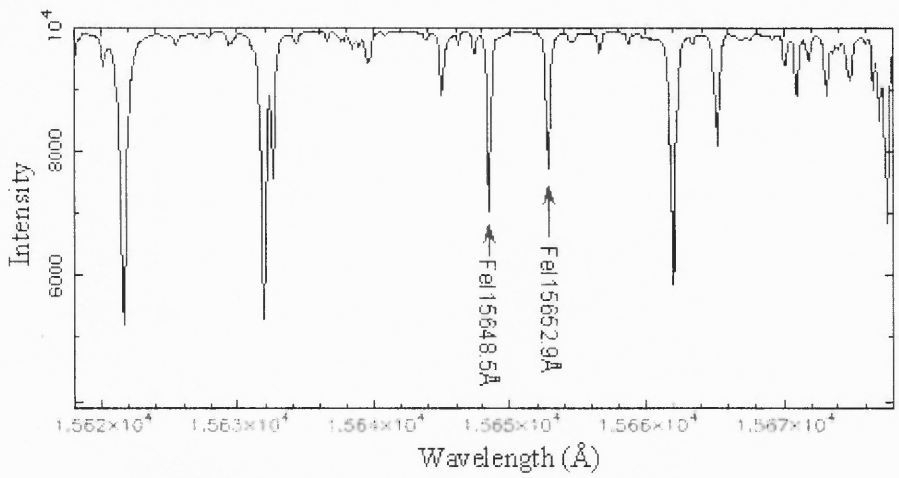

Figure 1.1 The absorption spectral lines near 15648.5Å.

It has been shown that one can measure magnetic field strengths as low as 100 Gauss by using the line ratio between FeI15648.5Å and FeI15652.9Å lines[3]. Fig. 1.1 shows the absorption lines near FeI15648.5Å. FeI15648.5Å (e^7D_1 - $3d^64s5p^7D_1^0$) is a Zeeman triplet with a Lande factor g of 3 and the strongest spectral line in the H-band. FeI15652.9 Å (f^7D_5 - $(9/2)[7/2]_4^0$) has a Lande factor g of 1.53 and corresponds to a weaker spectral transmission. The use of infrared lines as probes of solar magnetic

features has been discussed in detail by Solanki, et al.[5]. Therefore, FeI15648.5Å and FeI15652.9Å are suitable lines for a near-infrared filter system to measure weaker solar magnetic fields.

On the other hand, the electromagnetic radiation from the sun interacts with matter in the atmosphere outside the earth. This means that only in certain wavelength regions, the electromagnetic radiation can penetrate the atmosphere and reach to the surface of the earth. Figure 1.2 shows the amount of absorption at different wavelengths in the atmosphere. It is presented in terms of the half-absorption altitude, which is defined to be the altitude in the atmosphere (measured from the Earth's surface) where 1/2 of the radiation of a given wavelength incident on the upper atmosphere has been absorbed.

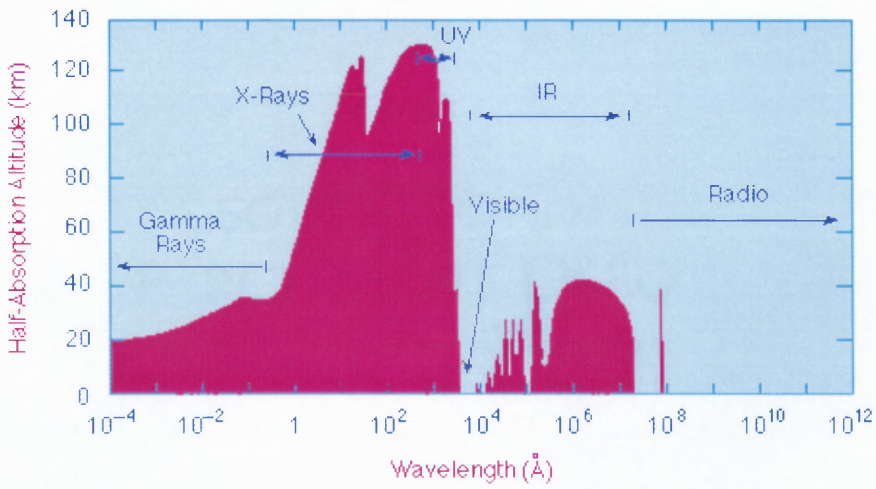

Figure 1.2 Atmospheric windows of the electromagnetic radiation from the sun.

The dominant transparent windows in the atmosphere are seen in the visible, near infrared and radio frequency regions. Meanwhile X-Rays and UV are seen to be very strongly absorbed and Gamma Rays and far IR are somewhat less strongly absorbed. This

is why the ground-base solar instruments work well in the visible, near-infrared and radio wavelength regions, while the observations at ultraviolet and X-rays (hard and soft X-rays) have to be done in space. So the other advantage of the near-infrared solar observations is that it has a good atmospheric window.

A near-IR filter system (magnetograph) is developed at the Big Bear Solar Observatory (BBSO), New Jersey Institute of technology (NJIT). This system is designed to obtain the chromatic images of the sun and measure the solar magnetic fields at the magnetic sensitive FeI15648.5Å and FeI15652.9Å. Because this system is wavelength tunable, Stokes profiles can be obtained using wavelength scanning. In this dissertation, this near-IR filter system is discussed in detail in Chapter 2. It includes:

(1) Introduction (section 2.1) --- a review of the solar optical instrumentation (section 2.1.1) and the principle of a birefringent filter (section 2.1.2);

(2) Measurement of the birefringent index of calcite in near-IR spectral range (100μm to 1.65μm) (section 2.2);

(3) Optical design of the near-IR birefringent filter (section 2.3);

(4) Discussion of the near-IR Fabry-Perot filter (section 2.4).

In Chapter 3, umbral dots at 1.56μm in the active regions NOAA 8485 and NOAA 8489 are studied. The data were obtained in March, 1999, with a near-IR InGaAs camera and a 50Å interference filter. The contrast distribution, size distribution and lifetime of umbral dots in these active regions are analyzed.

CHAPTER 2

A NEAR INFRARED FILTER SYSTEM

2.1 Introduction

2.1.1 Evolution of the Solar Optical Instrumentation

In the literature, the sun has been studied for a long time. Eclipses were probably first "recorded" prior to 1948 B. C., and telescopic observations of the sun's surface began around 1610 due to the invention of telescopes. At about that time the sunspots were systematically observed, by Galileo, Fabricius, Scheiner and Harriot. With the telescope, scientists could describe the sun's appearance, watch the movement of sunspots, and measure the sun's rotation. Telescopes consist of two kinds: refractive and reflective. An important parameter of a telescope is the limit of diffraction resolution[6]:

$$\theta \approx \frac{1.22\lambda}{\phi}, \tag{2.1}$$

where, θ is the angular separation of two distant objects that could be seen clearly, ϕ is the diameter of the primary lens or mirror of the telescope and λ is the wavelength of light. For example, if the diameter of a telescope is 10 inches (25.4cm) for light near the center of visible range (λ ~ 560nm), the theoretical diffraction limit of resolution is given by:

$$\theta \approx \frac{1.22\times 5.6\times 10^{-5} cm}{25.4 cm} \approx 2.69\times 10^{-6}, \tag{2.2}$$

or, in arc seconds,

$$\theta \sim 0.55''. \tag{2.3}$$

For near-IR wavelength, for example, λ = 1560nm, the theoretical diffraction limit of resolution is:

$$\theta \approx \frac{1.22 \times 1.56 \times 10^{-4} cm}{25.4 cm} \approx 7.49 \times 10^{-6}, \tag{2.4}$$

or, in arc seconds,

$$\theta \sim 1.54''. \tag{2.5}$$

From the results in Eqs. 2.3 and 2.5, the diameter of the primary lens or mirror of the telescope should be larger if higher resolution observations for near-IR light are needed.

Figure 2.1 is a simple scheme of a refractive telescope[7]. Light enters from the left and passes through the hard (KF_3) glass element of the objective lens (1), then through the ED (extra-low dispersion) glass element (2). This two lens objective system permits the telescope to bring all visible wavelengths of light to the same focal point (3). All the components are housed in the optical tube (4). The focuser (5) moves the eyepiece through the focal point (3).

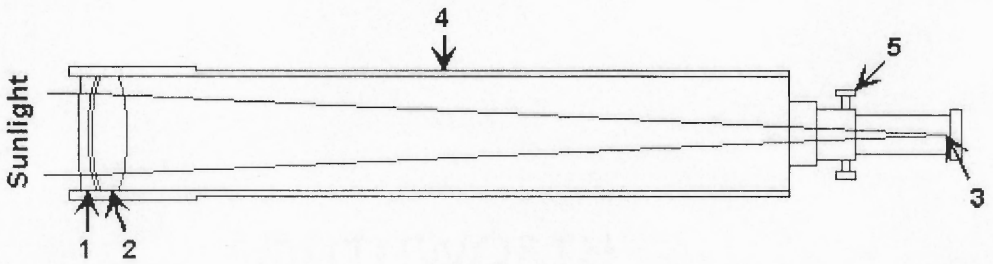

Figure 2.1 A simple scheme of a refractive telescope (Courtesy of Dave T. Runkle).

Figure 2.2 is a simple scheme of a reflective telescope[7]. Light enters from the left and passes through a correcting plate (1). This correcting plate is a thin, two-side aspheric correction lens. The corrected light passes the entire length of the optical tube to a spherical primary mirror (2) where it is reflected back up the tube to the convex (Cassegrain telescope) or concave (Gregorian telescope) secondary mirror (3).

The convex or concave secondary mirror increases the effective focal length of the primary mirror. The resulting light is returned down the scope into the primary baffle tube (4) and focuser (5) to the eyepiece set at the focal point (6) located on the end of the focuser. The primary baffle tube passes through a hole in the primary mirror.

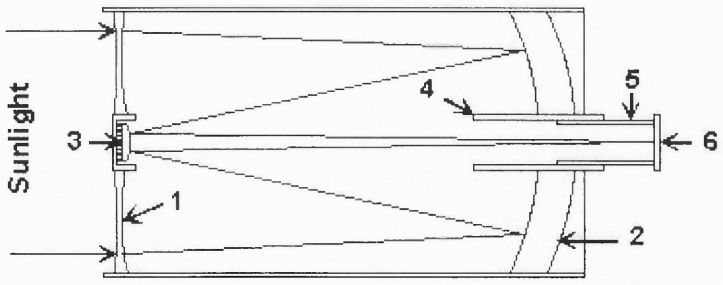

Figure 2.2 A scheme of a reflective telescope (Courtesy of Dave T. Runkle).

A reflective telescope can be constructed with a large aperture primary mirror because the tube (usually a vacuum tube) can be much shorter than the refractive telescope due to changing direction of the light propagation. The 26-inch Gregorian reflective telescope at Big Bear Solar Observatory, NJIT, is a good example of reflector. The optical scheme is shown in Fig. 2.3[8]. In this telescope, the primary mirror is mushroom-shaped for strength and lightness. A tilted cooled heat stop mirror at the first focus rejects all the light except what passes through a hole 3 arc minutes in diameter. The system is enclosed in a vacuum tube with a window. The theoretical diffraction limit of resolution of this 26-inch telescope for the near-IR light with wavelength 1.56μm can be calculated by Eq. 2.1:

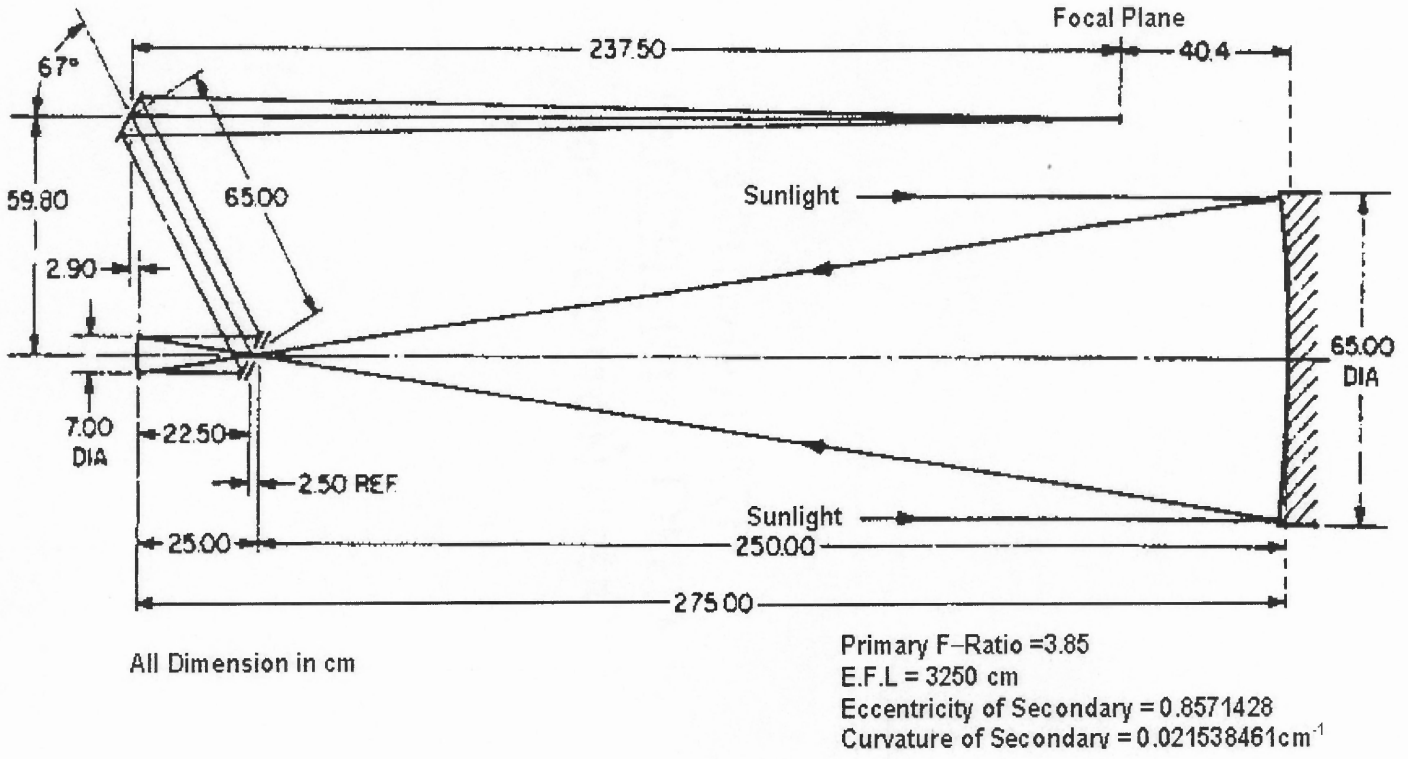

Figure 2.3 The Gregorian vacuum reflective telescope at Big Bear Solar Observatory.

$$\theta \approx \frac{1.22 \times 1.56 \times 10^{-4} cm}{26 inch \times 2.54 cm / inch} \approx 2.89 \times 10^{-6}, \tag{2.6}$$

or, in arc seconds,

$$\theta \sim 0.60''. \tag{2.7}$$

On the other hand, the primary lens of refractors is typically smaller. For example, the 10-inch and 8-inch telescopes at BBSO are refractors. The 8-inch refractive telescope is used for the solar full disk H_α observation and the 10-inch refractive telescope is utilized for observations of solar magnetic fields at λ = 6102Å.

The solar tower telescope, a special vertical telescope, was invented for use in solar studies. Its long focal length can give very large images of the sun (up to more than 30 inches in diameter). The coronagraph, another special telescope, is used to examine the sun's outer atmosphere. The instrument blocks the direct light from the sun's disk and allows its dim outer atmosphere, called the corona, to be viewed. The details of these instruments are not discussed here.

When a ray of sunlight, which appears white, passes through a prism or a diffraction grating, it spreads out into a series of colors called a spectrum. The spectrum and its fine structures are used not only to determine chemical composition of the sun as well as their abundance, location, and physical states, but also to measure solar magnetic fields using Zeeman effect. In 1814, Joseph von Fraunhofer began a thorough study of the solar spectrum. He found that it was crossed by many dark lines, now called absorption lines or Fraunhofer lines. Meanwhile, other scientists had been studying the light emitted and absorbed by elements in the gaseous state when they were heated in the laboratory. They discovered that each element always produced a set of bright emission

lines associated with that element alone. The dark solar line that Fraunhofer had called D was shown to have the same position in the spectrum as the brilliant line that sodium gave off when it was heated in the laboratory. It is now believed that the dark bands represent elements in the sun's atmosphere. The lines are dark because the elements in the sun's atmosphere absorb the bright lines given off by the same element on the sun's disk. Linking the lines of the spectrum with the elements that emit or absorb them provided a way to study the composition of the sun's surface. For the study of the spectrum, the spectrograph was invented and was used widely in many spectral analysis research areas.

For astronomical applications, the spectroheliograph was invented. It consists of a slit to limit the entering light, a collimator that makes the light diverging from the slit to a parallel collimated light, a grating to disperse this light and a camera to record the result. Various optical arrangements are used to achieve this result, depending on the goals of the particular spectrograph. In a Littrow spectrohelograph, a single lens performs the function of both a collimator and a re-imaging lens of the camera. Figure 2.4 is the optical diagram of the Littrow spectroheliograph of BBSO[8]. The slit 1 is at the focus of the Littrow lens, which produces parallel light. This light is diffracted by the grating and refocused by the lens on slit 2 where a camera is placed. An image of the slit 1 at each wavelength is produced on the slit 2. If the slit 1 is moved across the sun, images of the sun in all wavelengths are built up.

The grating diffraction formula is given by:

$$d\sin\theta = m\lambda, \tag{2.8}$$

where, d is the separation between the lines of the grating, θ is the angle of diffraction, m is the order and λ is the wavelength of the light. The inverse dispersion is the change in

wavelength, $d\lambda$, per linear interval $fd\theta$ in the focal plane (slit 2). It can be obtained from differentiating Eq. 2.8:

$$d\lambda = \frac{d}{n}\cos\theta d\theta = \lambda c \tan\theta d\theta, \tag{2.9}$$

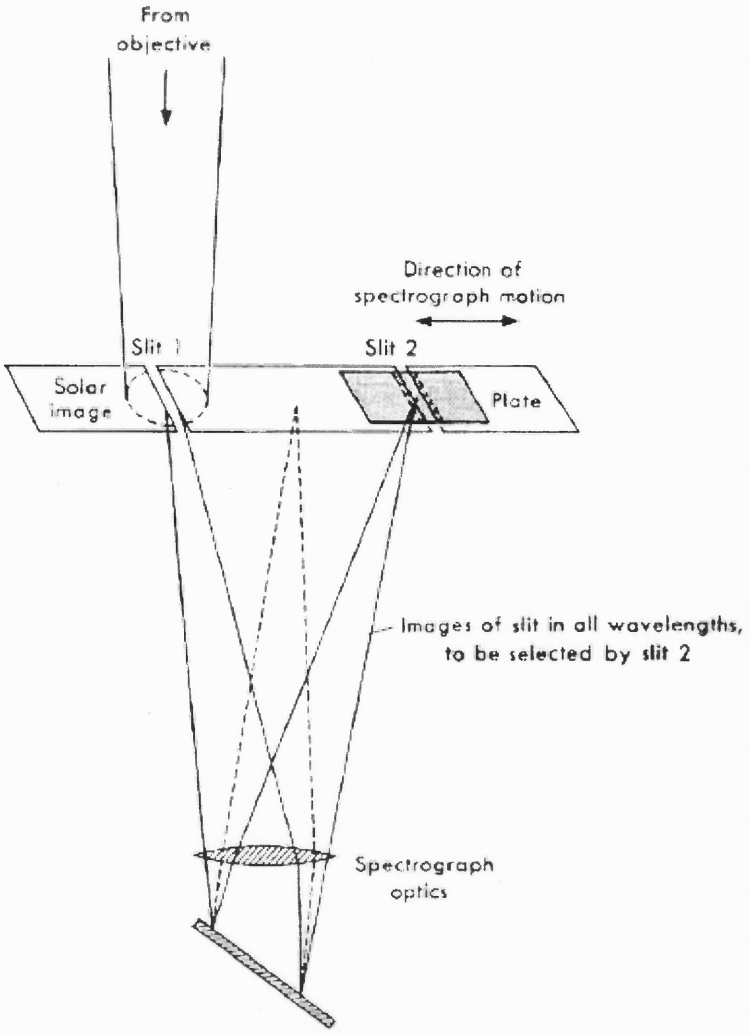

Figure 2.4 Optical diagram of the spectroheliograph of BBSO.

so the inverse dispersion (in Å/mm) is:

$$\frac{d\lambda}{fd\theta} = \frac{\lambda}{f} c \tan\theta . \tag{2.10}$$

The dispersion resolution of the spectroheliograph can be down to the order of 0.01Å. The spectroheliograph of BBSO was used for the test of calcite elements and the measurement of the birefringent index from 1.0μm to 1.65μm. The results of these test and measurements will be described in the later sections.

Although two-dimensional images of the sun can be obtained using the spectroheliograph with high spectral resolution band-pass, it is relatively slow, especially, for monitoring very fast phenomena on the sun, such as solar flare. The Lyot birefringent filter, proposed by B. Lyot and independently by Y. Öhman in the 1930s, made it possible to take instantaneous two-dimensional monochromatic images of the sun[9-11]. This kind of instrument is known as monochromator. It consists of several polarizers and birefringent crystal (quartz or calcite) plates. Each crystal plate with the optical axis parallel to the face is sandwiched between two polarizers. The thickness of each crystal plate is twice as thick as the preceding one.

Since 1930s, much progress has been made in the design of the birefringent filter. Lyot devised a wide-field configuration in which the element is split into two equal-thickness halves rotated 90° and separated by a half waveplate. This has the effect of making the optical axes symmetric and permits entrance of beams up to 4° - wide field. In addition, each element can be tuned in wavelength by placing a quarter waveplate before the second polarizer. Rotation of the second polarizer can shift the wavelength of the transmission peak. Evans showed that one could eliminate a polarizer by placing one element between the split elements of a thinner one and crossing the end polarizers[12].

It is possible to reduce the total number of polarizers and improve the transmittance significantly.

Another kind of birefringent filter was developed by Iven Šolc in 1949[13-14]. A series of birefringent equal-thickness plates with different optical axes is sandwiched between two polarizers in a Šolc birefringent filter. It has high transmittance, but it is not easy to tune the wavelength. In the 1970s, Jacques M. Beckers employed the achromatic waveplate, made of M_gF_2 and quartz and used from 4200Å to 7000Å, to develop the Universal Birefringent Filter (UBF) which is fully tunable for the entire visible range[15]. In 1976, Alan M. Title proposed a partially polarized birefringent filter with partial polarizers.

In order to obtain two-dimensional solar images or solar magnetograms at different wavelengths simultaneously, the multi-channel birefringent filter was proposed by Guoxiang Ai and Yuefeng Hu[16-18] in 1986. Polarized beam splitters are used as the second polarizers of a few birefringent crystal elements in the birefringent filter to develop multi-channel outputs at different wavelengths. If the wavelengths are on specific Fraunhofer lines, many solar images, even magnetograms, at different wavelengths can be obtained simultaneously. Because the different wavelengths are from different layers of the solar atmosphere, three-dimensional images or magnetic field structures are expected to be obtained. Currently, there are over a hundred birefringent filters, which are working as a key solar instrument around the world. Most of them are used in the visible range of light for chromatic imaging and solar magnetic field observations. The working principle of birefringent filter will be described in detail in the next section.

The Fabry-Perot filter is another type of narrow pass-band device that can be used as a solar imaging instrument. D. Bonaccini et al. employed a Fabry-Perot and a universal birefringent filter to obtain a two-dimensional spectrograph in the visible wavelength range from 4200Å to 7000Å[19-20]. In the 1990s, Craig A. Gullixson et al. proposed using two Fabry-Perot interferometers in tandem to get a near infrared imaging vector magnetograph[21] and measured the properties of the Fabry-Perots with a 1523nm laser and sunlight[22]. In this dissertation, a near-IR (at FeI15648.5Å and FeI15652.9Å) magnetograph, which includes a narrow Fabry-Perot filter and a tunable birefringent filter with liquid crystal variable retarders, is proposed and designed[23].

Magnetic fields are the most important features on the sun because many phenomena that exist on the sun such as sunspots, flares, filaments, etc., are dominated by the solar magnetic field. The solar magnetic field was first measured by George E. Hale at the beginning of this century[24-26]. In 1907-1908, by measuring the Zeeman splitting in magnetically sensitive lines in the spectra of sunspots and detecting the polarization of the split spectral components, Hale provided the first unambiguous and quantitative demonstration that sunspots are the seats of strong magnetic fields. Not only was this the first detection of a magnetic field outside the Earth, but the inferred magnetic field strength, 3000 Gauss, turned out to be over 10 thousand times greater than the Earth's own magnetic field. It was subsequently realized that the pressure provided by such strong magnetic field would also lead naturally to the lower temperatures that were observed within the sunspots, as compared to the photosphere. In the following decade, Hale and collaborators went on to show that large sunspots pairs almost always:

(1) show the same magnetic polarity orientation in each solar hemisphere,

(2) show opposite polarity orientation in the north and south solar hemispheres, and

(3) these polarity orientations are reversed from one sunspot cycle to the next, indicating that the physical magnetic cycle has a period that is twice that of the sunspot cycle.

These empirical observations have stood the test of time and are since known as Hale's polarity Laws. Their physical origin is now known to originate with the operation of a large scale hydromagnetic dynamo within the solar interior, although the details of the process are far from adequately understood. Because the sun's dynamo generated magnetic field is ultimately responsible for all manifestations of solar activity (flares, coronal mass ejections, etc.), to this day, solar dynamo modeling remains a very active area of research in solar physics.

Observations of solar magnetic fields was revolutionized by the development of the magnetograph by Harold Babcock[27]. Until that time, solar magnetic fields could only be detected in sunspots, but in other regions the Zeeman splitting was too small. Babcock developed a photoelectric device to measure the weaker fields[27-28]. In this system, an electro-optic KDP crystal was used in front of the spectrograph. When a proper voltage is applied to this crystal it produces a retardation of a quarter waveplate, which changes circularly polarized light into two light beams linearly polarized at right angles to one another. If a polarizer is placed behind the crystal, one of the light beams can go through. As the voltage is alternated, the intensity of absorption line is modulated. The difference between the intensities is proportional to the longitudinal magnetic field strength. This type of electro-optic device is known as a magnetic analyzer that can be used to select the different polarization. The Babcock system can measure the field at a single point on the

sun. In 1973, Leighton and Smithson[29] replaced the spectrograph with a Lyot birefringent filter and a diode array as the receiver to obtain two-dimensional magnetograms directly. With the tremendous progress in semiconductor technology, the CCD camera became very popular in the visible range. The InGaAs near-IR camera has high photon efficiency and good imaging quality. Hence, the modern magnetographs, which include a tunable birefringent filter or a scanning Fabry-Perot filter as the narrow monochromator and CCD camera as the receiver, are widely used in observations of solar images and magnetic fields.

The spectrograph and the narrow pass-band filter (birefringent filter or Fabry-Perot filter) have advantages and disadvantages as solar observation instruments. With the spectrograph, information can be obtained with

(1) very wide spectral range (from ultraviolet to near infrared),

(2) high spectral resolution (~ 0.01Å), but,

(3) a very small field of view (with a slit) and very low time resolution (it takes a long time to scan a region or the whole disc of the sun!).

With a narrow pass-band filter, the advantages and disadvantages include:

(1) very high time resolution -- instantaneous two dimensional monochromatic images, magnetograms and dopplergrams which measure velocity fields. It is very important for the rapid phenomena, such as solar flares, etc.

(2) designed for specific wavelengths and

(3) relatively lower spectral resolution (~ 0.05Å).

The instrument chosen in the study of solar physics depends on the goals of the research. In this dissertation, the working principles of a Lyot birefringent filter and

tunable wavelength methods will be discussed in section 2.1.2. The measurement principle of solar longitudinal magnetic fields is also discussed in section 2.1.2. The schematic description of the near-IR filter system with a birefringent filter and a Fabry-Perot filter is given in section 2.1.3. The details of the near-IR filter system are discussed in sections 2.2, 2.3 and 2.4.

2.1.2 Principle of a Bireferingent Filter

2.1.2.1 A Simple Lyot Birefringent Filter. A birefringent filter depends on the interference of polarized light transmitted though plates of birefringent crystal in the direction perpendicular to the plane of the optic axes. Let n_e and n_o be the extraordinary and ordinary indices of refraction. The difference between n_e and n_o, $\mu = n_e - n_o$, is known as the birefringent index of the crystal. There are two kinds of birefringent crystals according to the value of μ, positive ($\mu > 0$, e.g., quartz) and negative ($\mu < 0$, e.g., calcite). Consider a plate of some birefringent crystal, such as quartz, calcite, etc., which is cut with its surface parallel to the optical axis of the crystal and perpendicular to the incident light ray. Its optical axis is 45° with the polarization directions of the polarizers, placed between two parallel polarizers (Fig. 2.5). The light ray in the crystal will be split into two rays, one is extraordinary light (e-ray) and the other is ordinary light (o-ray). The fraction of transmitted light τ will be a function of wavelength, λ, and temperature, given by:

$$\tau_{\parallel} = \cos^2(\frac{\delta}{2}) = \cos^2(\frac{\mu(\lambda,T)d}{\lambda}\pi) = \cos^2(\sigma\pi), \tag{2.11}$$

where d is the thickness, μ is the birefringent index of the crystal and λ is the wavelength of light. The quantity, $\delta = 2\pi \frac{(n_e - n_o)d}{\lambda} = 2\pi \frac{\mu d}{\lambda} = 2\pi\sigma$, is known as phase difference between the e-ray and the o-ray, and $\sigma = \mu d/\lambda$ is called the retardation of a birefringent retarder (i.e., the plate of the crystal). $\tau_{\|}$ will be maximized when σ is an integer and minimized when σ is half an integer. The device shown in Fig. 2.5 forms an element of a birefringent filter.

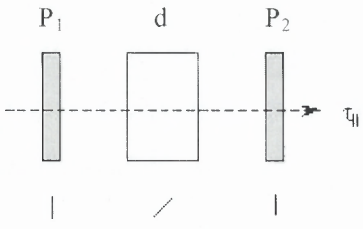

Figure 2.5 An element of a birefringent filter. |: represents polarizer direction along the surface, / : represents the direction of the optical axis along the surface of the calcite plate (45° with polarizer direction).

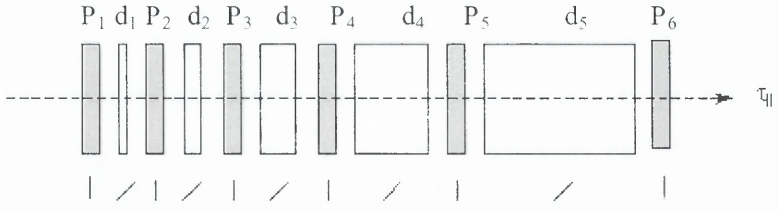

Figure 2.6 A 5-element birefringent filter. |: represents polarizer direction along the surface, / : represents the direction of the optical axis along the surface of the calcite plate (45° to polarizer direction).

When there are a series of polarizers parallel to each other and a birefringent crystal plate placed between each polarizer and the next one, a narrow band birefringent filter

can be constructed by making each crystal plate twice as thick as the following one. A 5-element birefringent filter working in the visible light range of wavelengths is described in Fig. 2.6. Due to $d_2 = 2d_1$, $d_3 = 4d_1$, $d_4 = 8d_1$, $d_5 = 16d_1$, the retardations $\sigma_2 = 2\sigma_1$, $\sigma_3 = 4\sigma_1$, $\sigma_4 = 8\sigma_1$, $\sigma_5 = 16\sigma_1$. The transmittance of the filter is:

$$\tau_{\parallel} = \cos^2(\pi \frac{\mu d_1}{\lambda})\cos^2(\pi \frac{\mu d_2}{\lambda})\cos^2(\pi \frac{\mu d_3}{\lambda})\cos^2(\pi \frac{\mu d_4}{\lambda})\cos^2(\pi \frac{\mu d_5}{\lambda})$$

$$= \cos^2(\pi\sigma_1)\cos^2(2\pi\sigma_1)\cos^2(4\pi\sigma_1)\cos^2(8\pi\sigma_1)\cos^2(16\pi\sigma_1). \qquad (2.12)$$

The output of this birefringent filter could be displayed by modeling the transmittance $\tau_{\parallel}$ with the wavelength of the light (Fig. 2.7).

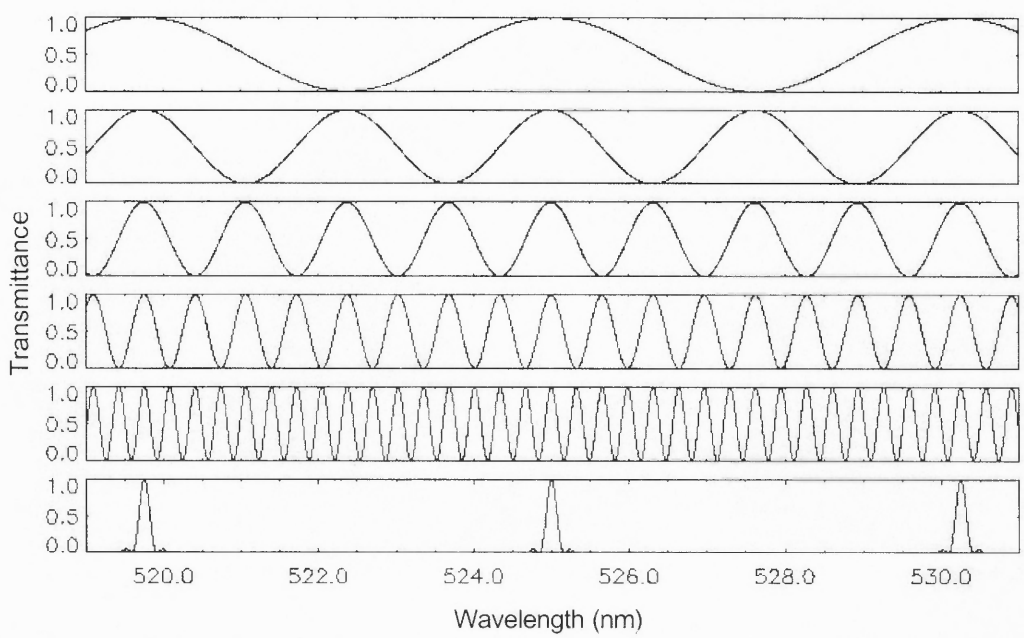

Figure 2.7 Profiles of the transmittance of a 5-element birefringent filter. The 1st (the upper) curve shows the transmittace of the thinnest element and the 5th curve shows the thickest element, the 6th (the low) curve shows the pass-bands of the filter.

A birefringent filter can be designed to transmit a wavelength pass-band of any desired width (down to a fraction of an angstrom) centered at any selected wavelength. An important parameter describing the width of the pass-band is called Full Width of Half

Maximum (FWHM) indicating the spectral width when the intensity of the pass-band is half of the maximum. FWHM is decided by the thickest element. The free spectral range (FSR) of a birefringent filter is another important parameter indicating the spectral separation between two pass-bands (peaks). FSR is decided by the thinnest element.

There are two equivalence principles existing in a birefringent filter[30]:

- Rotational equivalence. If the filter is rotated with the axis along the incident light, the transmittance remains the same.
- Reversible equivalence. If the direction of the incident light is changed by 180°, the transmittance remains the same.

These two principles are very important for determining the directional arrangement of the optical components in the design and assembly of a complicated birefringent filter.

2.1.2.2 Methods of Tuning Wavelength. In practice, it is difficult to control the thickness of a birefringent crystal during polishing for maximizing the transmittance (exactly) on a spectral line. Therefore, a wavelength tunable design of the filter is critical for calibration, testing of components and for the fabrication of an entire filter. On the other hand, wavelength tuning is also required for measurement of solar magnetic fields. There are several methods for tuning wavelength. These are:

- Changing temperature T (μ, d are all functions of T) - Usually it takes a long time to get a stable temperature. Therefore, this method is not usable in practice.
- Rotating polarizers or half waveplate - A quarter waveplate, which follows the crystal with 45° difference of their optical axes, is followed by a rotating polarizer

or a rotating half waveplate. This method has been used widely in many kinds of birefringent filters[30].

The transmittances of a wavelength tunable element in Figs. 2.8 (a) and (b) are:

$$\tau_{\parallel} = \cos^2\left(\frac{\mu(\lambda,T)d}{\lambda}\pi + \alpha\right) = \cos^2(\sigma\pi + \alpha), \tag{2.13}$$

and

$$\tau_{\parallel} = \cos^2\left(\frac{\mu(\lambda,T)d}{\lambda}\pi + 2\beta\right) = \cos^2(\sigma\pi + 2\beta). \tag{2.14}$$

α and β are the angle of rotation of the polarizer and half waveplate respectively. The period of α is π and the period of β is $\pi/2$. Eq. 2.13 and Eq. 2.14 are derived in Appendix A.

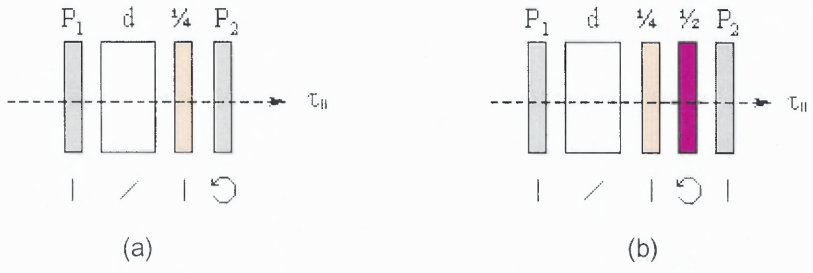

Figure 2.8 Wavelength tunable element with (a) a rotated polarizer or (b) a rotated half waveplate.

- Compensating the crystal with compensators, such as Babinet compensator - is not convenient for mechanical design of birefringent filters.
- Compensating the crystal with liquid crystal retarders - A liquid crystal retarder is a special kind of compensator. It is controlled electrically to change its retardation with different voltages. Recent progresses on the technique of liquid crystal retarders make it possible to use them as compensators to get good performance for imaging.

Figure 2.9 shows a wavelength tunable element with a liquid crystal retarder. The transmittance, $\tau_{//}$, is given by:

$$\tau_{\parallel} = \cos^2\left[\left(\frac{\mu(\lambda,T)d}{\lambda} + \Delta\right)\pi\right] = \cos^2[(\sigma + \Delta)\pi]. \tag{2.15}$$

Δ is the retardation given by the liquid crystal retarder. It changes from 0 to 1.

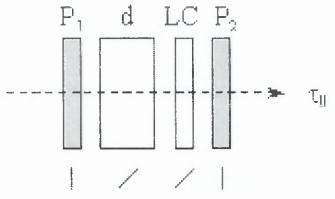

Figure 2.9 Wavelength tunable element with liquid crystal retarder.

2.1.2.3 Measurement Principle of Solar Magnetic Field. Typically, when a magnetic field exists, a spectral line is split into two shifted components, σ, and one unshifted component, π. If the line of sight is along the direction of the magnetic field, ***B***, the observer can only see the σ components, which are right and left handed circularly polarized light. This is the longitudinal Zeeman effect (Fig. 2.10).

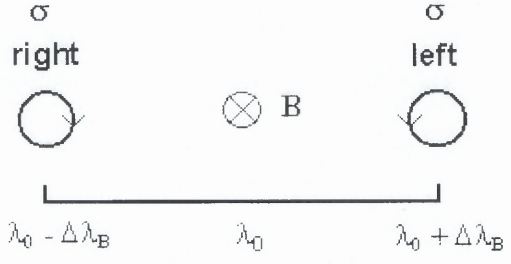

Figure 2.10 The longitudinal Zeeman effect.

If the line of sight is perpendicular to the direction of the magnetic field, ***B***, the observer can see the three components: two σ components, which are parallel to ***B***, and the π component, which is perpendicular to ***B***. This is the transverse Zeeman effect (Fig. 2.11).

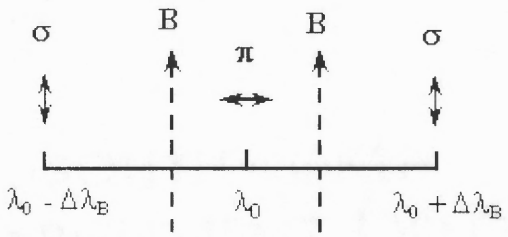

Figure 2.11 The transverse Zeeman effect.

The shift of the wavelength is given by:

$$\Delta\lambda_B = \frac{e}{4\pi c m_e} g\lambda^2 B\,, \tag{2.16}$$

where, g is the Lande factor, B is the magnetic field strength, λ is the wavelength of radiation, e is the value of electron charge and m_e is electron mass. If B is in gauss and λ is in angstroms, $\Delta\lambda_B$ is equal to:

$$\Delta\lambda_B = 4.7\times10^{-13} g\lambda^2 B\,. \tag{2.17}$$

A very narrow pass-band filter is not only a monochromator for getting solar monochromatic images, but also a key instrument for measuring solar magnetic fields. The measurement principle of solar magnetic field is here described briefly. Consider a simple case, in which the magnetic field is parallel to the line of sight (longitudinal magnetic field). A light beam is split into opposite circularly polarized beams by a longitudinal magnetic field. Left and right handed circularly polarized light will be

become mutually orthogonal linear polarized light when passing through a quarter waveplate,

(1) passing through a $+\frac{\lambda}{4}$ (+45°) and the liquid crystal (0° retarder)(Fig. 2.12);

right circularly polarized light becomes ↕ (90° linear),

left circularly polarized light becomes ↔ (0° linear);

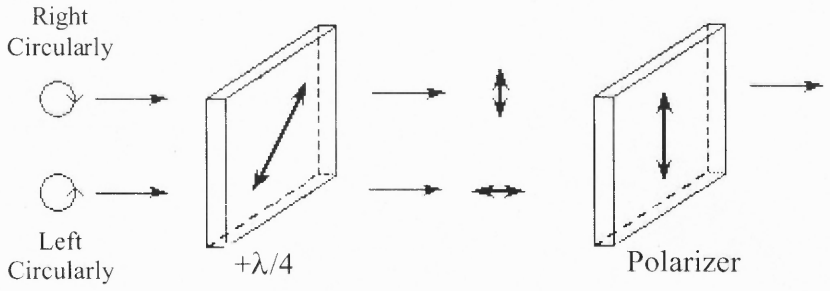

Figure 2.12 The states of the circularly polarized light when through +λ/4.

(2) passing through a $-\frac{\lambda}{4}$ (−45°) and the liquid crystal(180° retarder)(Fig. 2.13);

right circularly polarized light becomes ↔ (0° linear),

left circularly polarized light becomes ↕ (90° linear).

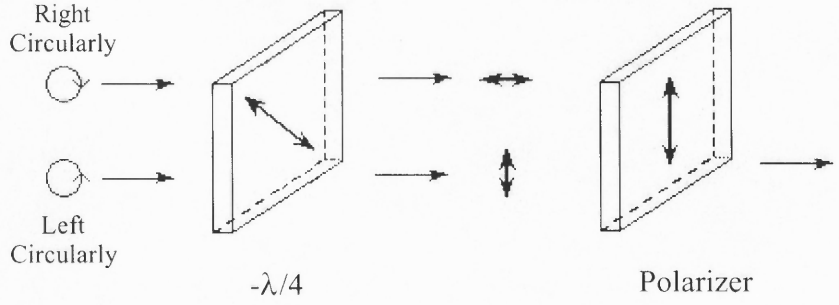

Figure 2.13 The states of the circularly polarized light when through -λ/4.

When measuring longitudinal magnetic fields, a magnetic analyzer (including a quarter waveplate and a liquid crystal variable retarder) is used to allow only the left circularly polarized light or right circularly polarized light to enter the narrow pass-band filter, blocking the orthogonal polarization[31-32].

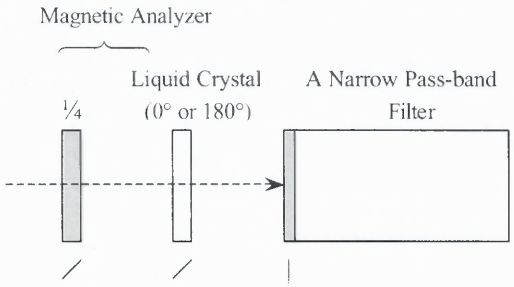

Figure 2.14 Setup of the Instruments for Measurement of Longitudinal Magnetic Fields.

Figure 2.14 shows the setup of the instruments when the longitudinal magnetic fields are measured. Because the first polarizer of the birefringent filter is 90°, when the liquid crystal has a 0° retarder, only right circularly polarized light can go through the filter and the intensity on the CCD camera is I_R. When the liquid crystal has a 180° retarder, only left circularly polarized light can go through the filter and the intensity on the CCD camera is I_L.

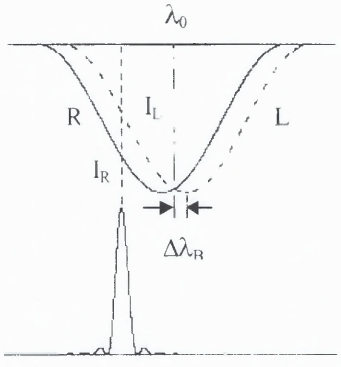

Figure 2.15 Principle of magnetic field measurement.

Figure 2.15 is a schematic of the profiles of the spectral lines and the filter. Then the intensity difference is:

$$\Delta I_B = I_R - I_L \tag{2.18}$$

If $\Delta\lambda_B = 0$, $I_R = I_L$, then $\Delta I = 0$. If $\Delta\lambda_B \neq 0$, but small, then $\Delta I_B \propto \Delta\lambda_B \propto B$, and the longitudinal magnetic field intensity $B(x,y)$ can be obtained[32].

2.1.3 The Research Objective

The goal of this research work is to develop a near infrared filter system for measurement of solar magnetic fields at 1.56μm at Big Bear Solar Observatory (BBSO), New Jersey Institute of Technology (NJIT). Such a system, including a prefilter, a magnetic analyzer, a narrow-band filter and an IR camera (Fig.2.16), forms a magnetograph system.

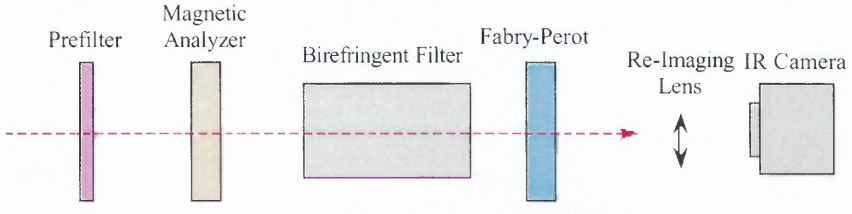

Figure 2.16 A schematic of the near-IR magnetograph.

The details of the sections are as follows:

- Prefilter: interference filter
- Magnetic analyzer: a near infrared ¼ waveplate and a liquid crystal variable retarder (retardance is 0° or 180°) as a modulator
- A narrow pass-band filter: **a near-IR tunable birefringent filter** (FWHM ≤ 2.5Å) and a Fabry-Perot (Queensgate Instruments, FWHM ~ 0.12Å)

- Near-IR InGaAs camera: Sensors Unlimited, 10000Å to 17000Å, 320×240 pixels

This system is expected to achieve a clean narrow pass band of 1/8Å. Using this system, we can obtain the chromatic images in a spectral range near 1.56μm and solar magnetograms. The pass-band of this system can also be tuned across the spectral line to obtain line profiles of every point in a two-dimensional field of view.

2.2 Measurement of the Birefringent Index of Calcite

2.2.1 Birefringent Index of Calcite at 1.56μm

In section 2.1.2, it was mentioned that the birefringent index of a crystal, $\mu = n_e - n_o$, is an important parameter for the design and fabrication of a birefringent filter.

In the visible light range (0.4μm to 0.7μm), the values of the birefringent index of calcite and quartz are quite reliable. Refractive index values and the birefringent index values of calcite in handbooks of optics[33, 34] are presented in Table 2.1. But, in the infrared range, we could extrapolate the value of μ at 1.56μm up to about -0.156 from of the curve in Fig. 2.17.

During the design of the near-IR magnetograph, this value was used in the calculations of thickness of calcite elements. But, in the process of testing the polished calcite, the FWHM of every element does not coincide with the design value.This is because, the "known" value of the birefringent index of calcite at 1.56 μm is found to be unreliable in the near infrared range. Therefore, the birefringent index of calcite and its temperature coefficient at 1.56μm are measured. Furthermore, the birefringent indices of

calcite from 1.0μm to 1.65μm has also been measured because this near-IR range is very important not only in solar physics, but also in fiber optics and communications (1300nm to 1600nm is a good window for fiber transmissions).

Table 2.1 The Refractive Indices and Birefringent Indices of Calcite in Handbook of Optics[33]

λ (μm)	n_o	n_e	$\mu = n_e - n_o$	λ (μm)	n_o	n_e	$\mu = n_e - n_o$
0.394	1.68374	1.49810	-0.18564	0.991	1.6438	1.48022	-0.16358
0.410	1.68014	1.49640	-0.18374	1.042	1.64276	1.47985	-0.16291
0.434	1.67552	1.49430	-0.18122	1.097	1.64167	1.47948	-0.16219
0.441	1.67423	1.49373	-0.18050	1.159	1.64051	1.4791	-0.16141
0.508	1.66527	1.48956	-0.17571	1.22	1.63926	1.4787	-0.16056
0.533	1.66277	1.48956	-0.17321	1.273	1.63849	--	--
0.560	1.66046	1.48736	-0.17310	1.307	1.63789	1.47831	-0.15958
0.589	1.65835	1.4864	-0.17195	1.32	1.63767	--	--
0.643	1.65504	1.4849	-0.17014	1.369	1.63681	--	--
0.656	1.65437	1.48459	-0.16978	1.396	1.63637	1.4778	-0.15857
0.670	1.65367	1.48426	-0.16941	1.422	1.6359	--	--
0.706	1.65207	1.48353	-0.16854	1.479	1.6349	--	--
0.768	1.61974	1.48259	-0.13715	1.497	1.63457	1.47744	-0.15713
0.795	1.6488	1.48216	-0.16664	1.541	1.63381	--	--
0.801	1.64869	1.48216	-0.16653	1.609	1.63261	--	--
0.833	1.64772	1.48176	-0.16596	1.615	--	1.47695	--
0.867	1.64676	1.48137	-0.16539	1.682	1.63127	--	--
0.905	1.64578	1.48098	-0.16480	1.749	--	1.47683	--
0.946	1.6448	1.4806	-0.16420	1.761	1.62974	--	--

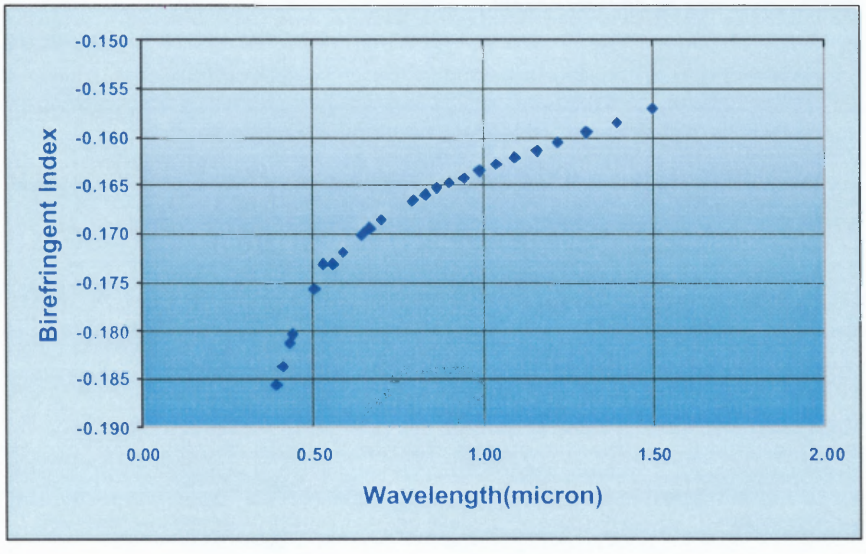

Figure 2.17 A chart of the published values birefringent index of calcite from 0.4μm to 1.7μm.

2.2.1.1 Principle of Measurement and Setup of the Instruments. As discussed in section 2.1.2.1 and shown in Fig. 2.5, the interference output of an element of a birefringent filter is a cosine square function with wavelength, λ. This is the case if the measured calcite is introduced between two parallel polarizers with its optical axis at 45° with respect to the polarization direction of the polarizers. Eq. 2.11 gives:

$$\tau_{\parallel} = \cos^2\left(\frac{\mu(\lambda,T)d}{\lambda}\pi\right) = \cos^2(\sigma\pi)\,. \tag{2.19}$$

When the retardation $\sigma = \mu d/\lambda$ is an integer, the transmission τ will be maximized, whereas, it will be minimized if σ is a half integer.

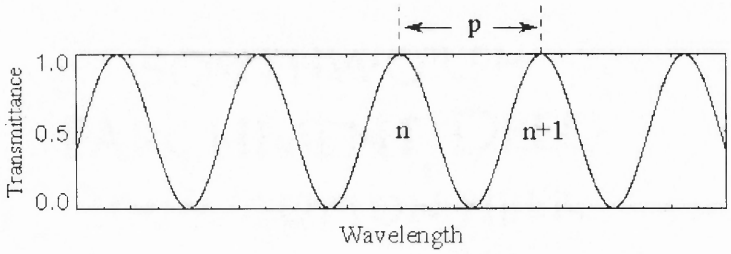

Figure 2.18 A scheme of output profile of transmittance with wavelength.

Let n be the retardance (negative integer, due to the negative value of μ) at λ and let p be the wavelength separation from an adjacent maximum peak at the same temperature T (see Fig. 2.18). We have:

$$n = \frac{\mu d}{\lambda}, \tag{2.20}$$

$$n+1 = \frac{\mu d}{\lambda + p} \approx \frac{\mu d}{\lambda}\left(1 - \frac{p}{\lambda}\right). \tag{2.21}$$

Assume that p is much smaller than λ and μ is unchanged within adjacent p near λ. From Eq. 2.20 and Eq. 2.21, we can get:

$$n = -\frac{\lambda}{p}, \tag{2.22}$$

$$\mu = \frac{n\lambda}{d} = -\frac{\lambda^2}{pd}. \tag{2.23}$$

Therefore, if p and d can be measured, we can calculate μ at wavelength λ and temperature T using Eq. 2.23. The measurement error can be estimated by:

$$\Delta\mu \approx \mu\left(\frac{\Delta p}{p} + \frac{\Delta d}{d}\right). \tag{2.24}$$

This is a random error in the measurement of μ. The systematic errors due to instrument errors, such as polarization direction of the polarizers and the optical axis of the calcite, only increase scattered light, but do not affect wavelength positions of the peaks (maximum values). Therefore, these kinds of errors do not give rise to measurement error of μ. Error analyses and calculations are given in appendix B.

Because the birefringent index, μ, is temperature sensitive, the calcite plate must be contained in a temperature-controlled chamber. The two parallel polarizers and an insulated container are installed on a regular bench (Fig. 2.19), and the bench is placed in front of the slit of the spectrograph of BBSO when measuring the birefringent index of calcite or testing the optical components.

The two polarizers, P_1 and P_2, are separately mounted on accurate rotators, and are set to be parallel to each other and to one of the inner sides of the insulated container. The measured calcite is square and the optical axis of the calcite plate is along the surface and 45.0° ± 2′ to its one side. The calcite could be put in or taken out from the container easily for tests.

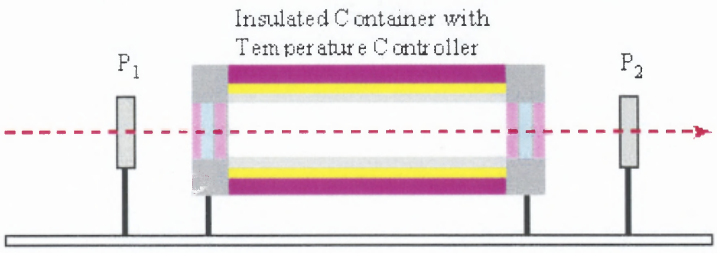

Figure 2.19 Schematic of the insulated container and the polarizers.

The container was designed by Jun Ma, a Master's student of the Mechanical Engineering Department at NJIT, and fabricated in the workshop at NJIT[35]. This container consists of an aluminum tube as a good heat conductor for holding the measured calcite, two PVC end-plates with two optical widows, heater outside the aluminum tube for heating and insulated material outmost for heat isolation. Figure 2.20 is a mechanical scheme of the insulated container mounted on a bench.

There are five holes in the tube for holding five temperature sensors. The precision of the temperature read by the sensors can be to ±0.1°C. The electrical control system was designed by Thomas J. Spirock[36], a Ph. D. candidate of the Electrical Engineering Department and Big Bear Solar Observatory, NJIT.

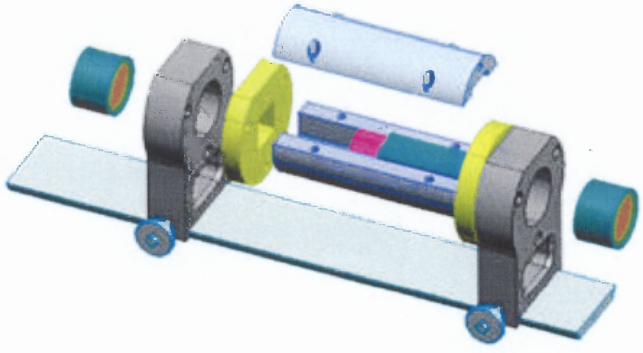

Figure 2.20 The structure of the insulated container (Courtesy of Jun Ma).

The setup of the all instruments for tests with the spectrograph at BBSO is shown in Fig. 2.21. The sunlight from the 26-inch telescope enters the thermally insulated container and is focused on the slit before being incident on the grating. From the grating, it proceeds to the IR camera and subsequently to the on-line computer for image acquisition and analysis.

When a measured calcite plate is not inside the container, the spectral image can be obtained for calibrating spectral resolution and determining positions of spectral lines. When the measured calcite plate is put inside the container, after the temperature of the container becomes stable, the transmission images (interference patterns) at different temperatures can be obtained.

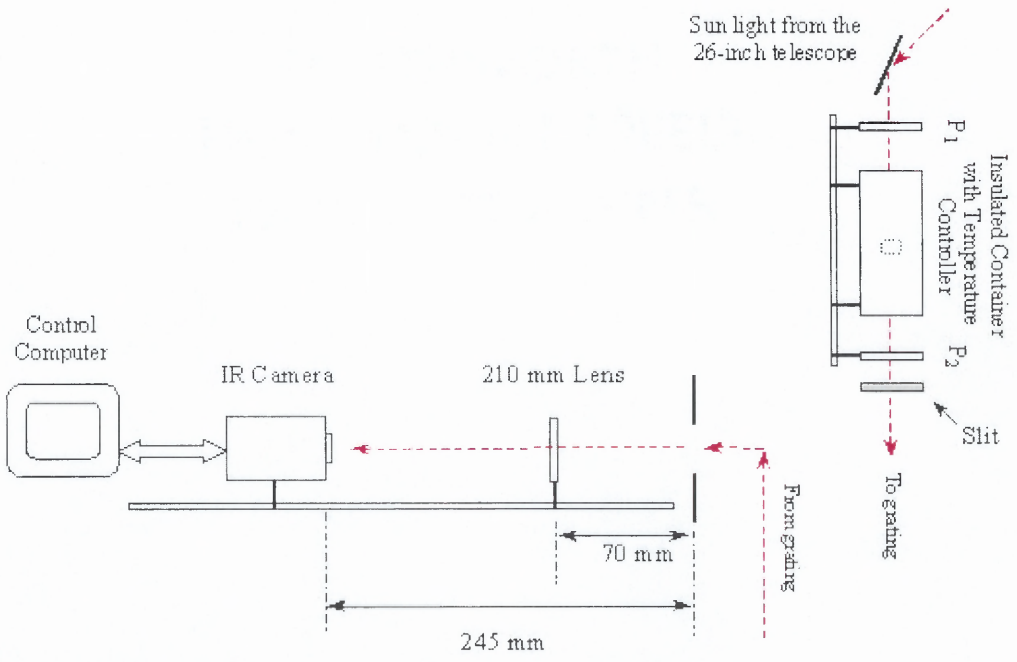

Figure 2.21 Setup of instrument for measuring the calcite birefringent index and testing optical components.

Figure 2.22 shows the measured results of the processed transmission images at different temperatures. The vertical axes are the slit images with the wavelength, λ, as the horizontal axes. Figure 2.22j is the spectral image with which we can calibrate the spectral resolution for data analysis. Figs. 2.22a – i represent the transmission images at 11.0°C, 15.0°C, 19.0°C, 21.0°C, 23.0°C, 28.0°C, 33.0°C, 37.0°C and 43.0°C respectively. Figure 2.22 very clearly shows that the maximum peaks (marked n) shift to shorter wavelength with increasing temperature due to variations in the birefringent index and thickness of the calcite. This is an important and useful experimental result during the design and test of a birefringent filter system.

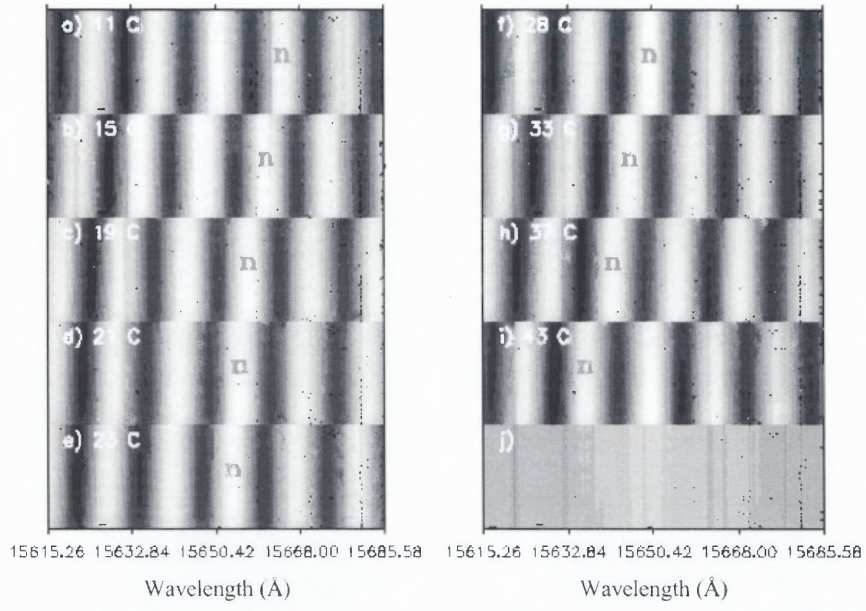

Figure 2.22 Transmission images at different temperatures. a) T = 11°C, b) T = 15°C, c) T = 19°C, d) T = 21°C, e) T = 23°C, f) T = 28°C, g) T = 33°C, h) T = 37°C, i) T = 43°C, j) spectral image near 15648.5 Å.

2.2.1.2 Birefringent index of Calcite at Room Temperature (21°C) and at the Filter Working Temperature (43°C). The measured calcite plate is a sample plate with thickness, d_0 = 10498.0 ± 3.0μm at T_0 = 69.0°F (21.56°C). The thermal expansion coefficient along the direction perpendicular to the optical axis of calcite is $\beta = -3.7\times10^{-6}$ /°C[33]. Because β is negative, calcite will shrink in this direction with increase of temperature like ice. We can obtain its thickness at temperature, T, by $d = d_0 (1+\beta\Delta T)$, where, $\Delta T = T - T_0$. From Fig. 2.22j, we can obtain the spectral profile vs. pixel position or wavelength λ (Fig. 2.23). Figure 2.23 shows a sample spectral profile near FeI15648.5Å. The locations of the two lines L1, L2, whose wavelengths are λ(L1) =15621.695Å, λ(L2) =15662.012Å, can be identified in pixels. A spectral resolution of 0.2940Å/pixel is obtained from these data. This resolution results from dividing the spectral range by the number of pixels in the X-axis of the image. Thus, wavelength corresponding to each pixel can be calculated and the X-axis can be translated into wavelength. Although the background of the images is not uniform, it does not affect the analysis of the data.

Figure 2.23 shows the normalized transmission profiles of the measured calcite plate with respect to wavelength at room temperature T = 21°C and the filter operating temperature T = 43°C. The separation between the two maximum peaks, p, is measured as p (21°C) = 13.156Å and p (43°C) = 13.176Å. Using Eq. 2.22, we get $n(\lambda$=15648.5 Å, T = 21°C) = -15648.5Å/13.156Å = -1189.4356 and n (λ=15648.5 Å, T = 43°C) = -15648.5 Å/13.176Å = -1187.6662. The thickness of the calcite is d(21°C) = $d_0(1+\beta\Delta T)$ =10498.03μm and d(43°C) = $d_0(1+\beta\Delta T)$ = 10497.18μm, using Eq. 2.23 we obtain:

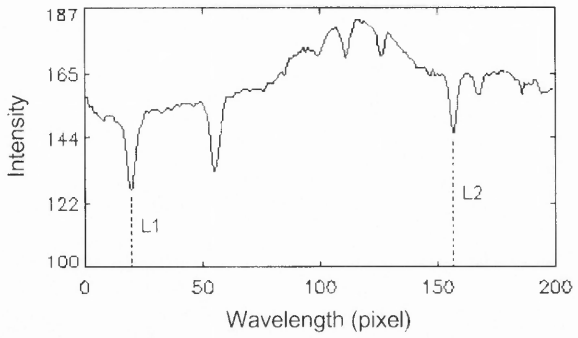

Figure 2.23 Spectral profile near FeI 15648.5Å. L_1, L_2 represent the two lines for calibrating the spectral resolution.

$$\mu\,(\lambda = 15648.5\ \text{Å}, T = 21°\text{C}) = n\lambda/d\,(21°\text{C}) \approx -0.1772989, \tag{2.25}$$

$$\mu\,(\lambda = 15648.5\ \text{Å}, T = 43°\text{C}) = n\lambda/d\,(43°\text{C}) \approx -0.1770494. \tag{2.26}$$

The accuracy in the measurement of p is about $\Delta p \approx \pm 0.03$Å (0.2940 Å has been approximated to 0.3Å and the error during data analysis is down to $\pm\frac{1}{10}$ pixel $\Rightarrow$ ± 0.3Å$/10 = \pm 0.03$Å) and $\Delta d \approx \pm 3.0\mu$m. Therefore, the error in the measurement of μ is:

$$\Delta\mu \approx \mu(\Delta p/p + \Delta d/d) \approx \pm 4.5 \times 10^{-4}. \tag{2.27}$$

Thus,

$$\mu\,(\lambda = 15648.5\ \text{Å}, T = 21°\text{C}) \approx -0.17730 \pm 4.5 \times 10^{-4}, \tag{2.28}$$

$$\mu\,(\lambda = 15648.5\ \text{Å}, T = 43°\text{C}) \approx -0.17705 \pm 4.5 \times 10^{-4}. \tag{2.29}$$

2.2.1.3 Temperature Coefficients of the Birefringent Index. Although we determined the birefringent index of calcite at T = 21°C and T = 43°C, we cannot calculate the thermal coefficient of μ just using these two indices because if will include big measurement error. In this section, the thermal coefficients of calcite are measured

independent of the birefringent index μ and thickness of the sample. Figure 2.22 clearly shows the shifts to the blue (short wavelength) end of the spectrum for the maximum peaks with an increase in temperature. These shifts are due to the variation of μ and shrinking of the calcite thickness as temperature increases. If α is the thermal coefficient of μ and β is the thermal expansion coefficient, we have:

$$\mu(T_2) \approx \mu(T_1)\,(1 + \alpha\,\Delta T), \tag{2.30}$$

and

$$d(T_2) \approx d(T_1)\,(1 + \beta\,\Delta T), \tag{2.31}$$

where, $\Delta T = T_2 - T_1$, $\beta = -3.7\times10^{-6}$/ °C. The higher orders of ΔT are ignored.

For a specific peak of the intensity, let the retardation be n at a specific temperature T_1 and let the position be λ_1 as shown in Fig. 2.22. The position of the peak will shift from λ_1 to λ_2 as the temperature increases, where $\Delta\lambda = \lambda_2 - \lambda_1$. Therefore, we have:

$$\text{at } T_1, \quad n = \frac{\mu_1 d_1}{\lambda_1}, \tag{2.32}$$

$$\text{at } T_2, \quad n = \frac{\mu_2 d_2}{\lambda_2} \approx \frac{\mu_1(1+\alpha\Delta T)d_1(1+\beta\Delta T)}{\lambda_1+\Delta\lambda} \approx \frac{\mu_1 d_1}{\lambda_1}\left(1+\alpha\Delta T+\beta\Delta T-\frac{\Delta\lambda}{\lambda_1}\right). \tag{2.33}$$

The higher order terms are neglected in Eq. 2.33. Combining Eqs. 2.32 and 2.33, we obtain:

$$\alpha+\beta=\frac{\Delta\lambda}{\lambda_1\Delta T}. \tag{2.34}$$

Knowing the wavelengths at which the peaks occur (marked as n in Fig. 2.22) and with the use of Eq. 2.34, we get the results for α as shown in Table 2.2. α is obtained by subtracting β from values of $\alpha + \beta$. The temperature coefficient the birefringent index, α,

and the thermal expansion coefficient of calcite, β, are properties of calcite that are independent of the thickness of the crystal and its birefringent index.

The values in Table 2.2 show some variation of α with respect to temperature. The average value of α is about -5.37×10^{-5}. We use this value to get the birefringint index of calcite at 43°C:

$$\mu(43°C) \approx \mu(21°C)\,(1.0 + (43.0°C - 21.2°C)\times(-5.37 \times 10^{-5}/°C)) \approx -0.17709. \qquad (2.35)$$

This value of μ at 43°C matches quite well with the value obtained in Eq. 2.29. It is to be noted here that the values of α in Table 2.2 are in accordance with the data reported in the literature[33, 34].

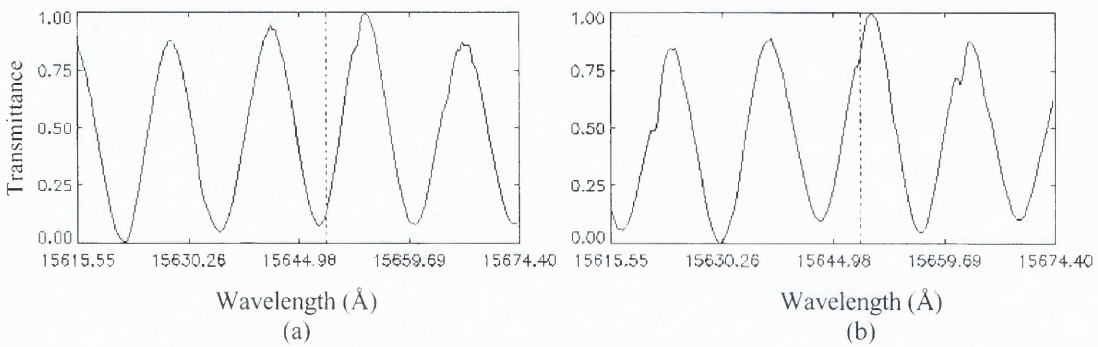

Figure 2.24 The normalized transmission profiles of the sample calcite at T = 21°C (a) and T = 43°C (b). The dashed lines indicate the FeI 15648.5Å line.

Table 2.2 Measurement Results for Thermal Coefficient of Birefringent Index

Temperature (°C)	Wavelength at peak n (Å)	$\alpha + \beta$ (10^{-5}/°C)	α (10^{-5}/°C)
11.3	15664.768	-5.69	-5.32
15.2	15661.293	-5.81	-5.51
19.2	15657.494	-5.85	-5.48
21.2	15655.727	-5.97	-5.60
23.0	15653.952	-5.78	-5.41
28.0	15649.833	-5.23	-4.86
33.0	15645.772	-5.49	-5.12
37.0	15642.153	-5.93	-5.56
43.0	15636.444	-6.08	-5.71
		Average:	-5.37

2.2.2 Birefringent Indices of Calcite from 1.00μm to 1.65μm at 21°C

In section 2.2.1, we discussed the birefringent index of calcite near 1.5648μm. This is required for our IR birefringent filter. In this section, a discussion of the measurements of birefringent indices of calcite in a wide wavelength range is presented. Sunlight is the light source and the same sample of calcite is used. As described in section 2.2.1, the measurement includes several steps:

(1) Choosing the working wavelength range - This depends on (a) the intensity of the solar spectrum. In some spectral range, many strong absorption lines occur with the result that the intensity of solar spectra appear to be too low (or dark) to be measured. (b) If there are stable lines due to specific chemical species (for example, iron, helium, etc.), they can be identified from the calibration of the spectral resolution (Å/pixel), we call these spectral lines as "calibration lines".

(2) Obtaining the spectral image and the calcite interference image at same spectral resolution.

(3) Getting the spectral resolution and the wavelength separation between two adjacent peaks or troughs, p.

(4) Eq. 2.23 gives the birefringent index, μ, at this wavelength range.

(5) Error analysis.

The solar spectrum has been investigated from 1.00μm to 1.65μm and 10 wavelength ranges are chosen. Exact wavelengths of the calibration lines are figured out using data of Solar Atlas[37]. Figs. 2.25a-j present the spectral images, calcite interference images and the profiles of the images in 10 different wavelength ranges.

The temperature is set to 21.0 °C. The thickness of the sample calcite is 10498.0 ± 3.0μm. In the following section, we describe the calculations of birefringent indices of calcite in these ten spectral ranges.

CASE 1 (Fig. 2.9a):

Central wavelength: 10050.0Å

Temperature: 21.0 ± 0.1 °C

Wavelength range: λ = 10050.0 ± 30.0Å

Calibration lines: $\lambda(L_1)$ =10036.664Å, $\lambda(L_2)$ =10065.065Å

Spectral resolution: r = 0.32274Å/pixel

Wavelength separation: p = 17.09 pixel, i.e., p = 5.5156Å

$$\mu \approx -\frac{\lambda^2}{pd} \approx -0.174435 \pm 1.0\times10^{-3} \tag{2.36}$$

CASE 2 (Fig. 2.9b):

Central wavelength: 10140.0Å

Temperature: 21.0 ± 0.1 °C

Wavelength range: λ = 10140.0 ± 30.0Å

Calibration lines: $\lambda(L_1)$ =10123.890Å, $\lambda(L_2)$ =10145.584Å

Spectral resolution: r = 0.33856Å/pixel

Wavelength separation: p = 17.40pixel, i.e., p = 5.5438Å

$$\mu \approx -\frac{\lambda^2}{pd} \approx -0.176671 \pm 1.0\times10^{-3} \tag{2.37}$$

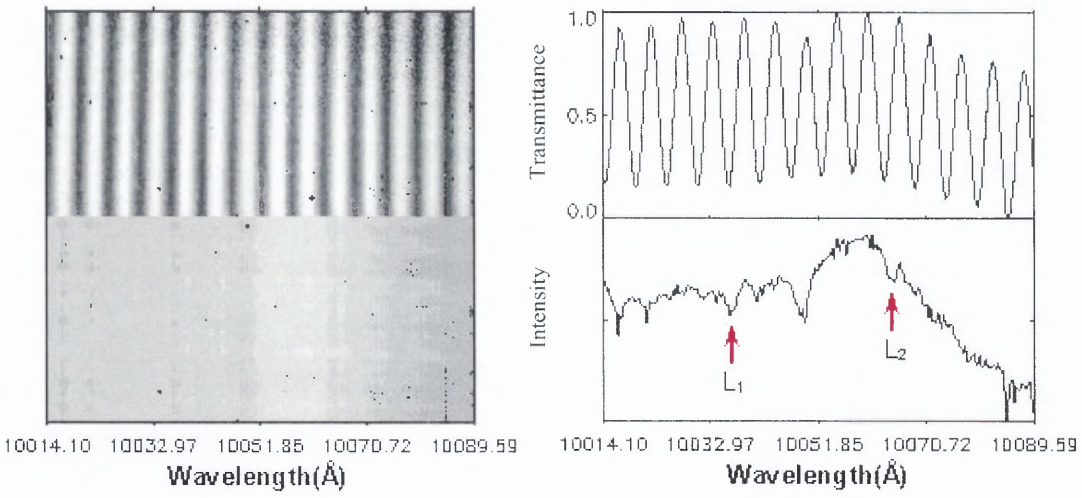

Figure 2.25a Data analysis at 10050 ± 30Å. Interference image of calcite (left up), normalized transmittance profile (right up), spectral Image (left down) near 10050Å, spectral profile and the marked calibration lines (right down).

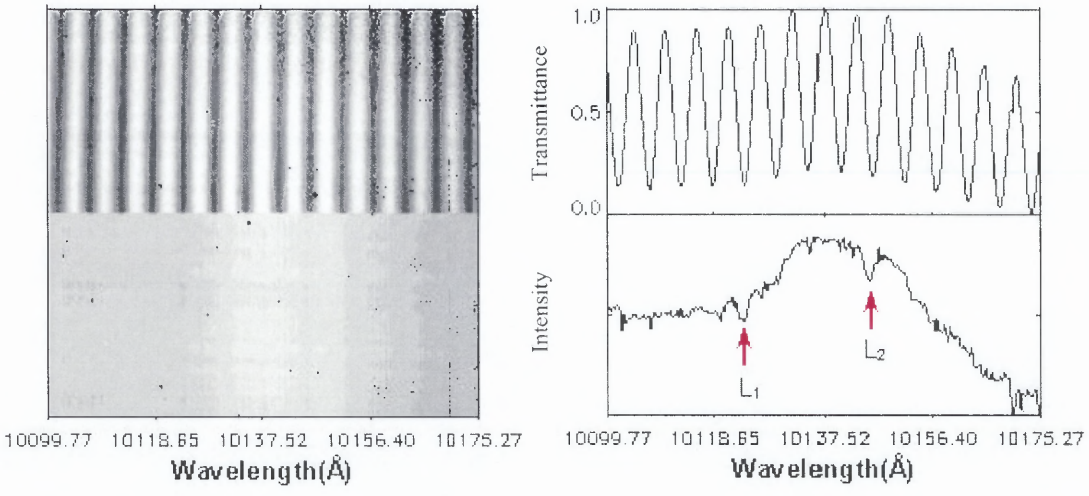

Figure 2.25b Data analysis at 10140 ± 30Å. Interference image of calcite (left up), normalized transmittance profile (right up), spectral Image (left down) near 10140Å, spectral profile and the marked calibration lines (right down).

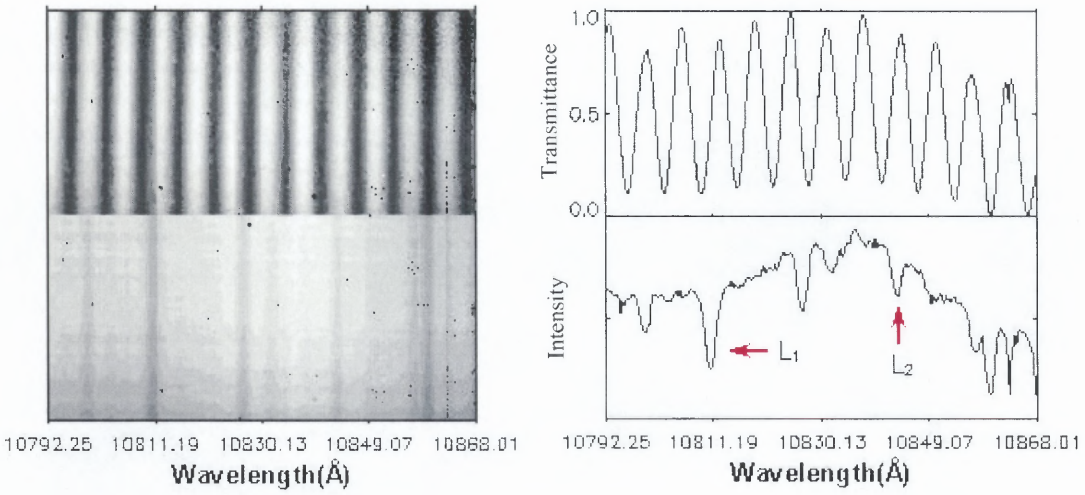

Figure 2.25c Data analysis at 10830 ± 30Å. Interference image of calcite (left up), normalized transmittance profile (right up), spectral Image (left down) near 10830Å, spectral profile and the marked calibration lines (right down).

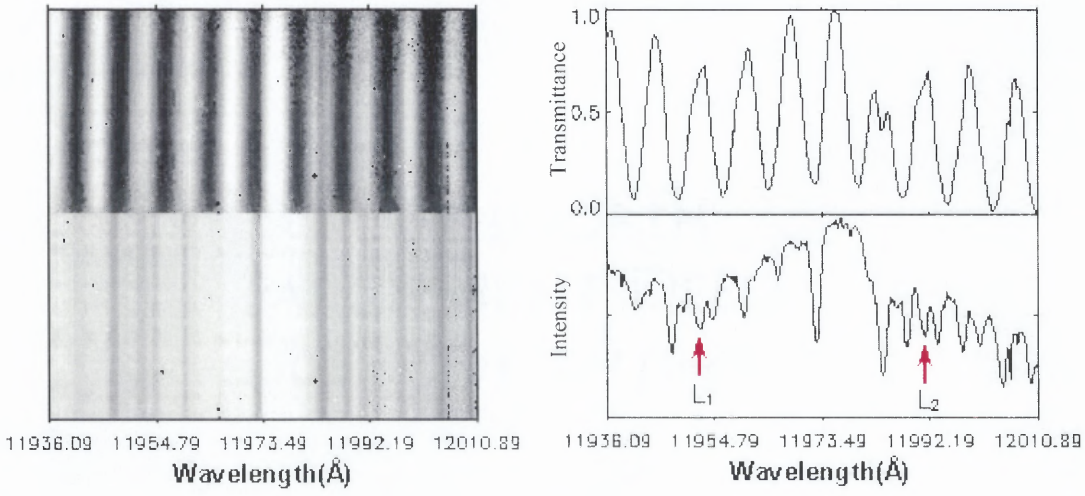

Figure 2.25d Data analysis at 11970 ± 30Å. Interference image of calcite (left up), normalized transmittance profile (right up), spectral Image (left down) near 11970Å, spectral profile and the marked calibration lines (right down).

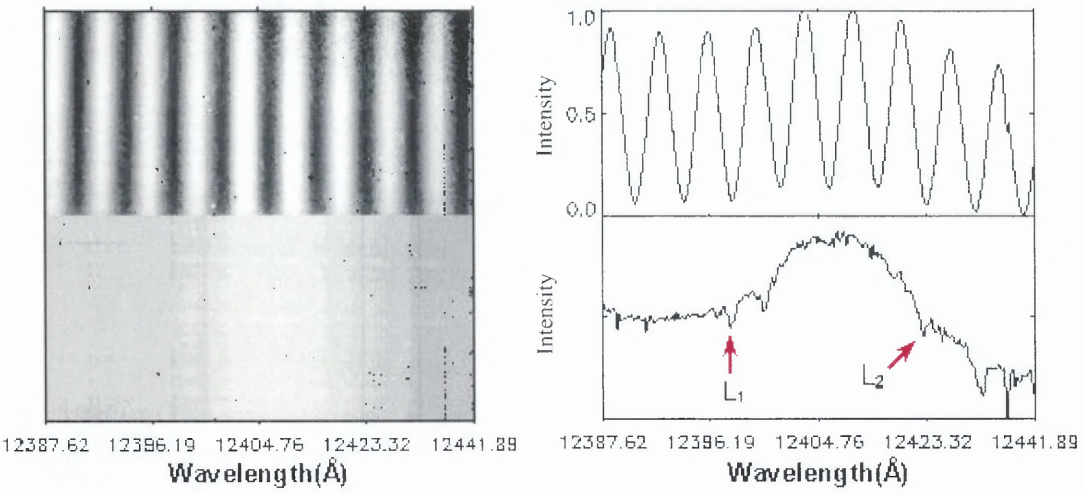

Figure 2.25e Data analysis at 12400 ± 30Å. Interference image of calcite (left-up), normalized transmittance profile (right up), spectral Image (left-down) near 12400Å, spectral profile and the marked calibration lines (right-down).

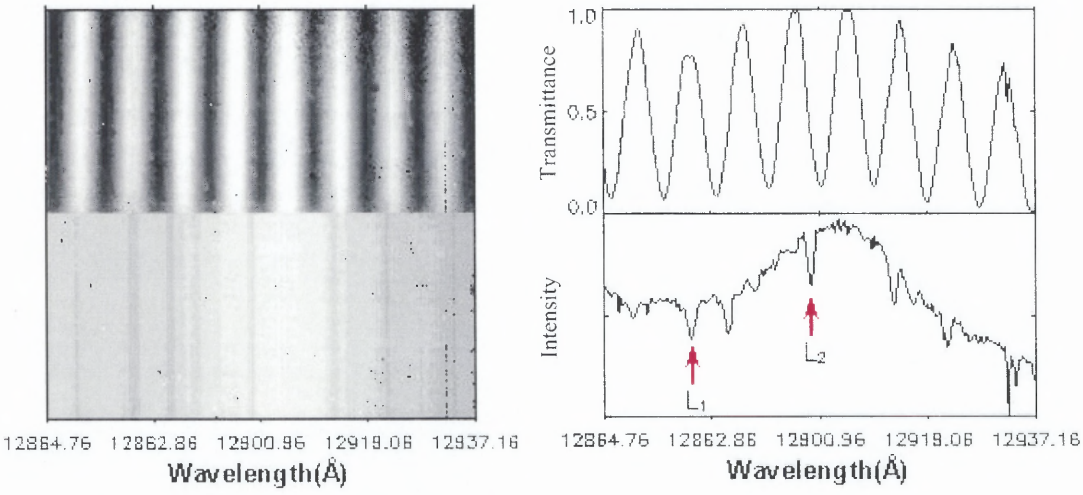

Figure 2.25f Data analysis at 12900 ± 30Å. Interference image of calcite (left up), normalized transmittance profile (right up), spectral Image (left down) near 12900Å, spectral profile and the marked calibration lines (right down).

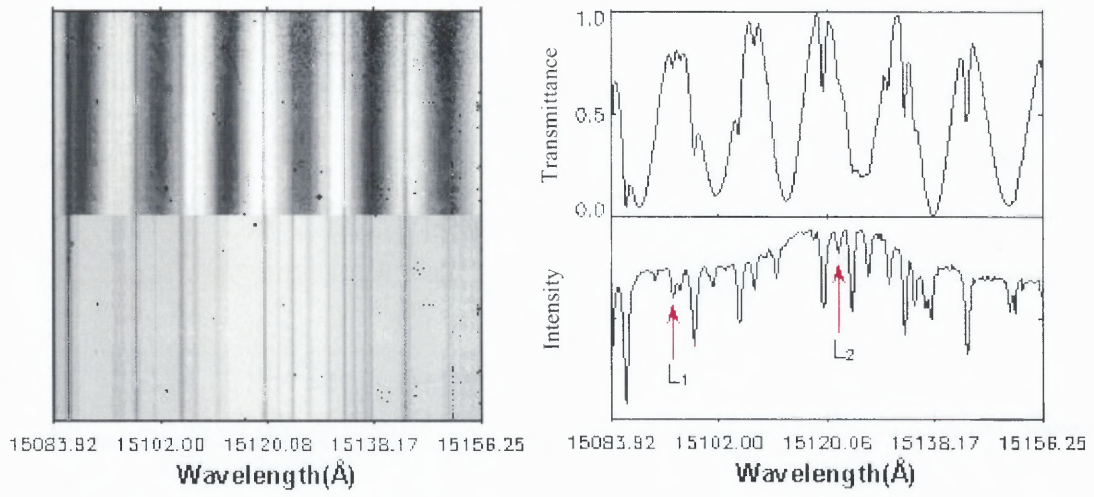

Figure 2.25g Data analysis at 15110 ± 30Å. Interference image of calcite (left up), normalized transmittance profile (right up), spectral Image (left down) near 15110Å, spectral profile and the marked calibration lines (right down).

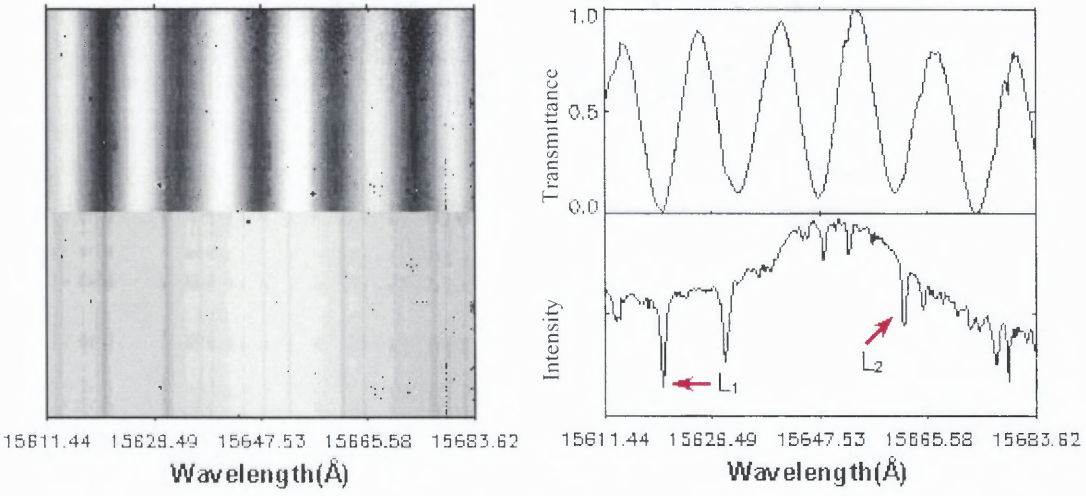

Figure 2.25h Data analysis at 15650 ± 30Å. Interference image of calcite (left up), normalized transmittance profile (right up), spectral Image (left down) near 15650Å, spectral profile and the marked calibration lines (right down).

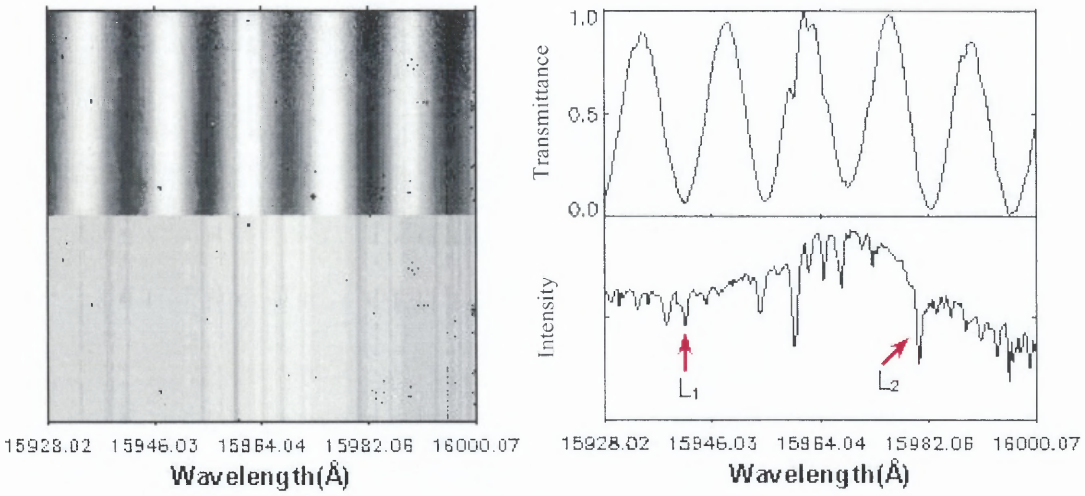

Figure 2.25i Data analysis at 15960 ± 30Å. Interference image of calcite (left up), normalized transmittance profile (right up), spectral Image (left down) near 15960Å, spectral profile and the marked calibration lines (right down).

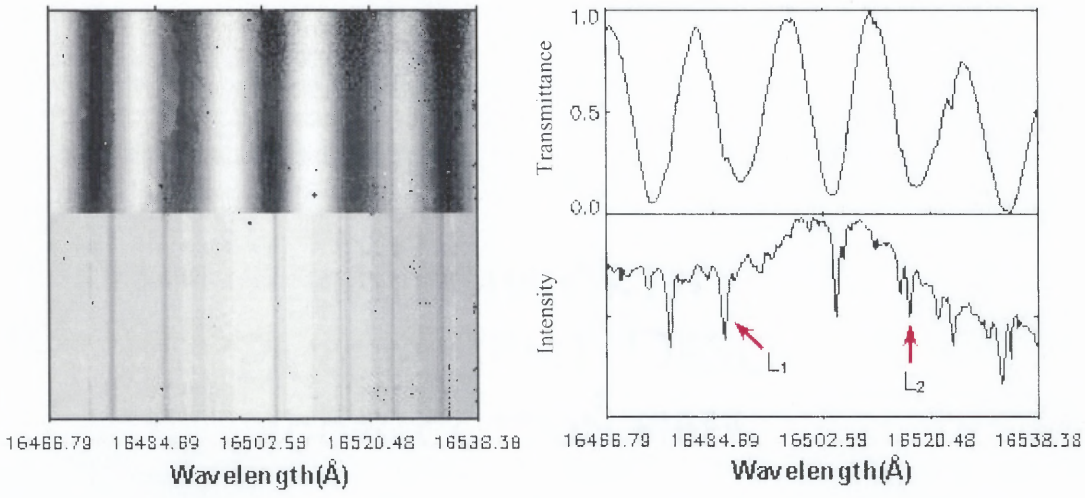

Figure 2.25j Data analysis at 16500 ± 30Å. Interference image of calcite (left up), normalized transmittance profile (right up), spectral Image (left down) near 16500Å, spectral profile and the marked calibration lines (right down).

CASE 3 (Fig. 2.9c):

Central wavelength: 10830.0Å

Temperature: 21.0 ± 0.1 °C

Wavelength range: $\lambda = 10830.0 \pm 30.0$Å

Calibration lines: $\lambda(L_1) = 10811.110$Å, $\lambda(L_2) = 10843.876$Å

Spectral resolution: r = 0.31967Å/pixel

Wavelength separation: $p = 19.943$ pixel, i.e., $p = 6.3751$Å

$$\mu \approx -\frac{\lambda^2}{pd} \approx -0.175251 \pm 8.7\times10^{-4} \tag{2.38}$$

CASE 4 (Fig. 2.25d):

Central wavelength: 11970.0Å

Temperature: 21.0 ± 0.1 °C

Wavelength range: $\lambda = 11970.0 \pm 30.0$Å

Calibration lines: $\lambda(L_1) = 11949.739$Å, $\lambda(L_2) = 11991.560$Å

Spectral resolution: r = 0.31563Å/pixel

Wavelength separation: $p = 24.725$ pixel, i.e., $p = 7.8040$Å

$$\mu \approx -\frac{\lambda^2}{pd} \approx -0.174891 \pm 7.2\times10^{-4} \tag{2.39}$$

CASE 5 (Fig. 2.25e):

Central wavelength: 12400.0Å

Temperature: 21.0 ± 0.1 °C

Wavelength range: $\lambda = 12400.0 \pm 30.0$Å

Calibration lines: $\lambda(L_1) = 12390.154$Å, $\lambda(L_2) = 12422.995$Å

Spectral resolution: r = 0.31337Å/pixel

Wavelength separation: p = 26.615 pixel, i.e., p = 8.3245Å

$$\mu \approx -\frac{\lambda^2}{pd} \approx -0.175947 \pm 6.8\times10^{-4} \tag{2.40}$$

CASE 6 (Fig. 2.25f):

Central wavelength: 12900.0Å

Temperature: 21.0 ± 0.1 °C

Wavelength range: λ = 12900.0 ± 30.0Å

Calibration lines: $\lambda(L_1)$ =12879.759Å, $\lambda(L_2)$ =12899.831Å

Spectral resolution: r = 0.30548Å/pixel

Wavelength separation: p = 28.850 pixel, i.e., p = 8.8131Å

$$\mu \approx -\frac{\lambda^2}{pd} \approx -0.179864 \pm 6.6\times10^{-4} \tag{2.41}$$

CASE 7 (Fig. 2.25g):

Central wavelength: 15110.0Å

Temperature: 21.0 ± 0.1 °C

Wavelength range: λ = 15110.0 ± 30.0Å

Calibration lines: $\lambda(L_1)$ =15094.685Å, $\lambda(L_2)$ =15122.374Å

Spectral resolution: r = 0.30522Å/pixel

Wavelength separation: p = 40.113 pixel, i.e., p = 12.2429Å

$$\mu \approx -\frac{\lambda^2}{pd} \approx -0.177638 \pm 4.9\times10^{-4} \tag{2.42}$$

CASE 8 (Fig. 2.25h):

Central wavelength: 15650.0Å

Temperature: 21.0 ± 0.1 °C

Wavelength range: λ = 15650.0 ± 30.0Å

Calibration lines: $\lambda(L_1)$ =15621.656Å, $\lambda(L_2)$ =15662.012Å

Spectral resolution: r = 0.30457Å/pixel

Wavelength separation: p = 43.188 pixel, i.e., p = 13.1538Å

$$\mu \approx -\frac{\lambda^2}{pd} \approx -0.177367 \pm 4.6\times10^{-4} \tag{2.43}$$

CASE 9 (Fig. 2.25i):

Central wavelength: 15960.0Å

Temperature: 21.0 ± 0.1 °C

Wavelength range: λ = 15960.0 ± 30.0Å

Calibration lines: $\lambda(L_1)$ =15941.836Å, $\lambda(L_2)$ =15980.735Å

Spectral resolution: r = 0.30402Å/pixel

Wavelength separation: p = 45.188 pixel, i.e., p = 13.7038Å

$$\mu \approx -\frac{\lambda^2}{pd} \approx -0.177062 \pm 4.4\times10^{-4} \tag{2.44}$$

CASE 10 (Fig. 2.25j):

Central wavelength: 16500.0Å

Temperature: 21.0 ± 0.1 °C

Wavelength range: λ = 16500.0 ± 30.0Å

Calibration lines: $\lambda(L_1)$ =16486.667Å, $\lambda(L_2)$ =16517.232Å

Spectral resolution: r = 0.30203Å/pixel

Wavelength separation: p = 48.692 pixel, i.e., p = 14.6923Å

$$\mu \approx -\frac{\lambda^2}{pd} \approx -0.176511 \pm 4.1\times10^{-4} \tag{2.45}$$

The measurement errors presented in Eq. 2.36 to Eq. 2.45 are provided by the measurement errors of p and d. The measurement precision of p, Δp, could be down to 0.1 pixel by amplifying the profile when analyzing the data, so Δp = r × 0.1pixel in angstrom. Where, r is the spectral resolution (Å/pixel). Eq. 2.24 can yield the error, $\Delta\mu$, in Eq. 2.36 to Eq. 2.45. Systematic errors due to instruments (e.g., the axis errors of polarizers, calcite) can be neglected because the wavelength positions of peaks or valleys in the profile curves of the calcite interference images are not changed with the axis errors (detailed discussion in Appendix B). In summary, Table 2.3 presents the measured values of birefringent index of calcite from 1.00μm to 1.65μm at room temperature. The measured values of the birefringent index and measured errors are shown in Table 2.3.

Table 2.3 Measured Values of Birefringent Index from 1.00μm to 1.65μm at 21.0°C

Central Wavelength (Å)	Measured Value of μ	Measured Error (10^{-4})
10050	-0.17444	± 10.0
10140	-0.17667	± 10.0
10830	-0.17525	± 8.7
11970	-0.17489	± 7.2
12400	-0.17595	± 6.8
12900	-0.17986	± 6.6
15110	-0.17764	± 4.9
15650	-0.17737	± 4.6
15960	-0.17706	± 4.4
16500	-0.17651	±4.1

The chosen wavelengths are not uniformly separated because some wavelength ranges cannot be used due to the very strong absorption lines in these ranges,

such as from 1.3μm to 1.5μm, and from 1.1μm to 1.2μm. Therefore we cannot obtain data in these wavelength ranges.

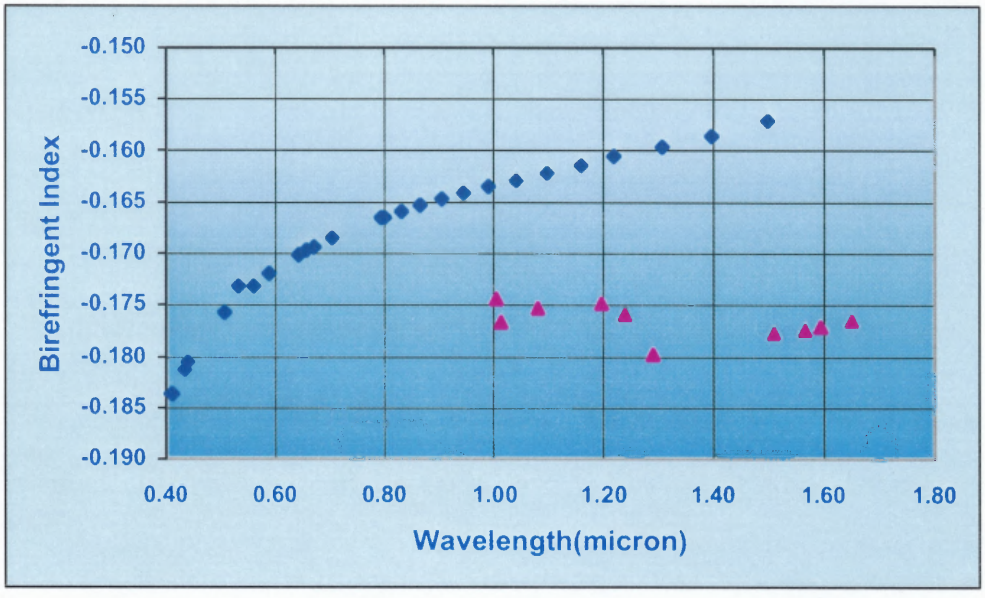

Figure 2.26 Comparison of the measured values of birefringent indices of calcite at different wavelengths with the data in literature[33, 34]. Diamonds: values in literature, triangles: measured values.

Figure 2.26 presents a comparison of the measured values of birefringent index of calcite from 1.0μm to 1.65μm with the data in the literature[33, 34]. The measured values of μ are much different from that in the literature. The general trend seems to be that there are differences in the values of μ depending on the origin of the calcite crystals. However, this difference is only of order of 10^{-5}. But, the difference between the measured value and that in literature is up to 0.2. This may be due to measurement errors before because some data in the literature were almost a hundred years old! The measured value of μ at 1.56μm was used in our near-IR birefringent filter design and

good results were obtained. The optical design and test results of this filter will be discussed in the next section.

2.3 Optical Design of the Near-Infrared Birefringent Filter

2.3.1 Scheme and General Considerations of the Optical Design of the Near-IR Birefringent Filter

In section 2.1.3, a discussion of the magnetograph that includes a prefilter, a magnetic analyzer, a near-IR birefringent filter, an IR Fabry-Perot and an IR camera was presented. Except for the birefringent filter, the other parts of the magnetograph are commercially available. Birefringent filters cannot be obtained commercially because of their special requirements. Therefore, the design and fabrication of the birefringent filter are the most important in the near-IR magnetograph system.

Specifications of such a birefringent filter are as follows:

Aperture:	ϕ 35.0mm
FWHM:	$\leq$ 2.5Å
Working Temperature:	43 $\pm$ 0.05 °C
FSR:	$\geq$ 40.0Å
Wavelength Tuning Range:	~15648.5Å $\pm$ 10.0Å

A scheme of the optical design of this near-IR birefringent filter is presented in Fig. 2.27. Four calcite elements are placed between five parallel polarizers. The wavelength tuning units are liquid crystal variable retarders controlled electronically. A few important aspects have been considered during the design of a birefringent filter. These are as follows:

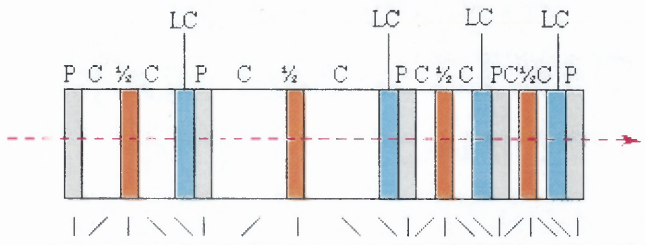

Figure 2.27 Scheme of the optical design of the near-IR birefringent filter. P: polarizer, C: calcite, ½: wide-field half waveplate, LC: liquid crystal variable retarder, |: represents polarization direction of the polarizers or the direction of optical axis of the ½ waveplates, ⁄ or \ : represents the direction of the optical axis of the calcite plate or the liquid crystal retarder.

1. FWHM and FSR:

The FWHM of the 1st (thickest) calcite element, $\Delta\lambda_{FWHM}$, is 2.5Å. This means

$$n_1 = \frac{\mu d_1}{\lambda} \Rightarrow \Delta n_1 \approx -\frac{\mu\, d_1}{\lambda^2}\Delta\lambda \Rightarrow \frac{1}{2} \approx -\frac{\mu\, d_1}{\lambda^2}\Delta\lambda_{FWHM}. \tag{2.46}$$

Hence,

$$d_1 = -\frac{\lambda^2}{\mu\Delta\lambda_{FWHM}} = -\frac{15648.5^2}{2\times(-0.1770494)\times 2.5}(\text{Å}) \approx 27.662\ (\text{mm}). \tag{2.47}$$

The variation of the birefringent index of calcite within a range of $\Delta\lambda_{FWHM}$ is ignored in the deduction above. In order to get maximum transmittance at 15648.5Å for the 1st element, its retadation should be an integer. If d_1 = 27.662mm, we have

$$n_1 = \frac{\mu d_1}{\lambda} = \frac{(-0.1770494)\times 27.662\times 10^7}{15648.5} = -3129.72\,. \tag{2.48}$$

The integer, for n_1, may be chosen to be equal to –3128, a value close to that in Eq. 2.48. The retardations for the thinner elements can still be integers as half the retardation of the

previous element, i.e., -1564 for the 2nd element, -782 for the 3rd element and -391 for the 4th element. In reverse, we can recalculate the thickness of the 1st element,

$$d_1 = -\frac{n_1\lambda}{\mu} = \frac{(-3128)\times 15648.5}{(-0.1770494)} \approx 27.647mm\,. \tag{2.49}$$

For the thinner elements, their thickness is half the thickness of the previous element, but their FWHM is twice of the FWHM of the previous element. Therefore we have

1st element	$d_1 \approx 27.647$mm	$\Delta\lambda_{FWHM} = 2.5$Å,
2nd element	$d_2 \approx 13.823$mm	$\Delta\lambda_{FWHM} = 5.0$Å,
3rd element	$d_3 \approx 6.912$mm	$\Delta\lambda_{FWHM} = 10.0$Å,
4th element	$d_3 \approx 3.456$mm	$\Delta\lambda_{FWHM} = 20.0$Å.

The Free Spectral Range (FSR) of a birefringent filter is actually two times the FWHM of the thinnest element. In our filter, the FSR could be up to 40.0Å (as required in the specifications) if the 4th element is the thinnest one. So we choose four elements in this near-IR birefringent filter.

2. Wide-field configuration

Generally, a birefringent filter is used in a collimated light. Nevertheless, a collimating light is not always a perfect parallel beam. If the incident light beam is not normal to the surface of the birefringent crystal plates, there will be an error in the retardation of the crystal.

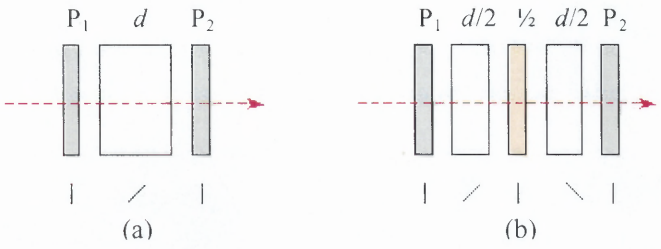

Figure 2.28 An element of a birefringent filter with wide-field configuration. (a) A simple element, (b) An element with a wide field configuration.

In order to reduce the retardation errors, a wide-field configuration for a crystal element should be considered. A wide-field configuration indicates that the calcite plate of an element is split into two equally thick parts and a half waveplate is sandwiched between them (Fig. 2.28). Therefore the four elements in Fig. 2.27 are all designed in wide field configuration.

3. The wavelength tunable unit

In this near-IR birefringent filter, liquid crystal variable retarders are chosen as the wavelength tunable units. Compared with the most popular method of tuning (Fig. 2.8), the advantages of the liquid crystal variable retarder are:

- Easier control for the tuning of pass-band,
- Stable during operation after encapsulation in the modules,
- Good enough image performance.
- No moving mechanical parts – reduce the possibility of breakdown of control system due to the moving parts.

- Instead of silicon oil inside an insulation tube to hold the optical components, some kind of grease can be used between the faces of the components to reduce scattering light. The oil leak problem in the traditional design of birefringrnt filters could be solved.

From Fig. 2.27, this near-IR birefringent filter includes five IR polarizers, four half waveplates, four liquid crystal viable retarders and four pair of calcite plates. The design parameters are shown in Table 2.4.

Table 2.4 Design Parameters of the Birefringent Filter

Element #	FWHM (Å)	Material	Thickness (mm)	Retardations	Field of View	Shape/Size
1	2.5	Calcite	13.831×2	3128	Wide	Octagon/37.00×37.00mm
2	5.0	Calcite	6.916×2	1564	Wide	Octagon/37.00×37.00mm
3	10.0	Calcite	3.458×2	782	Wide	Octagon/37.00×37.00mm
4	20.0	Calcite	1.729×2	391	Wide	Octagon/37.00×37.00mm
Waveplate	--	Quartz	2.00~3.00mm	½	--	Octagon/37.00×37.00mm
Polarizer	--	HR	2.00~3.00mm	--	--	--

The transmission, τ, of this filter is given by:

$$\tau = \cos^2(\pi \frac{\mu d_1}{\lambda} + \Delta_1)\cos^2(\pi \frac{\mu d_2}{\lambda} + \Delta_2)\cos^2(\pi \frac{\mu d_3}{\lambda} + \Delta_3)\cos^2(\pi \frac{\mu d_4}{\lambda} + \Delta_4), \qquad (2.50)$$

where, Δ_i, i=1, 2, 3, 4, are the phase differences given by the liquid crystal variable retarders to shift the wavelength of the pass-band within a period in every element. Figure 2.29 shows the numerical modeling of the transmittance of every element and the filter. These figures can be compared with the test results under a spectrograph.

This birefringent filter is designed to be tunable so that the pass band can cover the two magnetically sensitive lines at FeI 15648.5 Å (g = 3) and FeI15652.8 Å (g = 1.53). Figure 2.30 shows shift of the pass-band of this birefringent filter. The advantages of a wavelength tunable filter include:

- Wavelength tuning of the pass-band at different spectral lines, so it is realizable to use the two spectral lines (FeI 15648.5Å with $g = 3$ and FeI15652.8Å with $g = 1.53$) to measure weak solar magnetic fields;
- Scanning of solar spectral line profiles;
- Easy to do calibration and re-calibration of the pass-band.

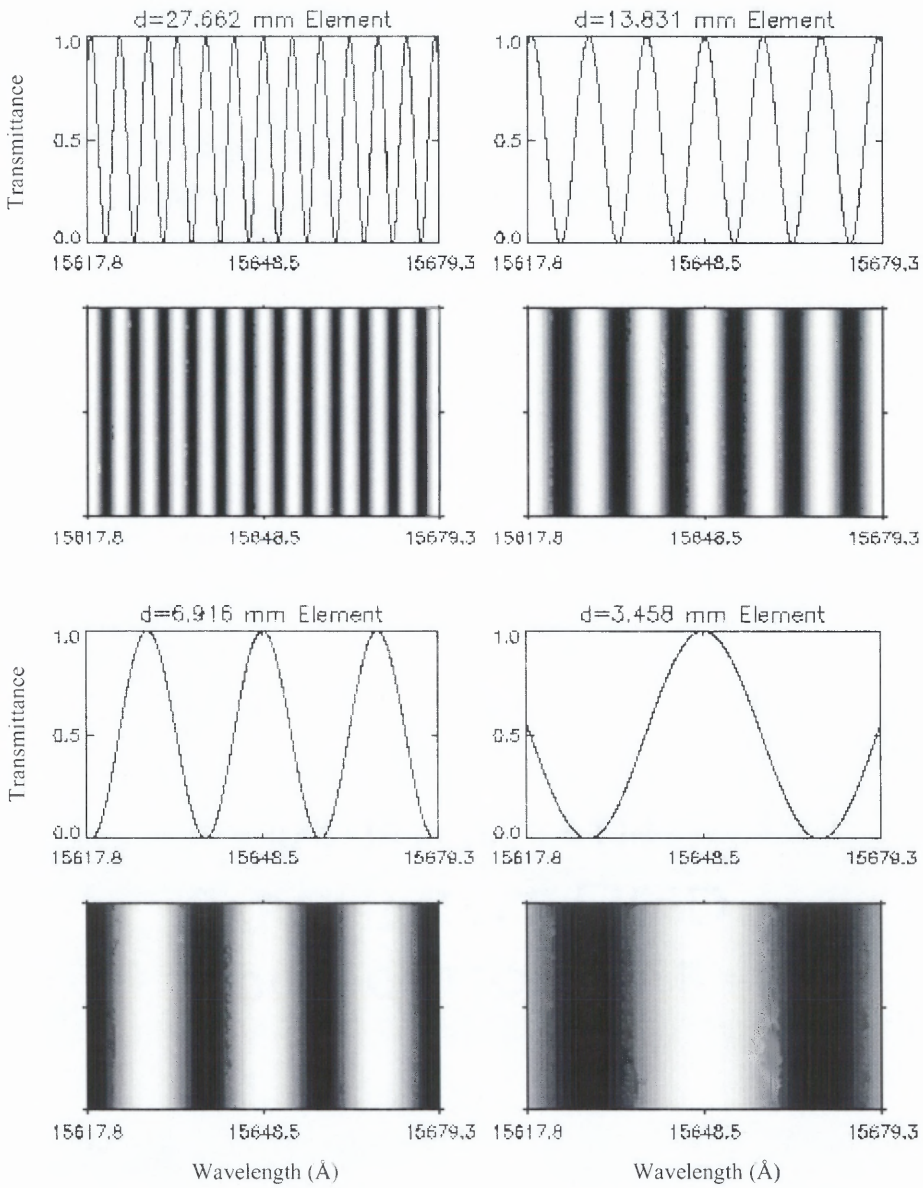

Figure 2.29 Numerical modeling of the transmittance of each calcite element.

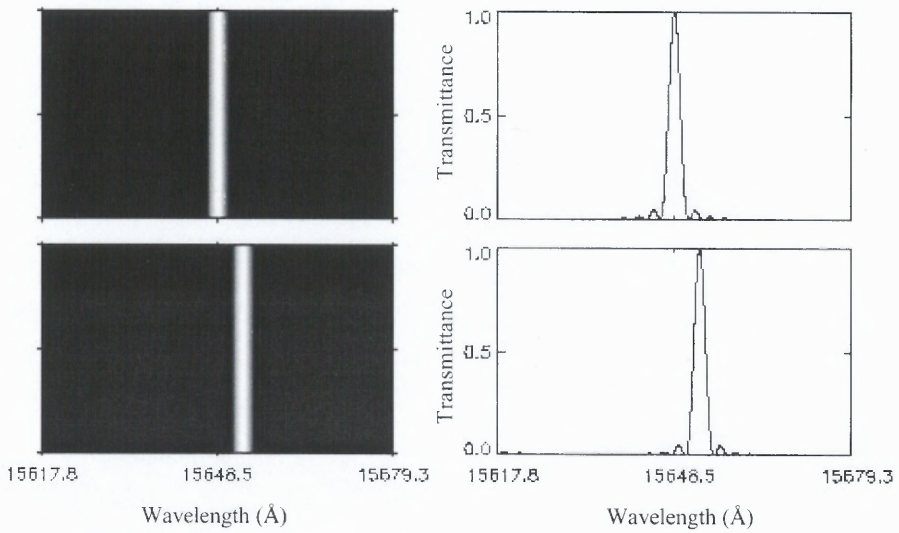

Figure 2.30 Numerical modeling of the pass-band of the near-IR birefringent filter. In the upper panels, pass-band of the near-IR birefringent filter at 15648.5Å, and in the lower panels, the pass-band of this filter shifted to 15652.9Å.

2.3.2 Infrared Polarizer

Five pieces of infrared polarizers will be used in the birefringent filter. The HR type polarized film, manufactured by the Polariod Company, was chosen as the polarizers. At 15600 Å, the transmission of the HR polarizer is about 34.5%. The parallel transmission τ_p is about 23.8% and the crossed transmission τ_c is about 0.00284. This is good enough for use in the birefringent filter. From the data above, we can obtain the absorptivity to be about (34.5%-23.8%)/34.5% = 31.0%, i.e., the transmission of a polarizer for a polarized light beam is about 69%. In fact, better polarized film whose transmission is larger than that above, can be obtained because small areas from a large film can be chosen that yield high transmission. Another kind of polarizer with very high transmission is developed by Corning, Inc. The shortcoming of this kind of polarizer is its small size (only up to 20 ×

20mm). Therefore, there is an option, which enables us to upgrade the polarizers in the future when the larger ones are available, in the mechanical design of the near-IR birefringent filter.

The polarizer film obtained from Polaroid Company is usually sandwiched between two celluloid layers for protection. These celluloid layers need to be removed them from the two sides of the film by use of acetone solution or other chemical reagents because they produce a strong, nasty scattering of light [38]. After removing the layers, we should glue the films with two protecting optical glass plates to reduce the reflection from the surfaces.

2.3.3 Half (1/2) Waveplate

The half waveplates are used for the wide-field configuration elements. Using equation $\mu d_{1/2} / \lambda = 1/2$, we obtain the thickness of a zero-order half waveplate for quartz as the material of choice:

$$d_{1/2} = \frac{\lambda}{2\mu_q} = \frac{15648.5\times10^{-7} mm}{2\times0.00879} \approx 0.089 mm . \tag{2.51}$$

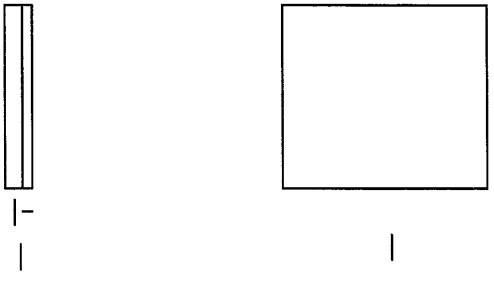

Figure 2.31 Design of half waveplate.

From mechanical considerations, the numerical value of $d_{1/2}$ in Eq. 2.51 is very small. We can design the waveplate consisting of two crossed quartz plates with a thickness difference between them of 0.089mm, i.e. $\Delta d = d_1 - d_2 = d_{1/2}$. The optical axis of the waveplate will be along that of the thicker plate (Fig. 2.31). These half waveplates were manufactured in Nanjing Astronomical Instrument Factory, Nanjing, P. R. China.

2.3.4 Estimation of the Transmittance of the Near-IR Birefringent Filter

For the birefringent filter, we know that the transmission of the HR polarizer is 34.5% and its absorptance is 10.7%. Assuming no absorption in the waveplates and calcites, the transmission of the birefringent filter is about:

$$T_b = 34.5\% \cdot (89.3\%)^4 \approx 21.94\%. \tag{2.52}$$

2.3.5 Testing the Four Pairs of Calcite with a Spectrograph

The key components in the near-IR birefringent filter, considered in this work, are the four pairs of calcite plates. These calcite plates were manufactured in Nanjing Astronomical Instrument Factory, Nanjing, P.R. China. Calcite is a natural single birefringent crystal. It is most often used as a material of physical optical component because of its larger birefringent index and pure optical performance. After complete polishing, four pairs of calcite crystals were tested for use in the IR birefringent filter using the spectrograph at BBSO. The setup of the test instruments is the same as in Fig. 2.21. The working temperature is set to 43°C with an accuracy ±0.1°C. Polarizer P_1 is parallel to P_2 and a half waveplate is sandwiched between a pair of calcite crystals just as in the wide field configuration.

The test results in Fig. 2.32 show the transmittance images of element #1(d_1), #2(d_2), #3(d_3) and #4(d_4) respectively. To simulate the passband of the filter, a), c) and d) are slightly shifted to align the peaks. This task will be performed by the liquid crystal variable retarders in the working filter. In Table 2.5, the experimentally measured values of FWHM of each pair of calcite element are listed and these are the average between the peaks near FeI15648.5Å. The FWHM of the simulated passband of the near-IR filter is approximately 2.254Å.

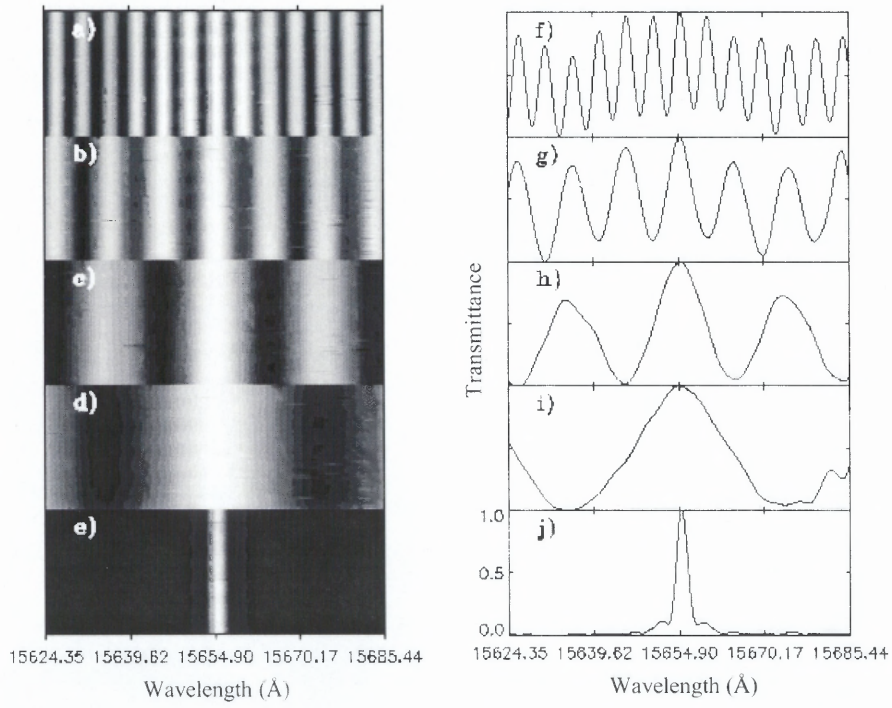

Figure 2.32 Transmittance images of each pair of calcite and simulated passband of the near-IR birefringent Filter. a) ~ d): transmittance images of the calcite element, f) ~ i): normalized profiles of the transmission images, e): simulated passband of the filter (product of image a), b), c) and d)), j): normalized simulation profile of the passband of filter.

Table 2.5 Measurement Results for Every Pair of Calcite Used in the Near-IR Birefringent Filter

Transmittance Image	Separation between Two Peaks (Å)	FWHM (Å)
a)	4.813	2.407
b)	9.630	4.815
c)	19.13	9.565
d)	38.52	19.26
Simulated passband of the filter	--	**2.254**

The test results presented in Table 2.5 show that the pass-bands of the four pairs of calcite are matched very well with each other for reducing the non-zero side-bands. On the other hand, the half waveplates at 15648.5Å, used between each pair of calcite plates, have been shown to be of good quality. This near-IR birefringent filter is being assembled by Cambridge Research & Instrument, Inc., Boston.

2.4 Characteristics of the Near-Infrared Fabry-Perot Filter

2.4.1 Basics of the Fabry-Perot Filter

Fabry-Perot filters are widely used in modern optics as resonators for allowing specific wavelengths of light to transmit. In its simplest configuration, the Fabry-Perot etalon consists of two plane, parallel, highly reflecting surfaces separated by some distance d. A simple scheme of optical construction of a Fabry-Perot is shown in Fig. 2.33. The reflecting surfaces are formed by a very thin silver or aluminum film, or multi-layer dielectric films on the surface of glass plates. The enclosed air gap generally varies from several millimeters to several centimeters when the device is used interferometrically.

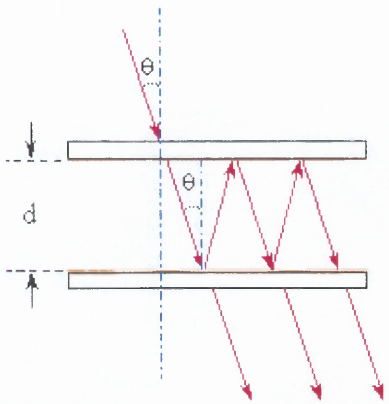

Figure 2.33 A simple optical scheme of a Fabry-Perot filter.

If the gap can be mechanically varied by moving one of the mirrors, the device is referred to as a Fabry-Perot interferometer. If the mirrors are held fixed and adjusted for parallelism by screwing down on some kind of spacer, it is said to be a Fabry-Perot etalon.

Figure 2.33 shows one ray as it propagates from some point *S* on the source through the etalon. Entering by way of the partially silvered plate, it goes through multiple reflection within the gap. The Fabry-Perot etalon operates by multiple beam interference. Light that is incident from the top of the first reflection surface is split by reflection into a series of parallel-transmitted rays. The ray is partially transmitted at each reflection from the second surface. For simplicity, Figure 2.33 does not show the change in direction of propagation of light upon refraction, nor does it show the rays that pass through the first surface and propagate upward.

When the difference in optical path length between the rays transmitted at successive reflections is such that the emerging waves are in the same phase, constructive interference will occur and the Fabry-Perot will show a maximum in transmission.

If this condition does not hold, the interference between successive emerging rays will be destructive and the transmission will be relatively low. It is a common practice to incorporate a lens and a viewing screen when using the Fabry-Perot, as shown in Fig. 2.34. This is necessary for bringing rays to a common point before the results of the interference can be detected.

The phase difference between two successive rays is given by:

$$\delta = 2\pi \frac{2n'd\cos\theta}{\lambda}. \tag{2.53}$$

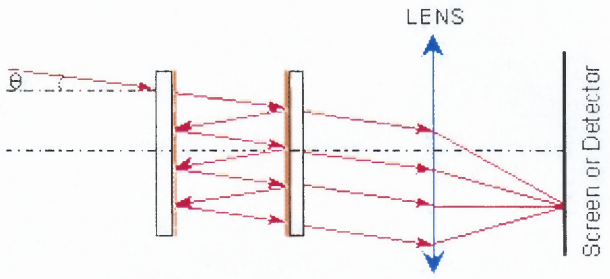

Figure 2.34 Interference in a Fabry-Perot etalon.

where λ = The wavelength of the radiation in vacuum (or air),

d = The separation of the reflecting surfaces,

n' = The index of refraction of the material between the reflecting surfaces,

θ = The angle of incidence, as shown in Fig. 2.33.

The transmission intensity distributions is[6]:

$$\frac{I^{(t)}}{I^{(i)}} = \frac{1}{1+\dfrac{4R}{(1-R)^2}\sin^2(\delta/2)} = \frac{1}{1+A\sin^2(\delta/2)}. \tag{2.54}$$

where, $A = \dfrac{4R}{(1-R)^2}$. From Eq. 2.54, we can get for fixed space separation, d,

$$\begin{cases} I^{(t)}/I^{(i)} \text{ is maximum when } \delta = 2m\pi, \ m \text{ is an integer,} \\ I^{(t)}/I^{(i)} \text{ is minimum, when } \delta = 2\pi\left(m + \dfrac{1}{2}\right), \ m \text{ is an integer.} \end{cases}$$

This means the maxima of transmission are at:

$$m = \frac{2n'd\cos\theta}{\lambda_0} \text{ for a specific wavelength } \lambda_0. \tag{2.55}$$

The product $n'd$ is referred to as the optical thickness or optical length to distinguish it from mechanical thickness or length. Because the wavelength is usually much smaller than the physical separation between the reflecting surfaces, the integer N will be large, usually on the order of 10,000 to 100,000 depending on the mirror separation. The integer m is of the order of the interference. In most cases of interest, the medium between the reflecting surfaces will be air and the index of refraction n' will be taken to be unity.

For a given angle of incidence, the transmittance as a function of wavelength is shown in Fig. 2.35. The reflectivity of the surface is very important in determining the cleanness of the passband of the filter.

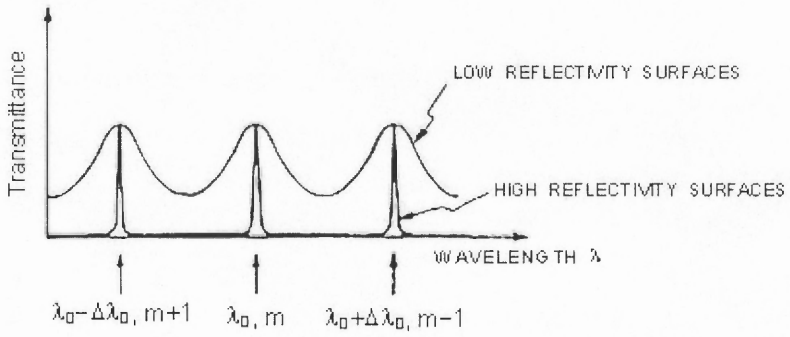

Figure 2.35 Fabry-Perot transmittance as a function of wavelength.

If Eq. 2.55 is satisfied by a particular combination of an integer m and wavelength λ_0, the interference between the transmitted rays will be constructive, and there will be a maximum in transmission. For other combinations, for example $m + 1$ and $\lambda_0 - f$, Eq. 2.55 will also be satisfied and there will be another maximum of transmission. The separation, ϕ, between maxima in transmission can be deduced from:

$$\begin{cases} m\lambda_0 = 2n'd\cos\theta, \\ (m+1)(\lambda_0 - f) = 2n'd\cos\theta, \end{cases}$$

therefore,

$$f \approx \frac{\lambda_0}{m}. \tag{2.56}$$

This is an important concept, referred as "free spectral range" (FSR), frequently used to indicate how nearly identical two wavelengths must be to produce adjacent, same-order fringes.

Another important concept is the Full Width of Half Maximum (FWHM) of the transmission pass-band of the Fabry-Perot. Let $\Delta\lambda_{FWHM}$ be the FWHM and the values of transmittance at $\lambda_0 \pm \Delta\lambda_{FWHM}$ are half of that at λ_0. Because

$$\frac{2n'd\cos\theta}{\lambda_0} = m, \qquad \text{and}$$

$$\delta = 2\pi \cdot \frac{2n'd\cos\theta}{\lambda_0 \pm \frac{\Delta\lambda_{FWHM}}{2}} \approx 2\pi \cdot \frac{2n'd\cos\theta}{\lambda_0}\left(1 \mp \frac{\Delta\lambda_{FWHM}}{2\lambda_0}\right)$$

$$= 2\pi m\left(1 \mp \frac{\Delta\lambda_{FWHM}}{2\lambda_0}\right), \tag{2.57}$$

we can get:

$$\sin^2\frac{\delta}{2} = \sin^2\left(m\pi \mp \frac{m\pi\Delta\lambda_{FWHM}}{2\lambda_0}\right)$$

$$= \sin^2\left(\frac{m\pi\Delta\lambda_{FWHM}}{2\lambda_0}\right)$$

$$\approx \left(\frac{m\pi\Delta\lambda_{FWHM}}{2\lambda_0}\right)^2, \ (\Delta\lambda_{FWHM} << \lambda_0). \tag{2.58}$$

Half maximum of the pass-band means:

$$\frac{I^{(t)}}{I^{(i)}} = \frac{1}{1 + A\sin^2(\frac{\delta}{2})} = \frac{1}{2}. \tag{2.59}$$

$$\Rightarrow \quad 1 + A\sin^2(\frac{\delta}{2}) = 2$$

$$\Rightarrow \quad A\sin^2(\frac{\delta}{2}) = A\left(\frac{m\pi\Delta\lambda_{FWHM}}{2\lambda_0}\right)^2 = 1$$

$$\Rightarrow \quad \frac{m\pi\Delta\lambda_{FWHM}}{2\lambda_0} = \frac{1}{\sqrt{A}}$$

$$\Rightarrow \quad \Delta\lambda_{FWHM} = \frac{\lambda_0}{m}\cdot\frac{2}{\pi\sqrt{A}}$$

$$\Rightarrow \quad \Delta\lambda_{FWHM} = \frac{2f}{\pi\sqrt{A}}. \tag{2.60}$$

In Eq. 2.60, $A = \frac{4R}{(1-R)^2}$ and $f \approx \frac{\lambda_0}{m}$ is the free spectral range. Combination of Eq. 2.56 and Eq. 2.60 will give another important concept, finesse F, the ratio of free spectral range and the FWHM:

$$\mathsf{F} = \frac{f}{\Delta\lambda_{FWHM}}$$

$$= \frac{\pi\sqrt{A}}{2} = \frac{\pi\sqrt{R}}{1-R}. \qquad (2.61)$$

Eq. 2.61 shows that the finesse, F, is a parameter describing the property of reflectivity of the surfaces. Figure 4.3 shows how the reflectivity, R, of the surfaces affects the transmission. If the reflectivity, R, is relatively low, the maxima in transmission will be broad and F will be low. On the other hand, if the reflectivity, R, is high, the maxima of transmission will be very narrow and sharp and F will be high.

2.4.2 Considerations for Testing the Characteristics of the Fabry-Perot Filter used in the Near-IR Filter System

The Fabry-Perot used in our near-IR filter system is ET70FS-1041 manufactured by SDL Queensgate, Ltd. It is shown in Fig. 2.36.

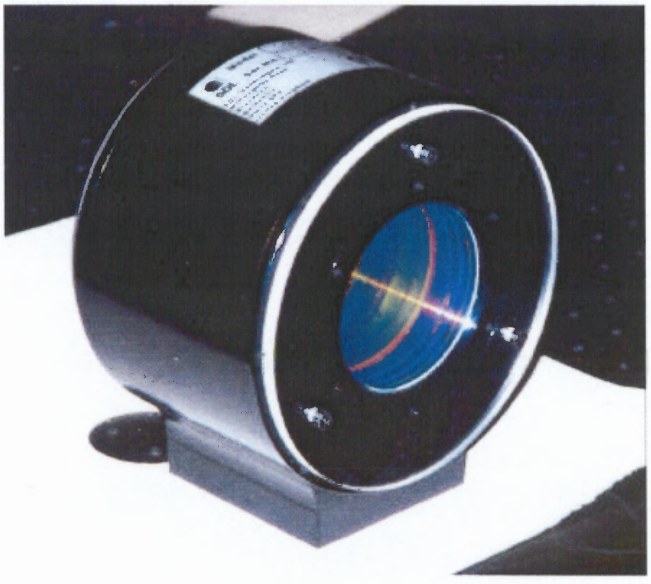

Figure 2.36 The near-IR Fabry-Perot filter ET70FS-104.

It is designed for use in the near-IR wavelength range between 1000nm to 1600nm in imaging mode. It will be used in combination with the near-IR birefringent filter discussed in section 2.3 to measure solar magnetic fields at 15648.5Å and 15652.9Å. This Fabry-Perot is tunable for its passband by changing the spacing with an interface of RS232C in the CS100 controller. In this section, the characteristics of this Fabry-Perot are discussed. Aspects for testing this Fabry-Perot are also considered before it is used as a part of the entire filter system.

2.4.2.1 Specifications of the Near-IR Fabry-Perot Filter. The specifications for the near-IR Fabry-Perot ET70FS-1041 are presented in Table 2.6[39].

Table 2.6 Specifications of the Fabry-Perot ET70FS-1041

Parameter	Specification
Clear Aperture	70mm
Surface Quality	λ/100 at 633nm
Wedge Angle	0 ± 1fringe
Mirror Spacing	2226μm (nominal)
Cavity Tuning Range	> 4.1μm
Operational Temperature Rang	0 °C to 50 °C
Nominal Finesse	60 at 1523nm
Coating Reflectivity	96% ± 2% from 1000 to 1600nm

The surface quality specification in Table 2.6 refers to the peak-to-valley departure from flatness of the matched pair of Fabry-Perot etalon mirrors measured at 633nm before the mirrors are coated.

The wedge angle specification refers to the wedge angle between the rear mirror surfaces and the front surfaces of the Fabry-Perot. Nominally, the rear surfaces of the etalon mirrors are wedged by 15 minutes of arc. But, for imaging purposes, the front and

rear mirror surfaces can be polished optically parallel to each other. This will eliminate 'ghost' reflections that are displaced from the main image when the etalon is used for two dimension spectral imaging. In ET70FS-1041, the wedge angle is 0 ± 1fringe.

For maximum possible mount stability, ET70FS-1041 is mounted in a sealed cell with high efficiency anti-reflection (AR) coated windows. This eliminates the impact of changes in environmental pressure and humidity on both the capacitance micrometers and on the optical cavity length.

The arrangement of capacitance sensors and piezoelectric (PZT) actuators to be found in the Fabry-Perot etalon is shown schematically in Fig. 2.37. Three piezo-electric actuators (a, b, c) are used to tune the cavity while the capacitance sensors Cx_1, Cy_1 etc., fabricated onto the mirror surface, are used to sense changes in parallelism and cavity length.

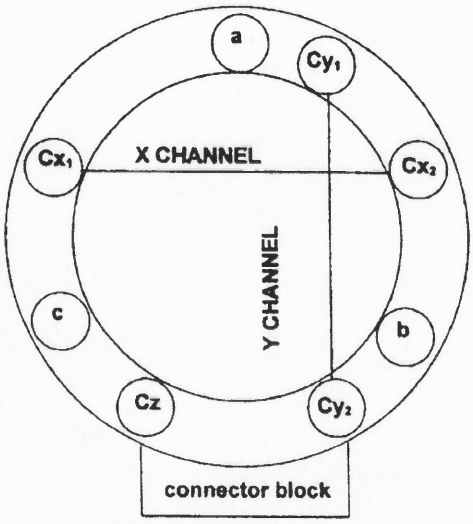

Figure 2.37 Definition of the X, Y and Z axes of the Fabry-Perot.

Parallelism information is obtained by comparing Cx_1 with Cx_2 (X-channel) and Cy_1 with Cy_2 (Y-channel). Cavity length control is achieved by referencing C_z to a stable fixed reference capacitor (Z-channel).

The X and Y capacitance bridges can be un-balanced by means of the front panel controls or the interface to compensate for differences in micrometer capacitor values when the plates are parallel. Varying the balance will cause the plates to tilt so they can be accurately aligned. Similarly the Z channel can be un-balanced causing the plate spacing to vary enabling the etalon to be tuned to a particular wavelength.

Figure 2.38 A picture of the CS100 controller (top).

The CS100 controller (Fig. 2.38) is used for stabilizing the spacing and parallelism of the Fabry-perot, ET70FS-1041. It is a three-channel controller that uses capacitance micrometers and PZT actuators, incorporated into the Fabry-Perot, to monitor and correct errors in mirror parallelism and spacing. Two channels (X-channel and Y-channel)

control the parallelism and the third (Z-channel) maintains spacing by referencing the cavity length-sensing capacitance micrometer to a fixed reference capacitor. The cable loom and connectors are shown on the top of Fig. 2.39. The CS100 can be operated manually from panel controls, or under computer control using RS232C interface. The front panel of the CS100 controller is shown in Fig. 2.40. The indications of the controls or indicators are described in Table 2.7. The rear panel of the CS100 controller is shown in Fig. 2.41. The indications of the connectors are given in Table 2.8.

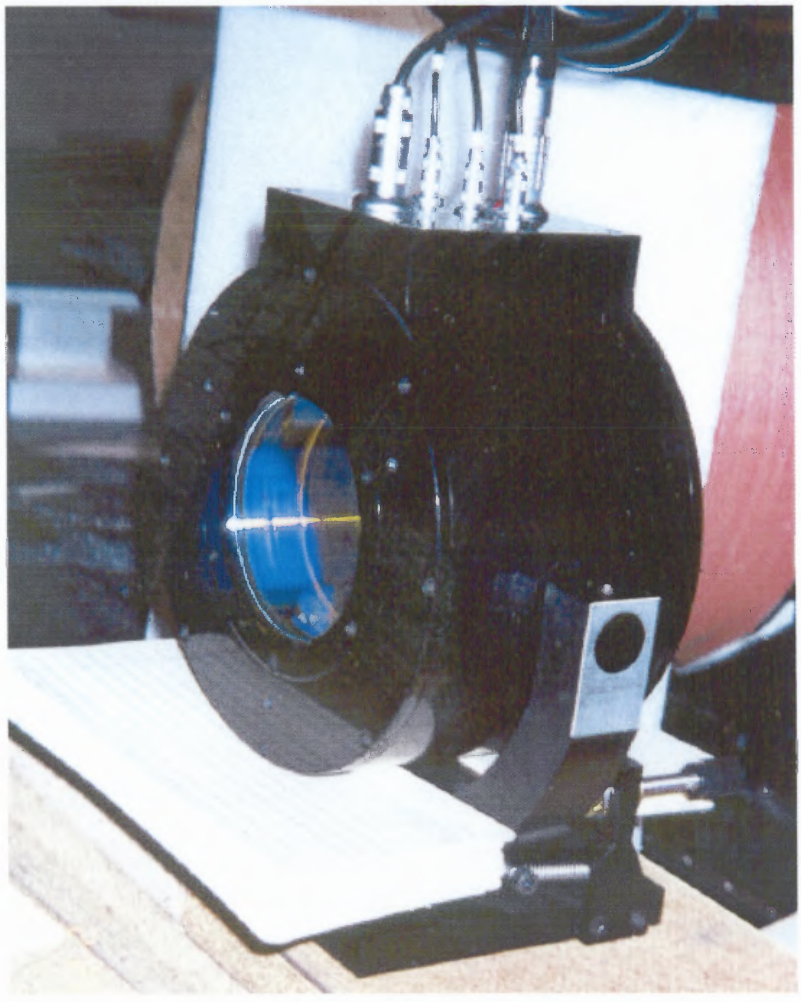

Figure 2.39 The near-IR Fabry-Perot filter ET70FS-1041 with the connectors.

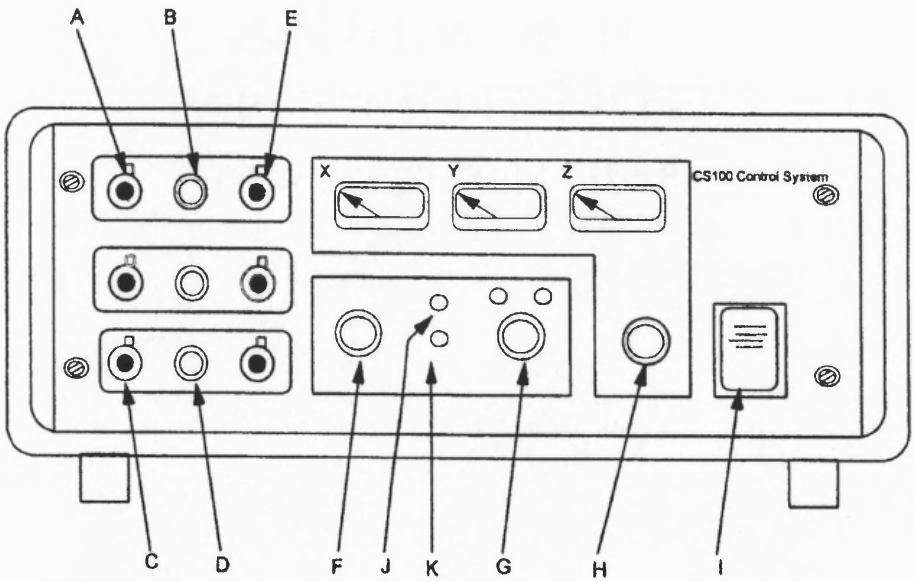

Figure 2.40 The front panel of the CS100 controller.

Table 2.7 Controls/Indicators of the Front Panel of the CS100 Controller

	Controls/Indicators	Comments
A	PARALLELISM	Fine 10 turn positions X and Y
B	PARALLELISM	Coarse switch X and Y
C	SPACING	Fine Z
D	SPACING	Coarse Z
E	QUADRTURE BALANCE	X, Y and Z
F	RESPONSE TIME	
G	BALANCE/OPERATE	Indicators show status
H	METER DISPLAY	Selects Quadrature error/offset
I	POWER	With indicator
J	OUT OF RANGE	Indicates X, Y and Z bridges out of range
K	DISABLED	Front panel controls disabled via interface

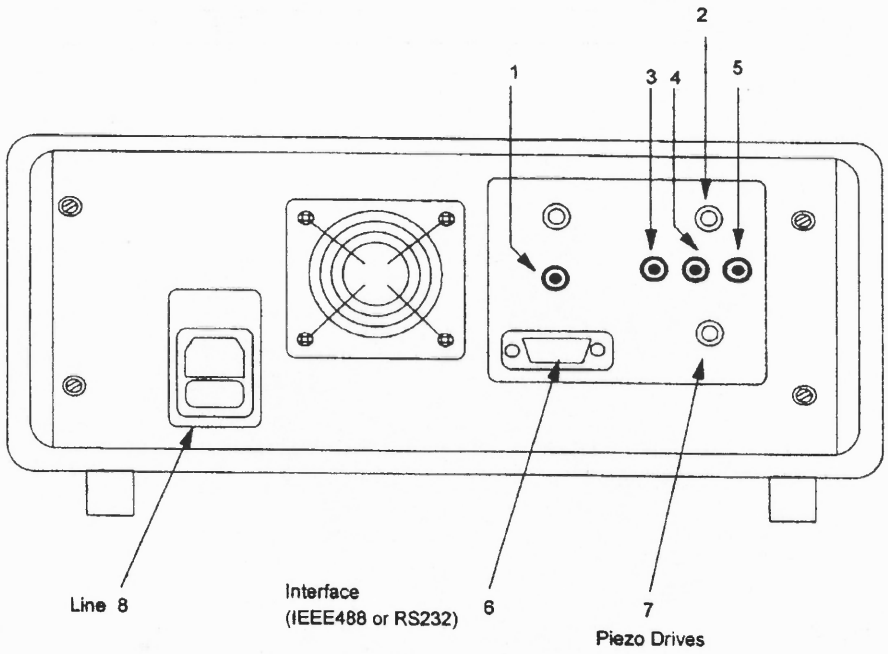

Figure 2.41 The rear panel of the CS100 controller.

Table 2.8 Connector Descriptions of the Rear Panel of the CS100 Controller

Connectors			
Item No.	Type	Purpose	Comments
1	LEMO PSA 0S 302 CLLC 37	Z-MODULATION	
2	LEMO PSA 1S 305 CLLC 37	BRIDGE DRIVES	PINS 1,2,3,4
3	LEMO PSA 00 250 CLLC 27	X-ERROR SIGNAL	
4	LEMO PSA 00 250 CTLC 27	Y-ERROR SIGNAL	
5	LEMO PSA 00 250 CTLC 27	Z-ERROR SIGNAL	
6	AMPH.57FE-40240-20S D1 (IEEE) OR AMPH. 17D-B-FR -A-25-S(RS232)	INTERFACE	CONNECTOR TYPE OPTIONAL
7	LEMO PSA 2S 306 CLLC 42	PIEZO DRIVES	
8	BULGIN PF0011/63/30	LINE	I.E.C/MAINS PLUG

The high reflective coating curve of the front mirror surfaces in the ET70FS-1041 is shown in Fig. 2.42. From this curve, the reflectivity $R \approx (100\text{-}5)\% = 0.95$, the finesse can be given by Eq. 4.9:

$$F = \frac{\pi\sqrt{A}}{2} = \frac{\pi\sqrt{R}}{1-R}$$

$$\approx \frac{\pi \times \sqrt{0.95}}{1-0.95} \approx 61.24 . \qquad (2.62)$$

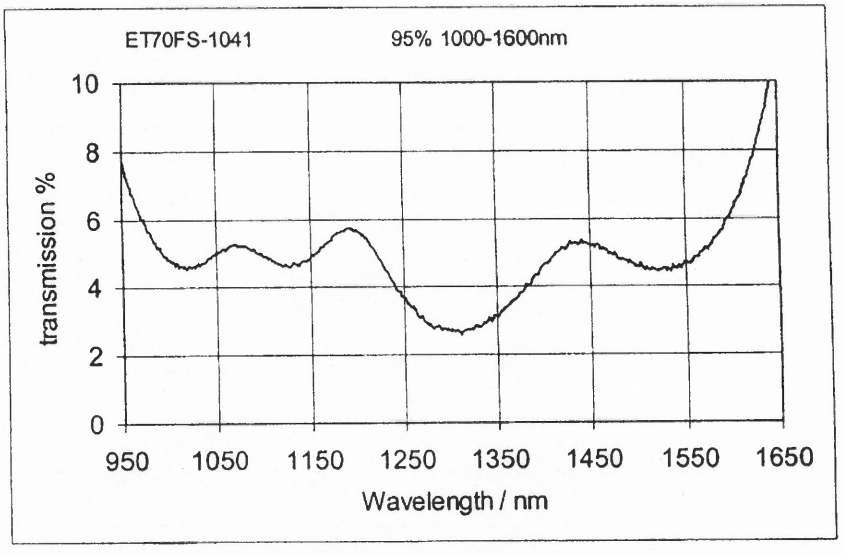

Figure 2.42 The etalon high reflective coating curve of the ET70FS-1041.

On the other hand, the anti-reflective curve of the rear mirror surfaces of in the ET70FS-1041 is shown in Fig. 2.43. The reflectivity is about 0.2% to 0.5% near 1.56μm, hence, the transmission is more than 99.5%. The coating curves (Fig. 2.42 and Fig. 2.43) are provided by SDL Queensgate, Ltd. which are only representative of the average expected reflectivity and have no information regarding the coating uniformity.

Therefore, the surface flatness and surface roughness should be measured in the testing of the Fabry-Perot filter.

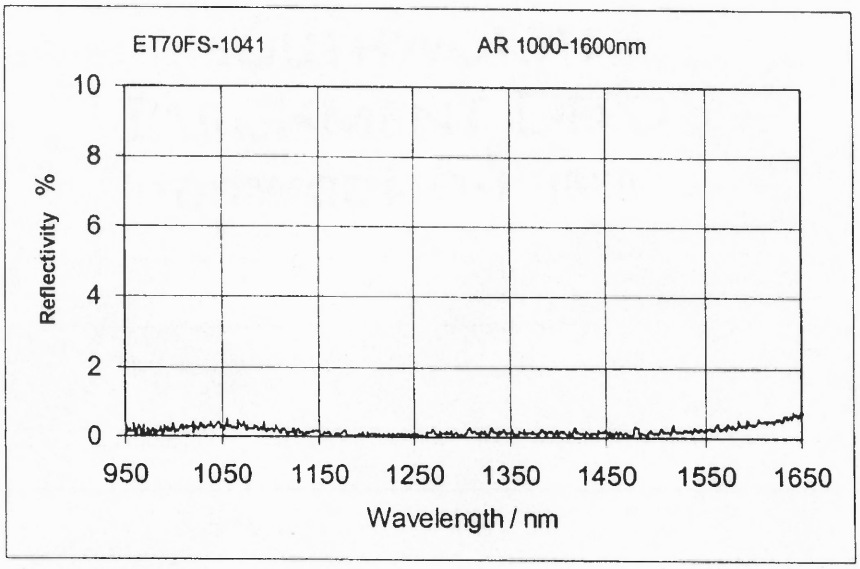

Figure 2.43 The anti-reflective coating curve of the rear mirror surface in the ET70FS-1041.

2.4.2.2 Considerations for testing the near-IR Fabry-Perot Filter. The specifications of the near-IR Fabry-Perot filter, ET70FS-1041, need to be measured with near-IR laser as the light source in the laboratory and on the 26-inch telescope at BBSO. The laser light beam of the laser is highly monochromatic, so a wide (up to 50Å) interference prefilter can be in front of Faby-Perot to be tested. Before testing the Fabry-Perot filter, the etalon needs to be aligned due to the manufacturing error of one or two fringes across the mirror diameter. There are two procedures to be followed to align the etalon. The first procedure balances the capacitance bridges with the etalon in its un-parallel, as-supplied state:

(1) Referring to Fig. 2.40, set the MODE control to BALANCE, the METER DISPLAY switch to OFFSET and the RESPONSE TIME to 0.5ms on the black scale. Turn on the power. The yellow BALANCE indicator will illuminate. The red POWER indicator, mounted in the POWER switch, will also illuminate within about 1 second.

(2) Turn the X COARSE switch to bring the X meter as close to zero as possible. Turning the switch clockwise will move the meter needle from left to right. Take the meter to 0 using the X FINE 10-turn control.

(3) Repeat using the Y and Z controls, observing the Y and Z meters respectively.

(4) Set the METER DISPLAY switch to QUADRATURE ERROR.

(5) Null the X, Y and Z meters using the X, Y and Z QUADRATURE BALANCE 10-turn controls respectively.

(6) Set the METER DISPLAY switch back to OFFSET and re-zero them if necessary using the respective COARSE and FINE controls.

(7) Turn the MODE switch from BALANCE to OPERATE. The yellow BALANCE indicator should go out and the green OPERATE indicator should come on after a delay of about 2 seconds.

(8) Turn the METER DISPLAY switch to QUADRATURE ERROR and null any offset using the relevant QUADRATURE BALANCE controls.

(9) Turn the METER DISPLAY switch back to OFFSET, the meters should all read within about 1V of zero.

The CS100 controller is now controlling the etalon in its as-supplied state. The next procedure is to align the plate parallel. Figure 2.44 shows the set up of the instruments for

aligning the Fabry-Perot. The light source is a suitable spectral lamp or a near-IR laser with beam expander. The receiver is a near-IR camera connected to a video monitor with a video cable. Straight-line fringes should be seen on the screen of the monitor. If the etalon plates (the two front mirror surfaces) are almost parallel, the fringe spacing may be too much for a fringe to be visible. In this case, the Z FINE control could be turned until a fringe appears. When the etalon plates are parallel, the fringe will be expanded to the whole aperture. In order to get the setting values of the meters when the etalon is aligned well, the following steps should be taken:

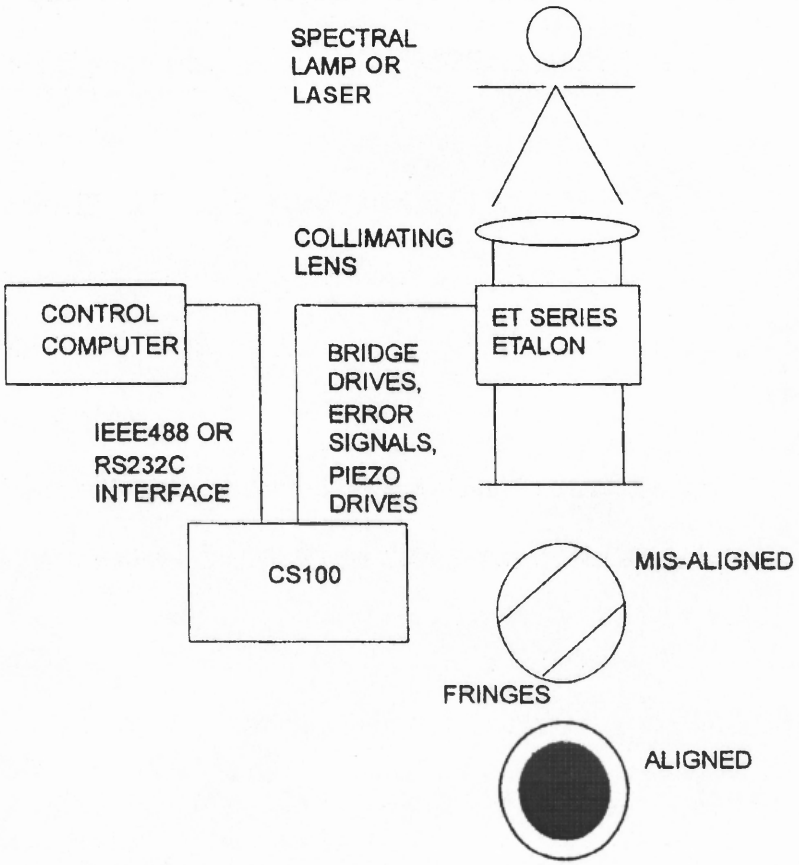

Figure 2.44 Alignment of the Fabry-Perot etalon.

(1) Set the METER DISPLAY switch to QUADRATURE ERROR.

(2) Turn the Z FINE control backwards and forwards. The fringe should be moved backwards and forwards in a direction perpendicular to its length.

(3) Turn the Y COARSE and FINE controls until the movement observed above is predominantly along the Y-axis. While doing this, keep the meters within a couple of volts of zero using the relevant QUADRATURE BALANCE controls. If any meter exceeds about 5 V, the OUT OF RANGE indicator may illuminate and the system reverts to BALANCE mode. If this happens, turn the last turned control back a few positions and set back to OPERATE mode by turning the MODE switch to BALANCE and then back to OPERATE.

(4) Turn the Y COARSE and FINE controls to expand the fringe until it fills as much of the aperture as possible. Again keep the meters within a couple of volts of zero.

(5) Keep adjusting the X and Y FINE controls until turning the Z FINE control causes the field to lighten and darken uniformly.

(6) Null the meters exactly using the QUADRATURE BALANCE controls and verify that the plates are still aligned.

(7) Turn the METER DISPLAY back to OFFSET. Now, the meters will not read zero but will give an indication of how much correction is being applied in the three axes to achieve parallelism at the spacing required to transmit the fringe used for alignment. Usually the X and Y meters will read 0 plus or minus 5V and the Z meter 0 plus or minus 2V.

(8) Record the PARALLELISM and SPACING control settings and QUADRATURE BALANCE settings for future reference.

The etalon plates are now aligned parallel and will remain so while the CS100 is switched on.

After aligning the Fabry-Perot filter, the characteristics, such as transmittance, free spectral range, FWHM, surface flatness, surface roughness, can be measured with a near-IR laser. The testing instruments could be setup as in Fig. 2.45[21-22]. The laser beam is expanded by the pinhole and microscope objective combination and the size of the beam is controlled by the adjustable stop. The beam is collimated through the Fabry-Perots and re-imaged onto a near-IR InGaAs camera having a resolution of 320 by 240 pixels. The Fabry-Perot can be moved into and out of the collimated beam as required. The method for data acquisition consists of stepping the Fabry-Perot across the profile of a collimated laser while taking a series of images of the Fabry-Perot at each Z-step. After parallelism adjustment, two types of images can be obtained:

A. Full-aperture images --- Taking a series of images (a few of ten to hundred) at each Z-step for the full aperture of the Fabry-Perot along with dark images and images of the laser only.

B. Expanded images --- Taking a series of images (a few of ten to hundred) at each Z-step along with dark images and images of the laser only after the image of the Fabry-Perot is optically expanded by a factor of 2.4 to provide enough spatial resolution to investigate the surface roughness of the Fabry-Perot.

With averaging the series of images of A-type image as a point respect to the Z-step, an intensity profile can be obtained with the horizontal axis as Z-spacing. The spacing step, s, between two peaks of the intensity can be obtained from this profile. Eq. 2.55 gives:

$$m = \frac{2n'd\cos\theta}{\lambda_0} \text{ and } m+1 = \frac{2n'(d+s)\cos\theta}{\lambda_0},$$

therefore,

$$s = \frac{d}{m}, \tag{2.63}$$

where, d is the nominal spacing, 2226μm, $n' = 1$ for air, $\theta \approx 0$. On the other hand, the free spectral range, f, is the spectral separation between two peaks of the transmission:

$$f \approx \frac{\lambda_0}{m}. \tag{2.64}$$

The resolution of steps (Å per step) is obtained by f/s. Hence, the profile can be converted to the profile with respect to wavelength (Å). The Full Width of Half Maximum (FWHM) and the free spectral range, f, could be obtained from the wavelength calibrated profile. If the averaging intensity of the laser beam without the Fabry-Perot in the collimated beam is calculated, the transmittance of this Fabry-Perot could be obtained using the value of the profile peak divided by the corresponding laser intensity. With the B-type data, the surface flatness and surface can be estimated by peak-to-valley value for the peak images.

The actual calibration of the Fabry-Perot pass-band should be done on the telescope with the birefringent filter. The values of parameters obtained will be used in future observations.

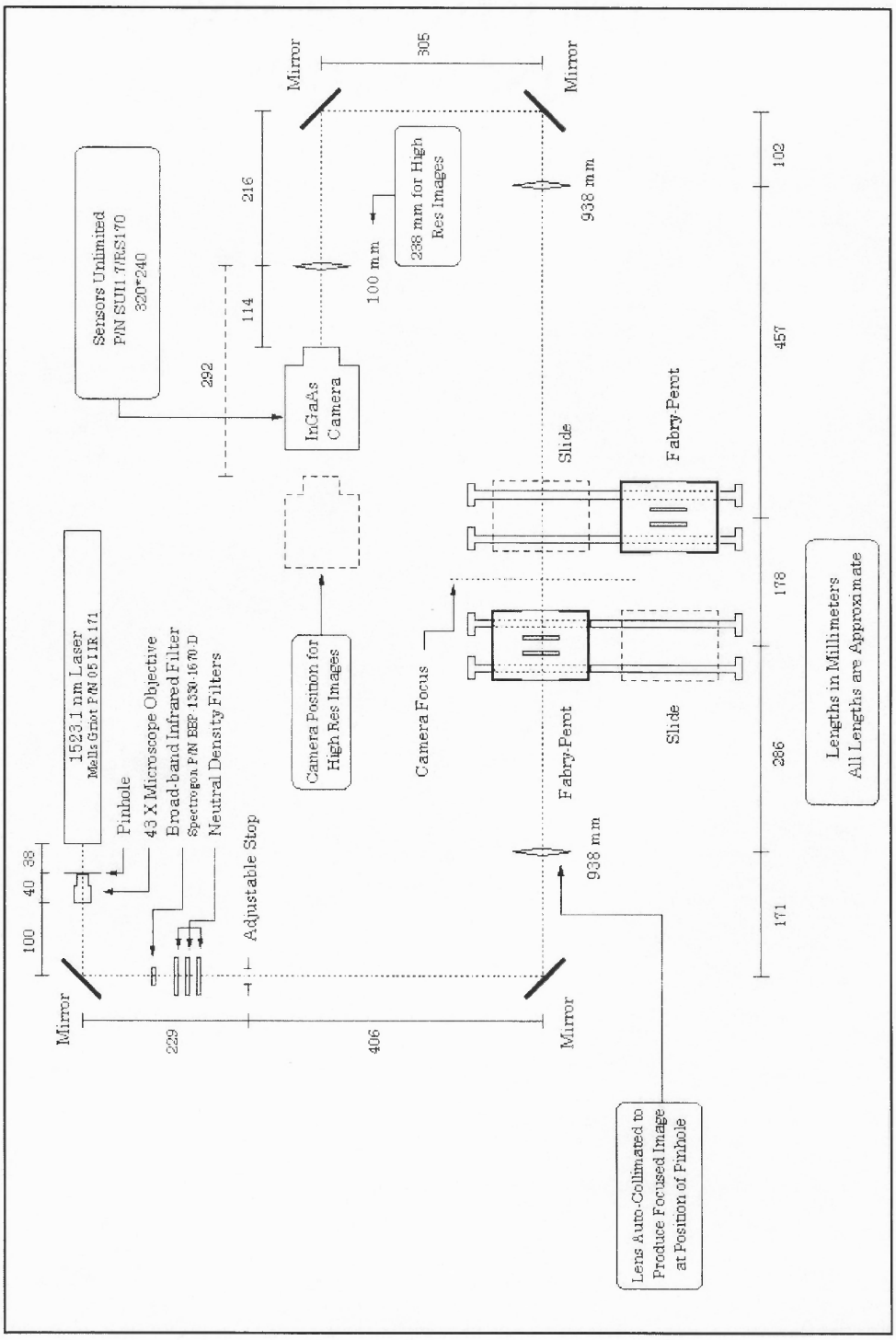

Figure 2.45 Setup of testing the near-IR Fabry-Perot with a laser (Courtesy of Craig Gullixson).

CHAPTER 3

STUDY OF UMBRAL DOTS AT 1.56 μm

3.1 Introduction

The study of structure and evolution of umbrae plays an important role in the understanding the energy transport in sunspots. A simple sunspot usually includes a single umbra and a simple penumbra around the umbra. But, in many sunspots, there are complicated fine structures existing in sunspot umbrae, such as light bridges, umbral dots, light rings, dark nucleus, etc. In a complicated sunspot, multiple umbrae are usually separated by strong light bridges (SLB) and these separated umbrae seem to behave like independent units. These separated dark regions were proposed to be called "umbral cores" (UCs)[40]. The UCs are to be identified with spot fragments and are basic umbral structures which survive the whole lifetime of the sunspot [41]. From a phenomenological point of view, UCs consist of two components:

(1) On the one side, a dark area formed by a diffuse background (DB) with spatially varying intensity and showing well-distinguished local intensity minima that is called dark nuclei (DNs).

(2) The bright features (BFs) within the UCs include umbral dots (UDs), faint light bridges (FLB), and sometimes, light rings.

Figure 3.1 shows an ideal drawing chart of a complicated sunspot. Regarding light bridges, they can be divided into two groups[41]:

(1) Strong light bridges (SLBs), which separate UCs. – They represent an abrupt change in typical umbral conditions and are closely connected with the sunspot decay.

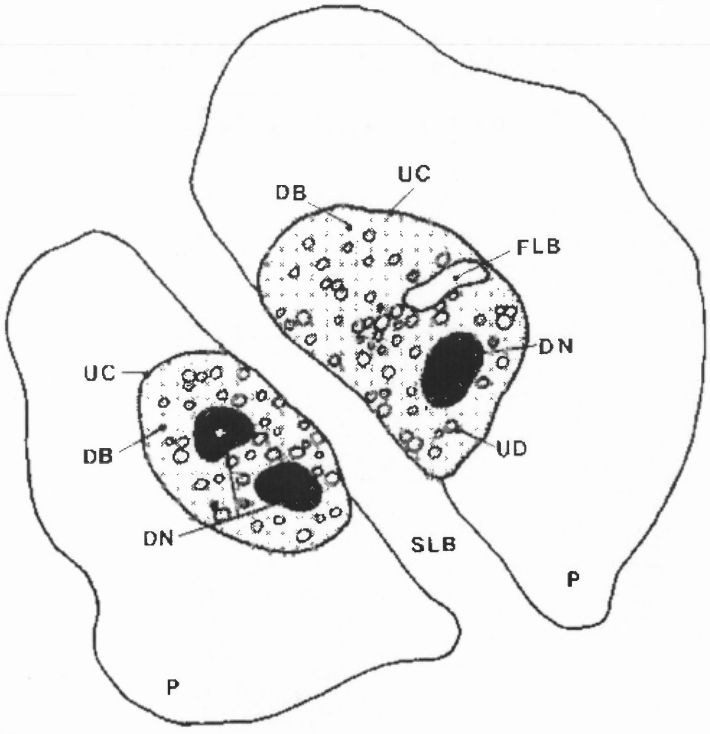

Figure 3.1 An idealized drawing chart of a complicated sunspot. P: penumbra; UC: umbra core; SLB: strong light bridge; DB: diffuse background; DN: dark nucleus; FLB: faint light bridge; UD: umbral dot[41].

(2) Faint light bridges (FLBs), also called streamers, located inside the umbral cores and with widths of about 1 arcsec. – They consist of some rows of bright grains with sizes similar to UDs. Sometimes it is difficult to distinguish FLBs from a chain of UDs. A transition from a chain of UDs to a FLB in the decay phase is a plausible phenomenon.

Umbral dots are very important features of the fine structures in sunspots. UDs are observed as tiny bright features and embedded in the dark area. The study of umbral dots is very important because they carry information on the magnetic structure and the thermal state of the near-surface layer of the umbra. In the literature, two classes of UDs,

"peripheral" umbral dots (PUDs) and "central" umbral dots (CUDs), were often used. But there was no proper definition to distinguish them from each other. There is some confusion as to the definitions:

Definition A. – CUDs are located well inside the umbra and PUDs in the outer parts, where the intensity gradient in the diffuse background is stronger[42]. Moreover, these two classes can be distinguished on the basis of their proper motions, with PUDs moving from the penumbra toward the numbra[43].

Definition B. – CUDs are only those located inside DNs, and those separating DNs are considered as PUDs[40].

These two definitions agree that CUDs are located in the "dark parts of umbrae", but the concept of "dark parts of umbrae" was not defined properly. In general, the CUDs inside DNs are not found in many umbrae. Therefore, it is not needed to distinguish between the central and peripheral umbral dots[41].

From an observational point of view, the most important quantities of umbral dots with respect to the background are intensity contrast, size distribution, magnetic field and flow velocity[44]. The dot intensities are shown in a broad range[42,45], and contribute up to 40% to the umbral intensity at visible wavelengths[46]. Therefore, the intensity of umbral dots represents a source of the observed umbral brightness. The dot intensity is related to the umbral background showing a mean excess of 2.6 above the inter-dot brightness[45]. The size distribution is observed to range between 0.4 ~ 0.7 arcsec[42]. Whereas, in another reference[41], the size of umbral dots is near 0.3 arcsec and is independent on the umbral brightness. The magnetic field strength in dots is about 20%

reduced with respect to the inter-dot field[47]. As for the flow velocity in umbral dots, the observations range from a few km/s to a maximum of 25 m/s[48-49].

In order to explain the physical meaning of umbral dots, a few theoretical models were proposed:

(1) The cluster model -- Umbral dots are believed to be the manifestation for hot columns of gas, rising up between the magnetic ropes. The magnetic field strength in UDs should be greatly reduced at the visible surface and accompanied by substantial up-flows (~10km/s) if the theory of this model is correct[50-51].

(2) The magnetoconvective model -- the sunspot consists of a single monolithic magnetic column. This model theory showed that vertical energy transport is occurring inside the rigid magnetic field structure with a nonlinear treatment of magnetoconvection. In the picture of this model, the UDs are the visible consequence of coherent motions in convective cells with diameters of 250~300km reaching down to a depth of ~1500km. The magnetic field strength would have large fluctuations due to the highly nonlinear oscillations[52].

(3) Model of Degenhardt & Lites[53] -- a field configuration in umbral dots that resembles magnetic 'bottles'. The behavior of a thin vertical gas column embedded in a sunspot umbra was investigated using the thin flux tube approximation[54]. This model predicts only small velocity and magnetic field differences in photospheric layers and an inverse field gradient in UDs.

However, these theoretical model characteristics are not completely in accordance with existing observations. On the other hand, the observations of UDs are strongly

influenced by the spatial resolution of the telescope and seeing conditions. Therefore, it is difficult to rule out or confirm any of the models.

All of the fine structures of umbrae discussed above are probably one of the manifestations of the interplay between convection and magnetism. These manifestations are reflected outside spots in the perturbation of the granulation by plage magnetic fields and, at a large scale, giving place to the dynamo process in deeper layers of convective zone. Because the near-infrared, 1.56μm continuum is formed about 30 km below the base of the quiet photosphere and the solar atmosphere has an opacity minimum near 1.6μm[3], the observations at these spectral region have many advantages on the studies of the fine structures of sunspot umbrae:

- Opacity minimum in solar atmosphere,
- Scattered light is much lower in IR,
- Intrinsic contrast between photosphere and umbra is lower (Planck's radiation law),
- Seeing is much better than in visible light.

In this chapter, the first comprehensive studies of umbral dots at 1.56μm are presented. These observations are the first of umbral dots ever reported at these IR wavelength range. The observation data include two sequences of sunspots, one of which is a complicated sunspot possessing about to 150 umbral dots. The other sunspot is a single, stable spot possessing about to 55 umbral dots and a stable light ring. The data were obtained using the 26-inch telescope of BBSO, with a 50Å wide interference filter at 1.56μm as the central wavelength. The objective is to study the properties of umbral dots in the opacity minimum and lower contrast with diffraction limited images (~ 0.6″).

Because of the lower scatter light in this near-infrared range, the very center of the umbra can be seen clearly. The contrasts, size distribution, and proper motions of umbral dots in these near-infrared data are discussed. Two short movies showing the motions and evolutions of the umbral dots quite clearly will be presented in discussion phase of this dissertation.

3.2 Observations

3.2.1 Instrumentation

The data were acquired on March 12, 1999 and March 17, 1999 respectively, using the 26-inch telescope, BBSO. The instrumental setup has been described by Thomas J. Spirock[55]. This is a newly developed near-infrared system. This system includes an InGaAs camera manufactured by Sensor Unlimited, Ltd, and an interference filter at 15648.5 ± 25Å. This InGaAs camera is 12-bit, 320 by 240 pixels, with image acquisition speed of 30 frames/second. The quantum efficiency of the IR CCD camera is greater than 70% from 1.0 μm to 1.7 μm and the exposure time is 127 μs. This instrument system is actually a sub-system of the near-infrared filter system described in chapter 2. Before the entire filter system is accomplished, the observations with this sub-system are much helpful not only for the studies of sunspot fine structures, but also for testing the near-infrared camera in order to be deployed in the near-infrared filter system. This sub-system is mounted on the 65cm telescope and the spatial solution is about 0.60" at 1.565 μm. The image scale is 0.25"/pix.

3.2.2 Observations

The active regions NOAA 8485 and NOAA 8489 were observed with the 65cm vacuum telescope on March 12 and March 17, 1999, respectively. Two sequences of images of the active region NOAA 8485 and NOAA 8489 were obtained. The images of the sequence of NOAA 8485 are shown in Fig. 3.2 and NOAA 8489 shown in Fig. 3.3.

NOAA 8485 is a very complicated sunspot including many strong light bridges (SLBs), faint light bridges (FLBs) and lots of umbral dots (UDs). From a morphological point of view, it is very difficult to distinguish FLBs from chains of umbral dots or SLBs. The observation of NOAA 8485 consists of a time series of 15 images with 3-minute cadence. NOAA 8489 is a stable sunspot including a "ring" inside the umbral core and about 40 to 50 umbral dots. The observation of NOAA 8489 consists of a time series of 30 images with 2-minute cadence. The seeing on March 12 and March 17, 1999, was moderate to good.

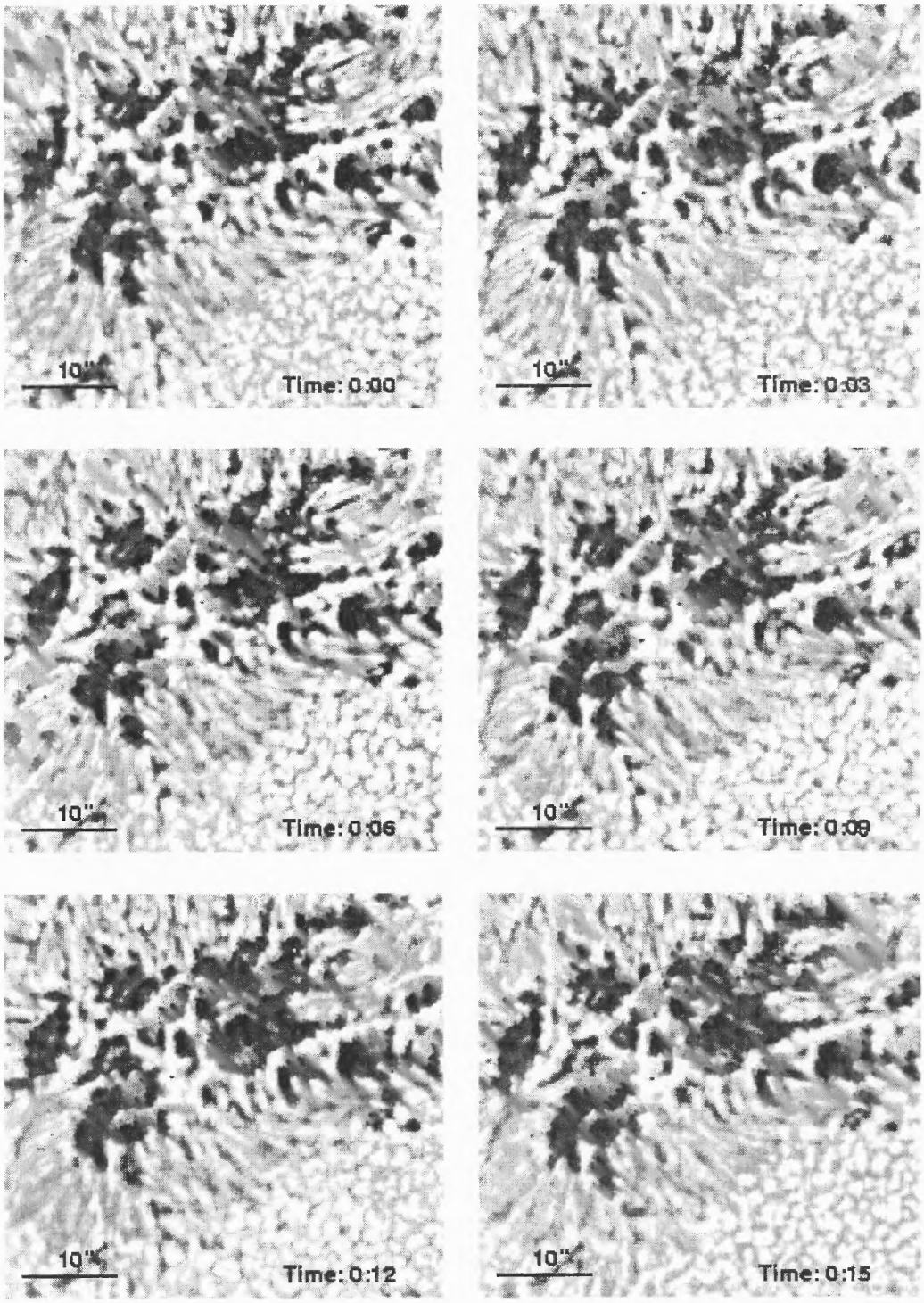

Figure 3.2 Time sequence of NOAA 8485 with 3-minute cadence.

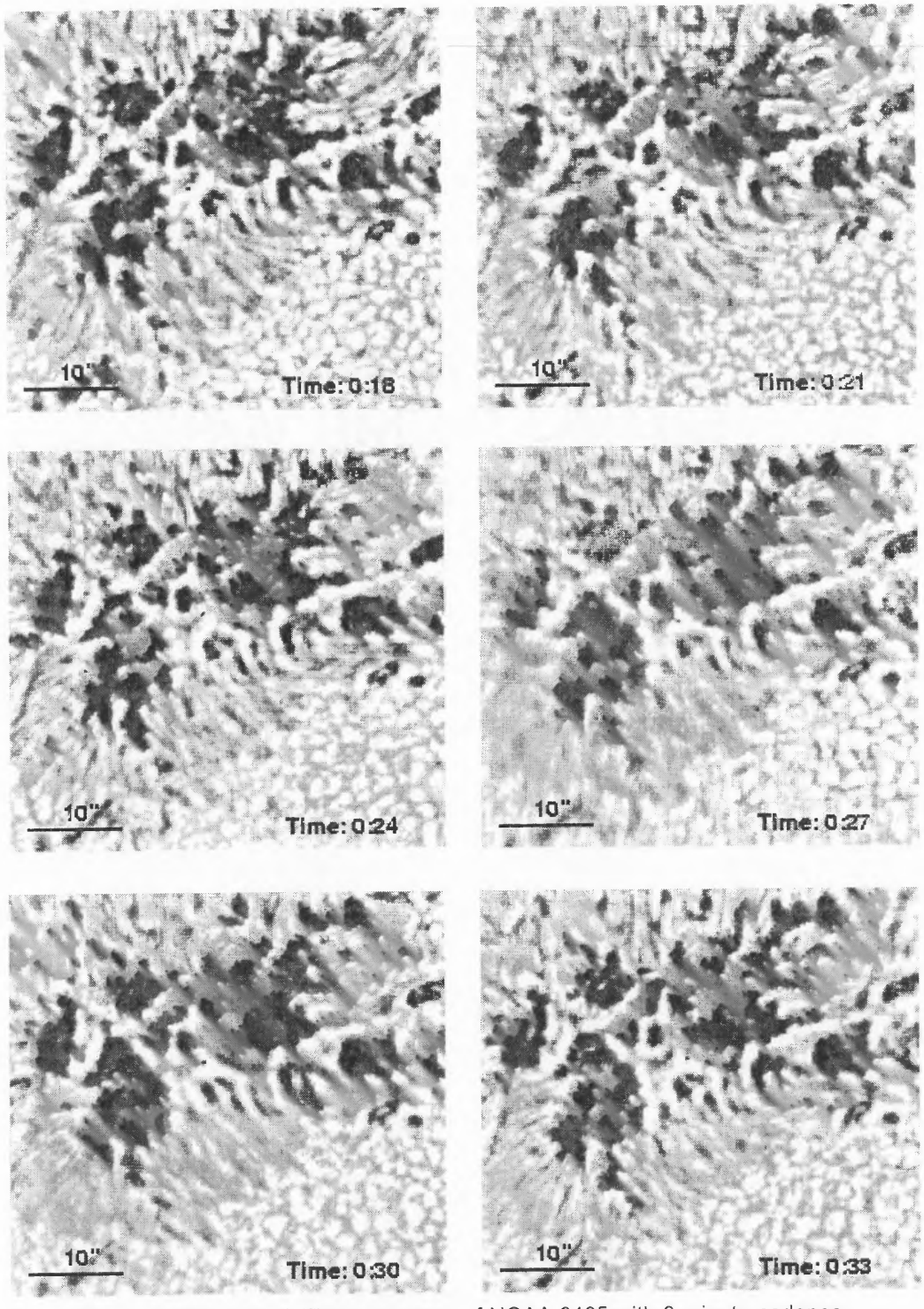

Figure 3.2(Continue) Time sequence of NOAA 8485 with 3-minute cadence.

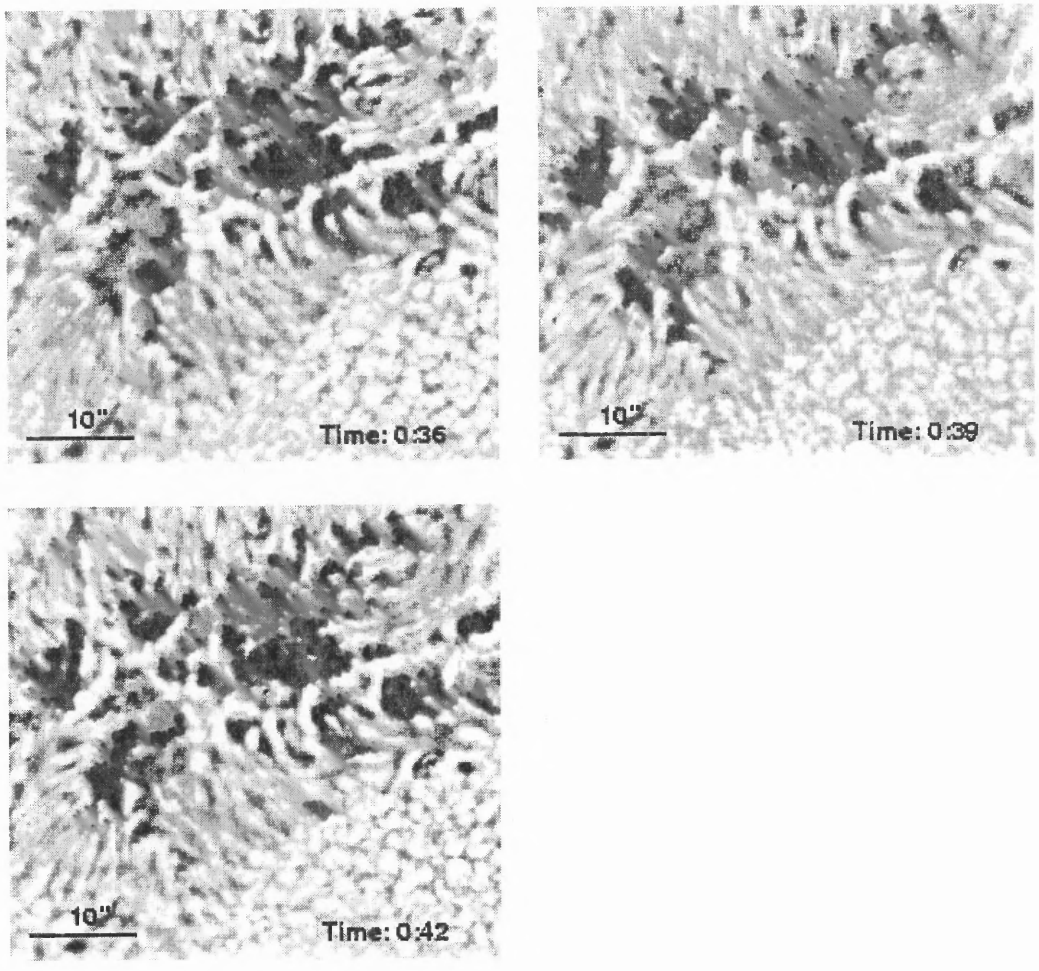

Figure 3.2(Continue) Time sequence of NOAA 8485 with 3-minute cadence.

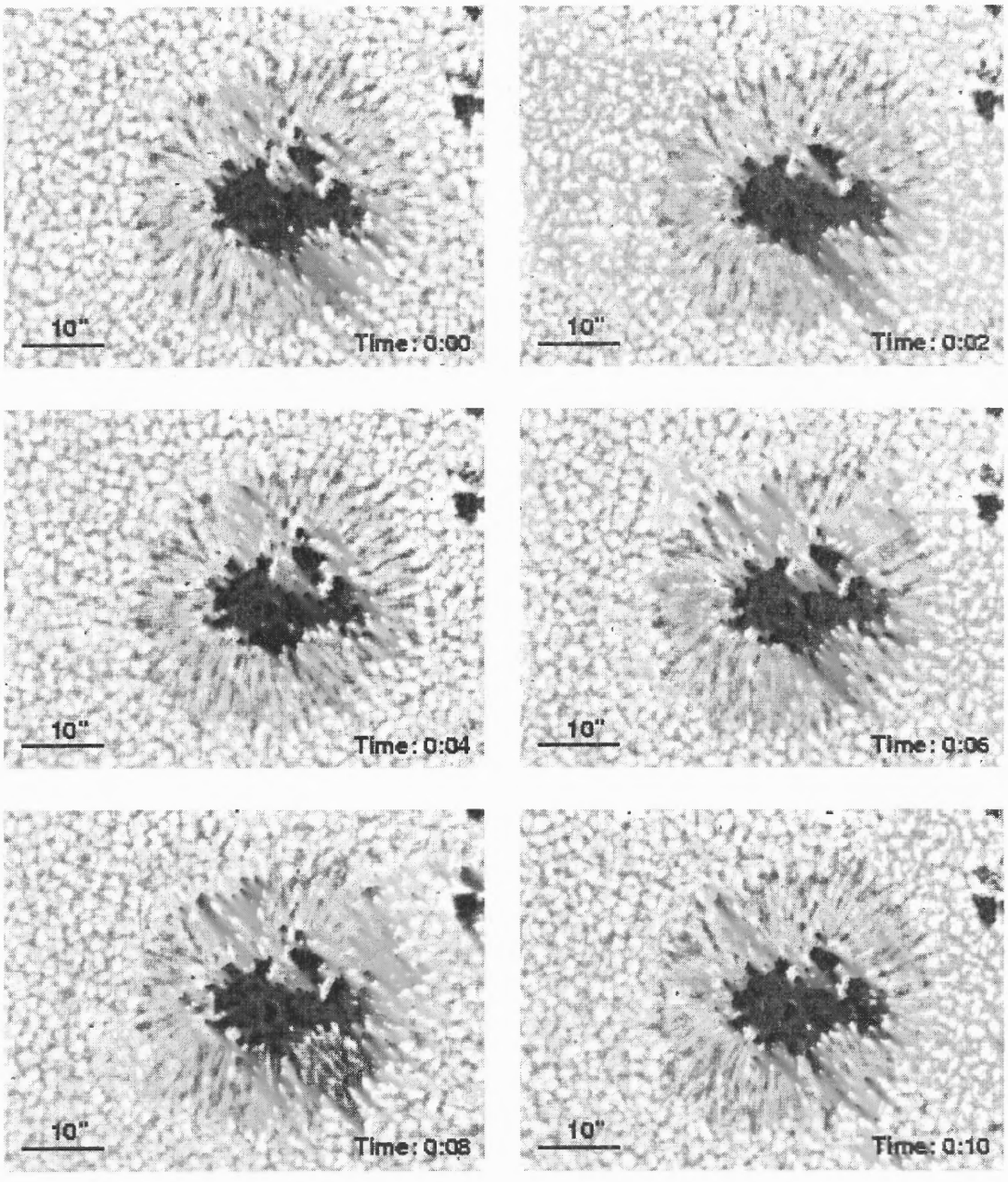

Figure 3.3 Time sequence of NOAA 8489 with 2-minute cadence.

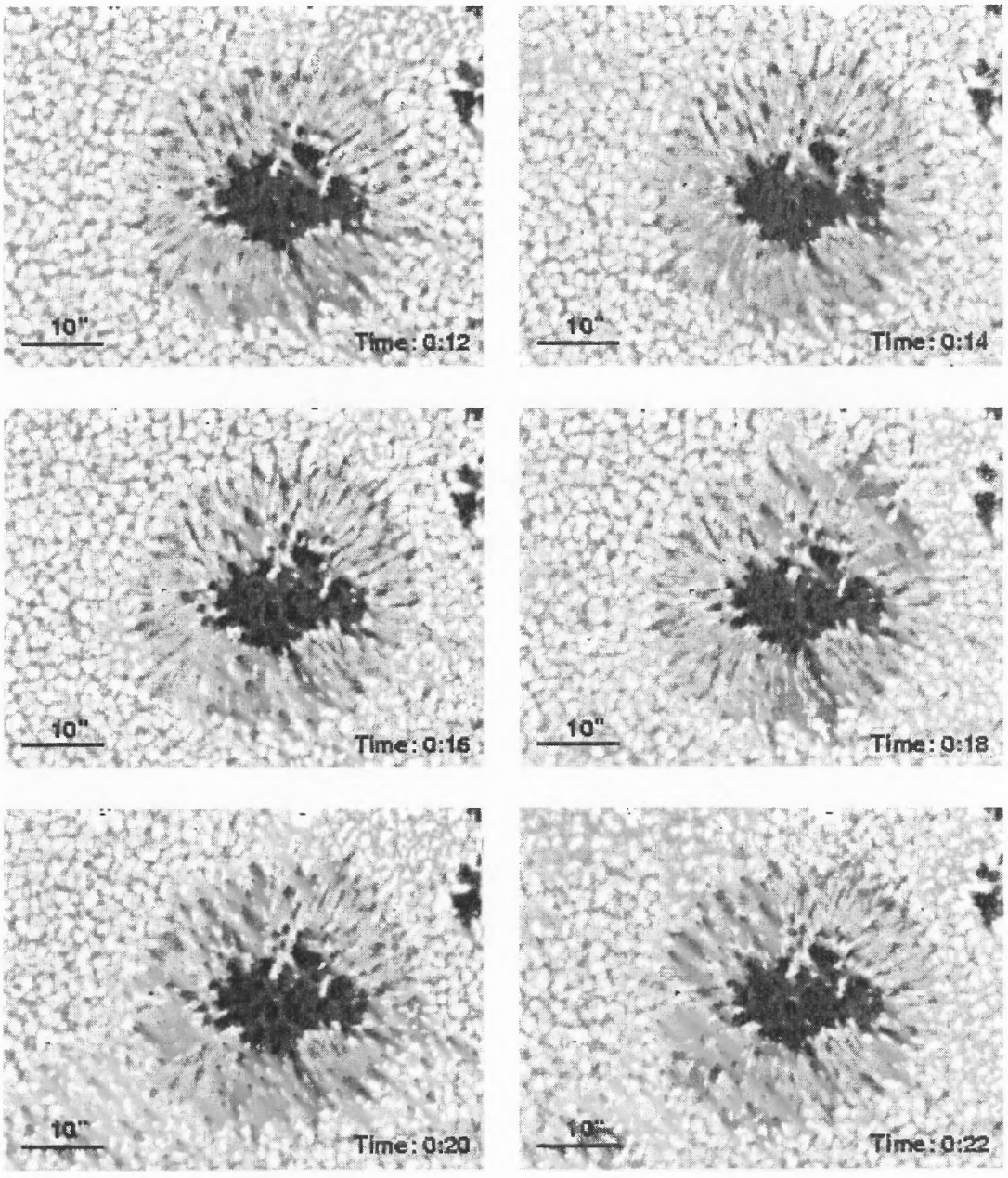

Figure 3.3(Continue) Time sequence of NOAA 8489 with 2-minute cadence.

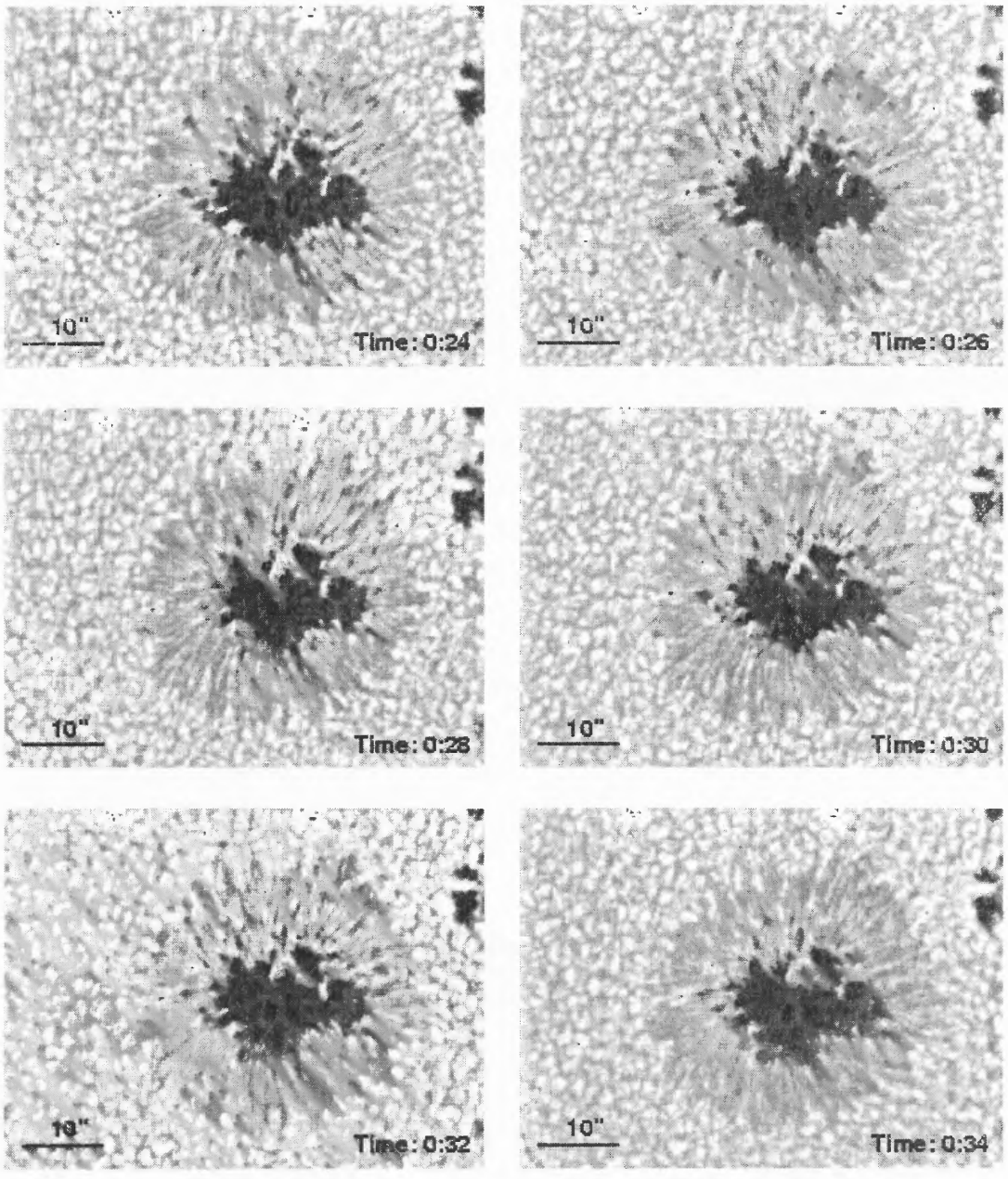

Figure 3.3(Continue) Time sequence of NOAA 8489 with 2-minute cadence.

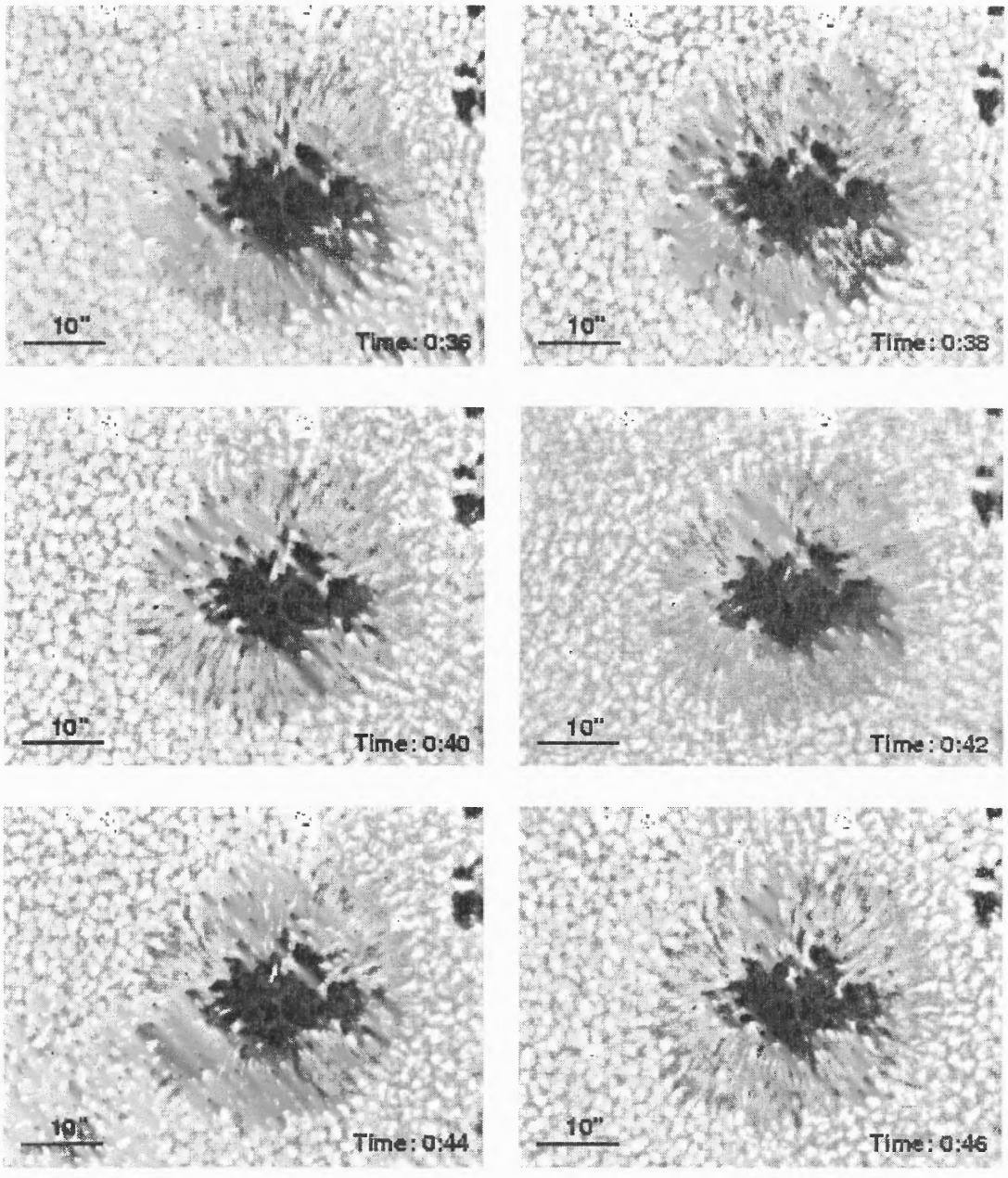

Figure 3.3(Continue) Time sequence of NOAA 8489 with 2-minute cadence.

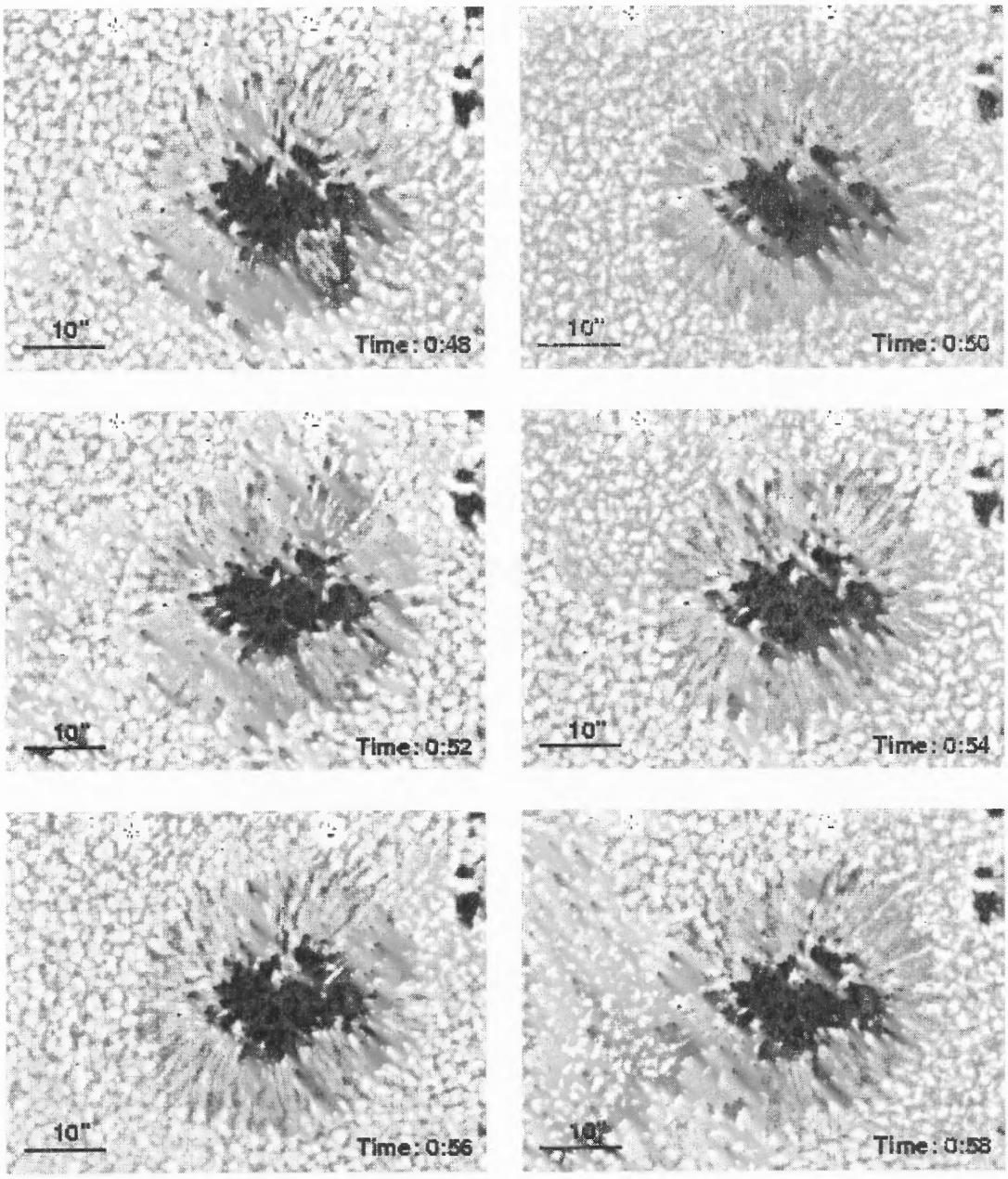

Figure 3.3(Continue) Time sequence of NOAA 8489 with 2-Minute cadence.

3.3 Data Analysis

3.3.1 UD Contrast Distributions

Two best images were chosen from the image series region NOAA 8485 and NOAA 8489 respectively. They were used to calculate the contrast of umbral dots.

Figures 4a & 4b are selected images of active region NOAA 8485 which are enlarged. A few dark nuclear areas are chosen as the background of the umbra and the mean value of this background is about 1369.34 for Fig. 3.4a and 1350.34 for Fig. 3.4b. The photosphere mean value is about 1776.34 for Fig. 3.4a and 1755.03 for Fig.3.4b. Therefore, the intensity ratios between umbra and photosphere are given by:

$$\frac{I_{umbra}}{I_{photosphere}} = \frac{1369.34}{1776.34} = 0.771 \text{ for Fig. 3.4a,} \tag{3.1}$$

$$\frac{I_{umbra}}{I_{photosphere}} = \frac{1350.34}{1776.34} = 0.769 \text{ for Fig. 3.4b.} \tag{3.2}$$

TABLE 3.1 Description of Active Region NOAA 8485

Image	No. of umbral dots	I_{umbra}	$I_{photosphere}$	$I_{umbra} / I_{photosphere}$
Fig.4a	143	1369.34	1776.72	0.771
Fig.4b	150	1350.34	1755.03	0.769

Table 3.1 shows the description of NOAA8485. 143 umbral dots in Fig. 3.4a and 150 umbral dots in Fig. 3.4b were studied. The intensity contrast of umbral dots is given by the maximum intensity value within the umbral dot over its near background. The distributions of umbral dot contrast of NOAA 8485 are shown in Fig. 3.5. From Fig. 3.5, the range of umbral dot contrast is 2% to 20%, and the contrast in most of the umbral dots is in the 10 to 15% range.

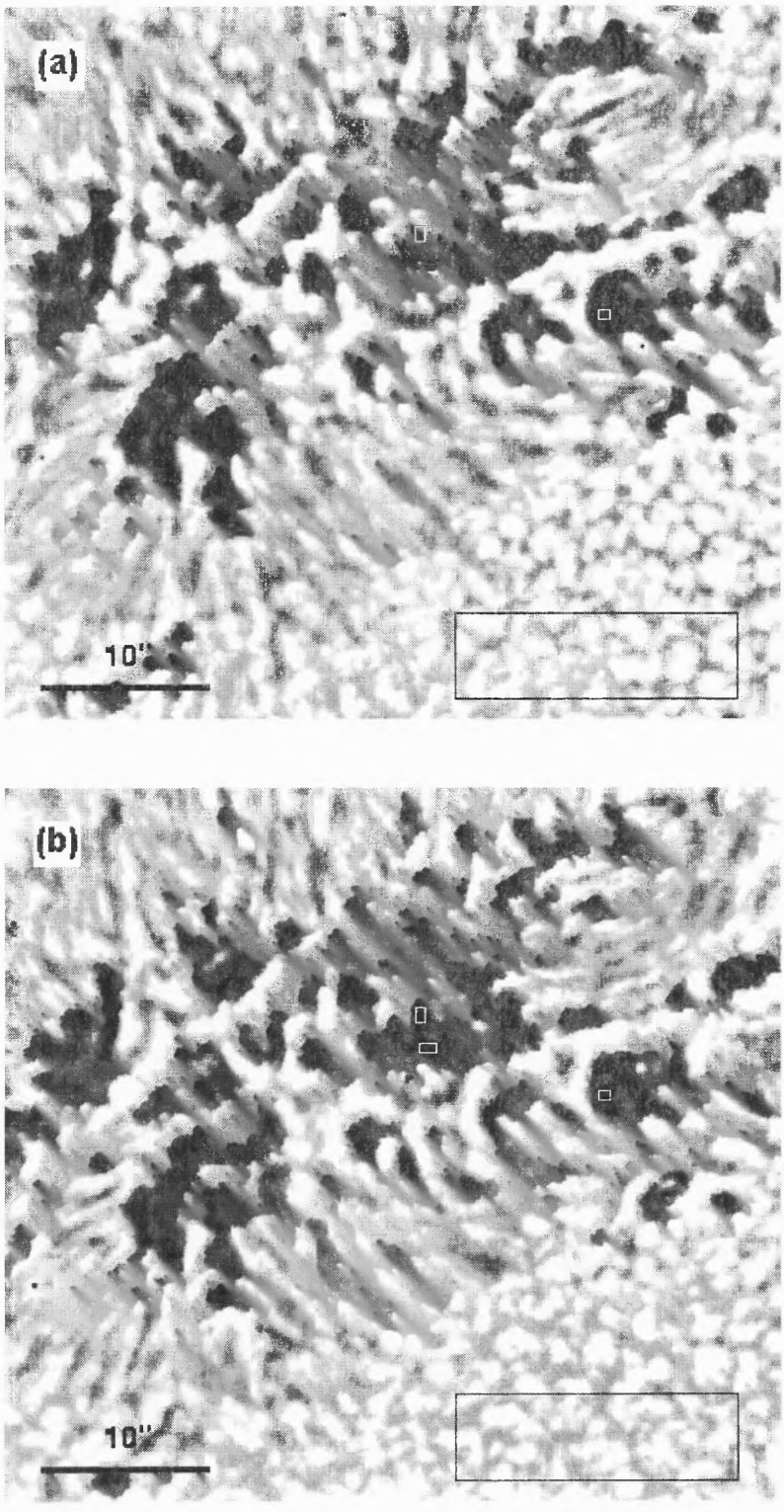

Figure 3.4 The enlarged images of NOAA 8485. (a) Time = 0:0, (b) Time = 0:42.

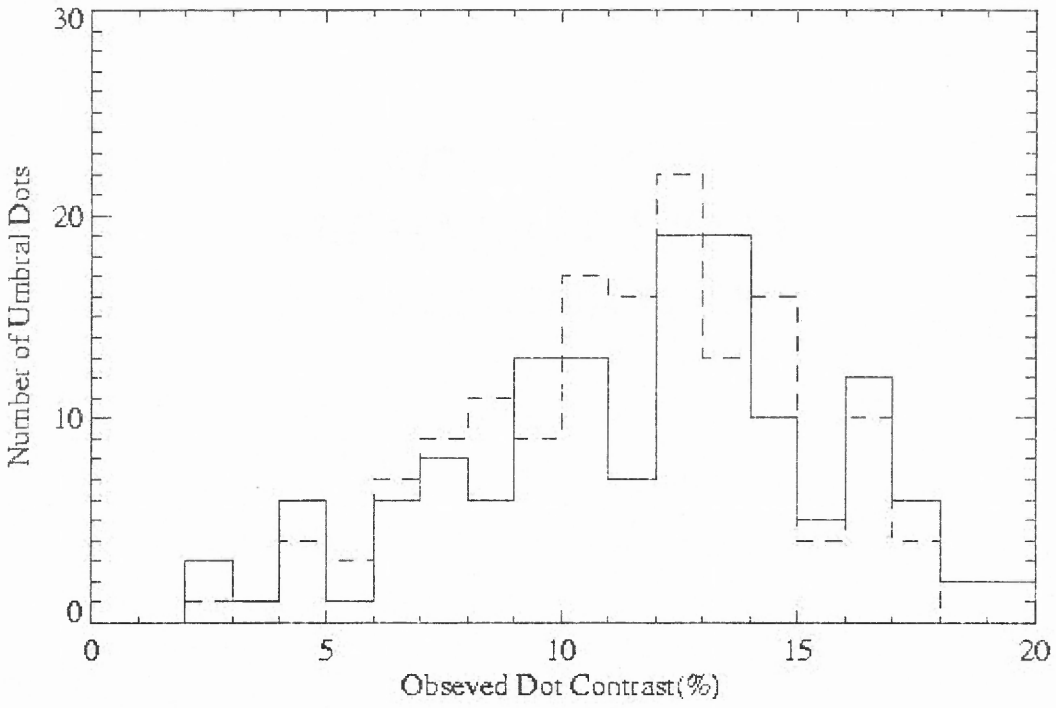

Figure 3.5 The distribution of umbral dot contrast in NOAA 8485. Solid line for Fig. 3.4a, dashed line for Fig. 3.4b.

Figures 3.6a & 3.6b are selected images of active region NOAA 8489 which are enlarged. The mean value of the umbral background is about 1321.60 and the photosphere mean value is about 1858.80 for Fig. 3.6a. In Fig.3.6b, the mean value of the umbral background is about 1322.08 and the photosphere mean value is about 1855.87. Therefore, the intensity ratios between umbra and photosphere are given by:

$$\frac{I_{umbra}}{I_{photosphere}} = \frac{1321.60}{1858.80} = 0.711 \text{ for Fig. 3.6a,} \tag{3.3}$$

$$\frac{I_{umbra}}{I_{photosphere}} = \frac{1322.08}{1855.87} = 0.712 \text{ for Fig. 3.6b.} \tag{3.4}$$

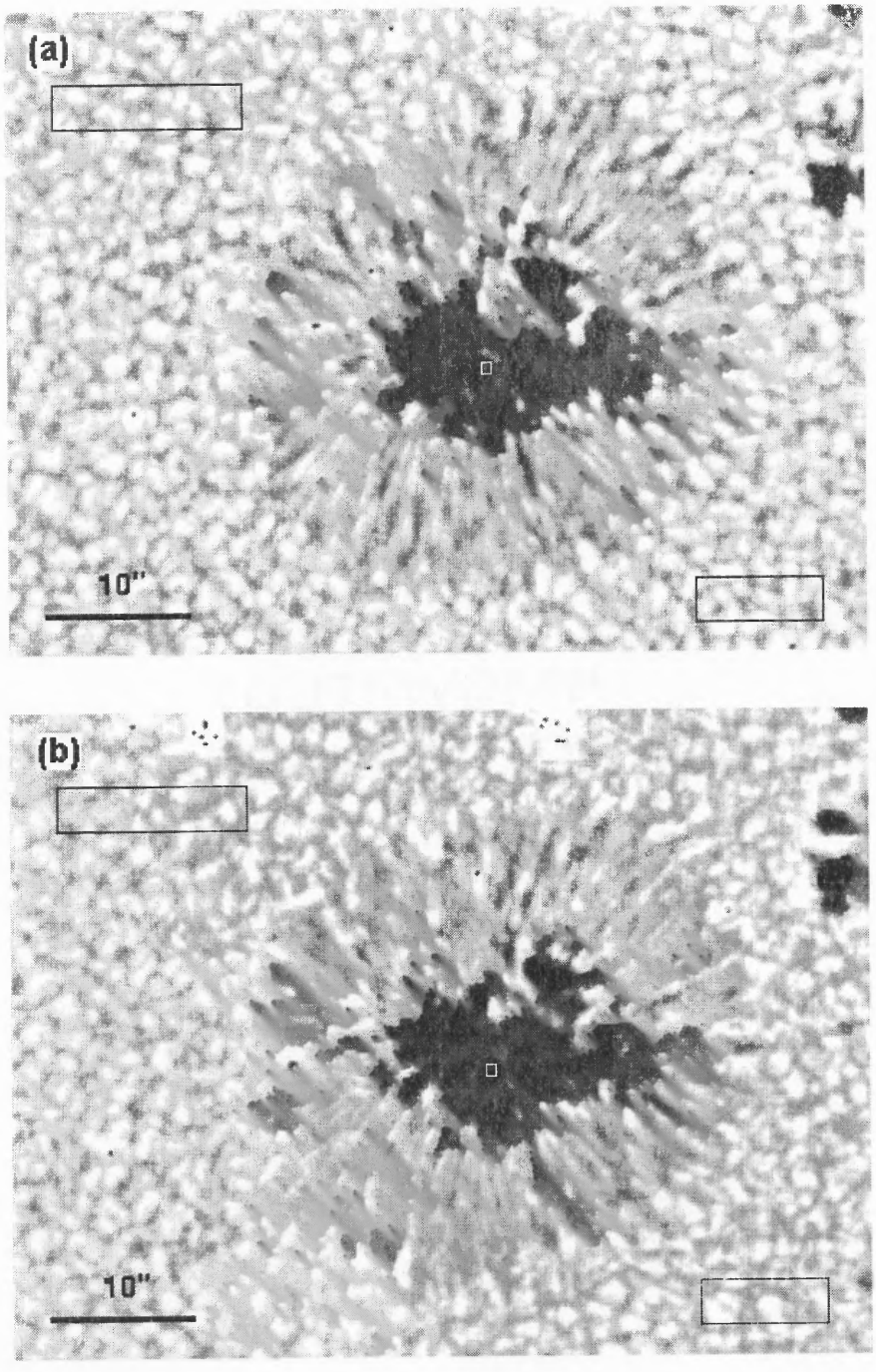

Figure 3.6 The enlarged images of NOAA 8485. (a) Time = 0:0, (b) Time = 0:58.

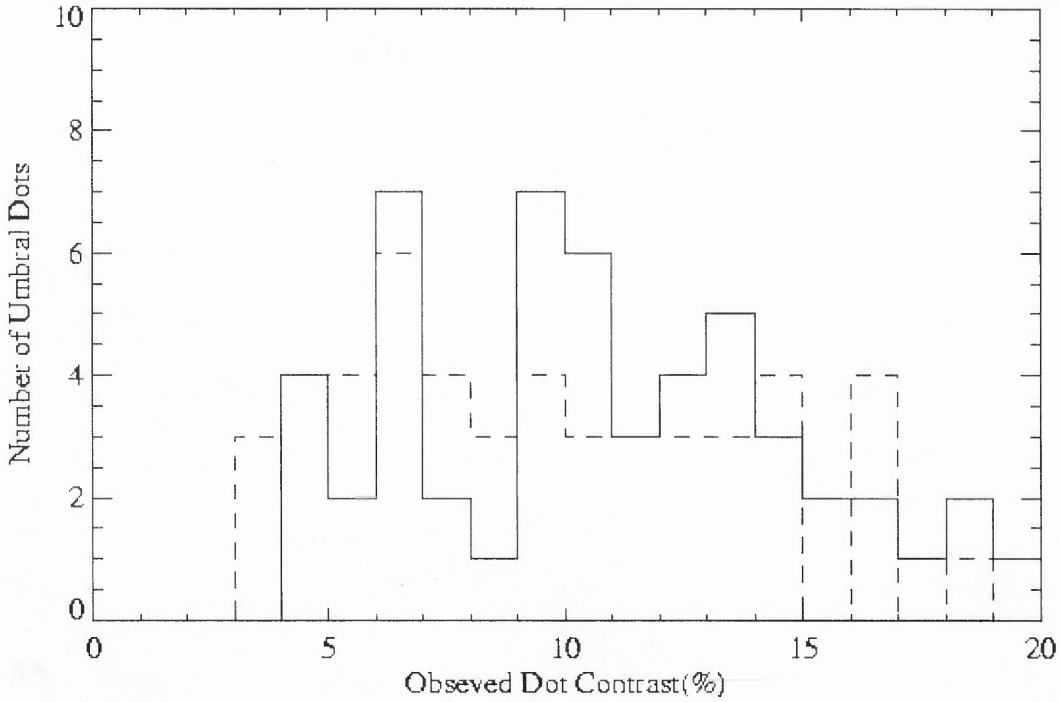

Figure 3.7 The distribution of umbral dot contrast in NOAA 8489. Solid line for Fig. 3.6a, dashed line for Fig. 3.6b.

The description of the active region NOAA 8489 is shown in Table 3.2. This sunspot includes 55 umbral dots in Fig. 3.6a and 50 umbral dots in Fig. 3.6b. The intensity contrast of every dot was calculated by the maximum value within the dot over its near background. Figure 3.7 gives the contrast distribution of the umbral dots in NOAA8489. From Fig. 3.7, it is found that the contrast range is 3% to 20%. The contrast in most of the umbral dots is in the 9 to 15% range.

TABLE 3.2 Description of Active Region NOAA 8489

Image	No. of umbral dots	I_{umbra}	$I_{photosphere}$	$I_{umbra} / I_{photosphere}$
Fig.6a	55	1321.60	1858.80	0.711
Fig.6b	50	1322.08	1855.87	0.712

3.3.2 Size Distributions

The diffraction limit of the 26-inch telescope at BBSO is about 0.60" at this near-infrared wavelength. The image scale is 0.25"/pix. To analyze the size of the umbral dots more precisely, the images were enlarged four times. The size of a dot is found by a geometric average method:

(1) determining its longer and shorter lengths at first,

(2) taking the mean value of these two lengths as the size of the umbral dot.

The size distribution of dot size in NOAA 8485 is shown in Fig. 3.8. From Fig. 3.8, size of umbral dots is 0.3 to 1.0 aresec, but most of the umbral dots has a size of 0.4 to 0.8 arcsec.

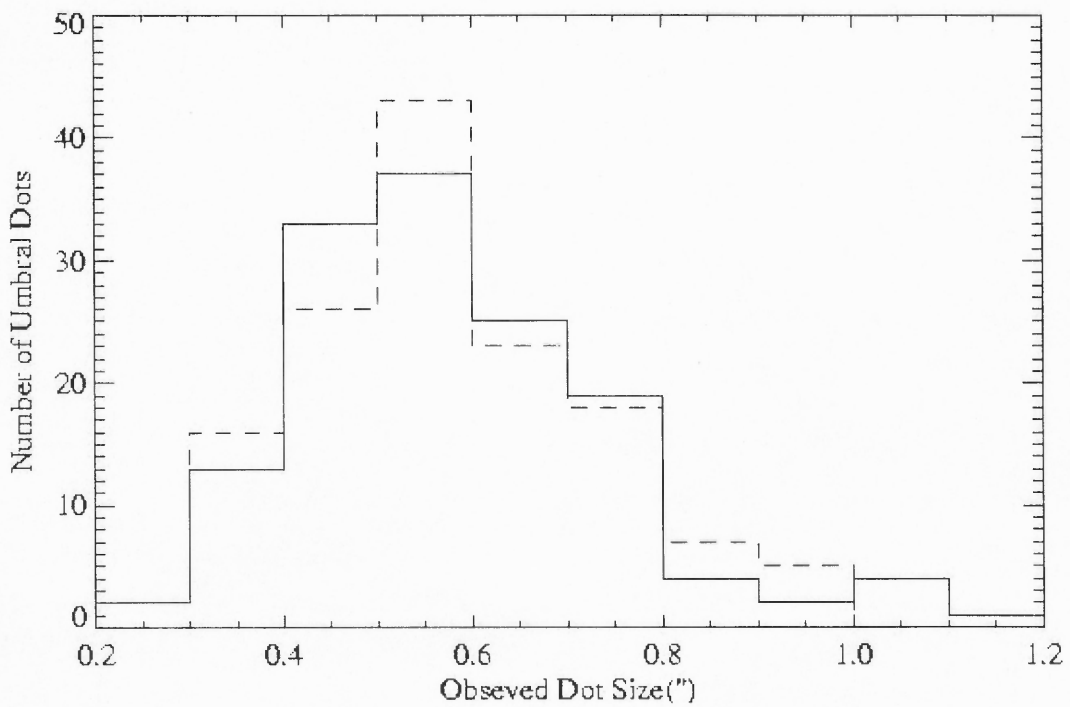

Figure 3.8 The Distribution of umbral dot size in NOAA 8485. Solid line for Fig. 3.4a, dashed line for Fig. 3.4b.

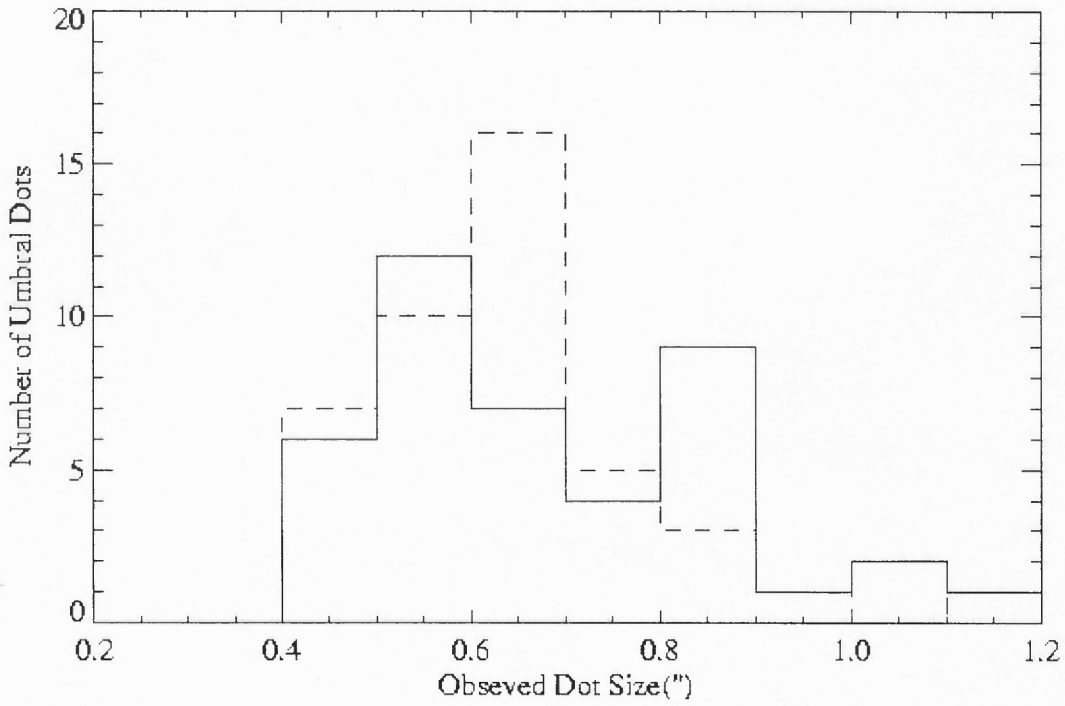

Figure 3.9 The distribution of umbral dot size in NOAA 8489. Solid line for Fig. 3.6a, dashed line for Fig. 3.6b.

Figure 3.9 shows the size distribution of umbral dots in NOAA 8489. Although the range of the size of umbral dots is 0.4 to 1.2 arcsec, the size of most of the umbral dots is in the range of 0.4 to 0.9 arcsec. Therefore, from the studies of the size distributions of NOAA8485 and NOAA 8489, it can be concluded that the size of umbral dots in the near-IR wavelength is 0.4 to 0.8 arcsec. This conclusion is in accordance with the reported value in Ref. 42.

The descriptions of the size distribution of umbral dots show that the most of umbral dots is within 0.4 - 0.8 arcsec, below the diffraction limit of the telescope.

Therefore, larger telescope will be needed to investigate the more fine structures in umbrae of sunspots.

3.3.3 Motion and Lifetime of Umbral Dots

For the motions of the bright grains in penumbra, many authors found that the bright grains, in the sunspot penumbra, move inward toward the umbra[56-61]. From the movies of our near-infrared data, it is obvious that the bright penumbral grains flow into the umbra. These observations support the conclusion above. Under the hypothesis of penumbral convection produced in a comb-like magnetic field structure, the individual flux tubes gain thermal energy and move inward and upward, so that their intersection with the surface migrate radial inward, giving rise to the proper motions of bright penumbral grains[62]. Another explanation for moving umbral bright features is associated with the magnetic fields whose inclination to the vertical is greater than that in the surrounding umbra[63].

In NOAA8489, there is a stable bright "ring" -- a circular light bridge. A chain of umbral dots is a connection between the penumbra and the circular light bridge. The umbral dots coming from the penumbra enter the circular light bridge to become a part of it. On the other side of the circular light bridge, some umbral dots leave from the circular light bridge. Therefore, it can be concluded that (1) umbral dots may become a part of strong light bridge, (2) a strong light bridge may eject umbral dots into umbra.

As for the lifetime of the umbral dots, they all survive for the entire observing duration time, i. e., about an hour. Therefore, from these observations, the lifetime of umbral dots should be much longer than 1 hour.

CHAPTER 4

CONCLUSIONS AND RECOMMENDATIONS

In this dissertation, a near-infrared birefringent filter system (actually a magnetograph), used for observations of solar monochromatic images and measurements of the solar magnetic fields at FeI15648.5Å and FeI15652.9Å at BBSO, has been described in detail (Chapter 2). This system includes a few optical parts -- a prefilter, a magnetic analyzer, a near-infrared birefringent filter, near-infrared Fabry-Perot filter and an IR camera. The optical design and fabrication of the near-infrared birefringent filter is the most important task in this system. For its optical design, the birefringent index of calcite near 1565nm has been measured (section 2.2.1). The values of the birefringent index, μ, of calcite have been obtained:

$$\mu\ (\lambda = 15648.5\ \text{Å}, T = 21°C) = n\lambda/d\ (21°C) \approx -0.1772989,$$

$$\mu\ (\lambda = 15648.5\ \text{Å}, T = 43°C) = n\lambda/d\ (43°C) \approx -0.1770494.$$

The temperature coefficients of μ are also measured (section 2.2.1.3). Its average value is:

$$\alpha \approx -5.37 \times 10^{-5}/°C.$$

In addition, the birefringent indices of calcite within a wide spectral range (from 1000nm to 1650nm) are also measured (section 2.2.2). These measured results are important in physical optics and optical components for communications because the working window of fiber communications is between 1300nm to 1600nm. These measured results are very different from that in the literature[33-34] and have been shown to be reliable.

The polished calcite plates and near-infrared half waveplates have been tested on the spectrograph at BBSO. The analysis of the results shows that the components have good qualities for construction of the near-IR birefringent filter as a key part of the entire system.

The basics of the Fabry-Perot filter used in this near-IR filter system have been described (section 2.41). The surface qualities of the etalon mirrors are very important because the near-infrared Fabry-Perot filter is used in this magnetograph in the imaging mode. Considerations for the surface quality testing of this near-IR Fabry-Perot filter have been discussed (section 2.4.2).

Two sequences of sunspot fine structure have been observed at 1.56μm. The data analyses show the following conclusions:

1. Contrast range of umbral dots is 3% to 20% with peaks at 9% to 15%.
2. Size range of dots is about 0.4 to 0.8 arsec with a peak around 0.5 arcsec probably due to diffraction limit.
3. Lifetime of most umbral dots is longer than 1 hour, the duration of observations.
4. No proper motion was observed for umbral dots, except near the penumbra where dots move towards umbra.
5. Umbral dots may become a part of strong light-bridge and a strong light bridge may eject umbral dots into umbra.

APPENDIX A

DERIVATION OF TRANSMITTANCE OF A ROTATED COMPONENT WAVELENGTH-TUNABLE ELEMENT

In this appendix, we derive Eqs. 2.13 and 2.14. Figure A.1 is a scheme of a rotating polarizer element and Figure A.2 shows the direction of each component. Let a light beam passing the first polarizer P_1 and the amplitude of the vibration be:

$$\text{after } P_1 : a = \cos(\omega t). \tag{A.1}$$

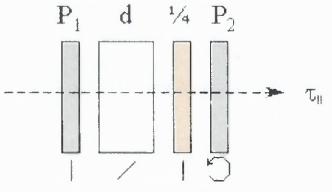

Figure A.1 A rotating polarizer element.

Its direction is along P_1 in Fig. A.2. Inside the birefringent crystal d, the beam could be split into two beams, one is faster (f_d) and another is slower (s_d). The phase difference is $\delta = 2\pi\mu d/\lambda$.

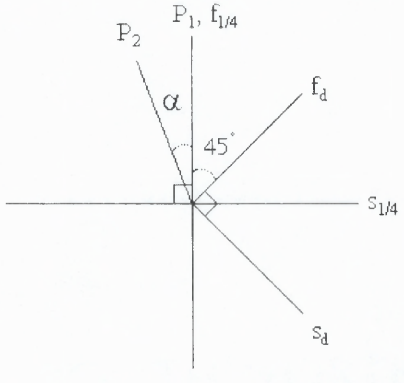

Figure A.2 The axes of all the components.

After passing d:

$$f_d = \frac{1}{\sqrt{2}}\cos(\omega t + \delta) \tag{A.2}$$

$$s_d = -\frac{1}{\sqrt{2}}\cos(\omega t). \tag{A.3}$$

Passing the quarter waveplate (with a $\pi/2$ phase difference):

$$f_{1/4} = \frac{1}{\sqrt{2}}\left[\frac{1}{\sqrt{2}}\cos(\omega t + \delta + \frac{\pi}{2})\right]$$

$$-\frac{1}{\sqrt{2}}\left[-\frac{1}{\sqrt{2}}\cos(\omega t + \frac{\pi}{2})\right]$$

$$= -\frac{1}{2}[\sin(\omega t + \delta) + \sin \omega t] \tag{A.4}$$

$$s_{1/4} = \frac{1}{\sqrt{2}} f_d + \frac{1}{\sqrt{2}} s_d = \frac{1}{2}[\cos(\omega t + \delta) - \cos \omega t]. \tag{A.5}$$

The amplitude of the light passing through the second polarizer, P_2 will be:

$$P_2 = f_{1/4} \sin \alpha - s_{1/4} \cos \alpha$$

$$= -\frac{1}{2}[\sin(\omega t + \delta) + \sin \omega t]\cos \alpha - \frac{1}{2}[\cos(\omega t + \delta) - \cos \omega t]\sin \alpha$$

$$= \frac{1}{2}\{[-\sin(\omega t + \delta)\cos \alpha - \cos(\omega t + \delta)\sin \alpha] - [\sin \omega t \cos \alpha - \cos \omega t \sin \alpha]\}$$

$$= \frac{1}{2}\{-\sin(\omega t + \delta + \alpha) - \sin(\omega t - \alpha)]\}$$

$$= \frac{1}{2}\cdot\left[-2\sin(\omega t + \frac{\delta}{2})\cos(\frac{\delta}{2} + \alpha)\right]$$

$$= -\cos(\frac{\delta}{2} + \alpha)\sin(\omega t + \frac{\delta}{2}) \tag{A.6}$$

The transmittance exiting from the second polarizer P_2 is:

$$\tau_{\parallel} = \cos^2(\frac{\delta}{2} + \alpha) = \cos^2(\pi\mu t / \lambda + \alpha) = \cos^2(\sigma\pi + \alpha). \quad (A.7)$$

This is Eq. 2.13.

For the rotating half waveplate element, Fig. A.3 is a scheme of a rotating half waveplate element and Fig. A.4 shows the directions of the components. The amplitudes before the rotated half waveplate are same as in Eq. A.5 and Eq. A.6.

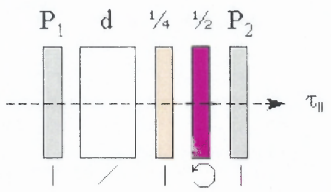

Fig A.3 A rotating half wavelength element.

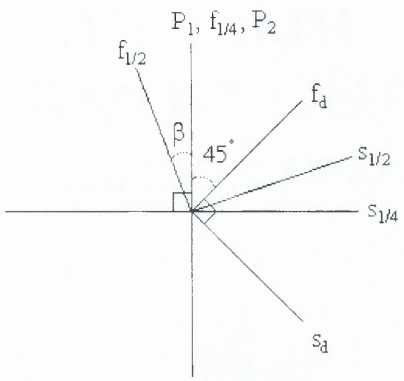

Figure A.4 The axes of all the components.

After passing through the rotated half waveplate, the amplitudes will be:

$$f_{1/2} = -\frac{1}{2}[\sin(\omega t + \delta + \pi) + \sin(\omega t + \pi)]\cos\beta - \frac{1}{2}[\cos(\omega t + \delta + \pi) - \cos(\omega t + \pi)]\sin\beta$$

$$= \frac{1}{2}[\sin(\omega t + \delta + \beta) + \sin(\omega t - \beta)], \qquad \text{(A.8)}$$

$$s_{1/2} = f_{1/4}\sin\beta + s_{1/4}\cos\beta$$

$$= -\frac{1}{2}[\sin(\omega t + \delta) + \sin\omega t]\sin\beta + \frac{1}{2}[\cos(\omega t + \delta) - \cos\omega t]\cos\beta$$

$$= \frac{1}{2}[\cos(\omega t + \delta + \beta) - \cos(\omega t - \beta)]. \qquad \text{(A.9)}$$

Passing the second polarizer P_2, the amplitudes will be:

$$P_2 = f_{1/2}\cos\beta + s_{1/2}\sin\beta$$

$$= \frac{1}{2}[\sin(\omega t + \delta + \beta) + \sin(\omega t - \beta)]\cos\beta + \frac{1}{2}[\cos(\omega t + \delta + \beta) - \cos(\omega t - \beta)]\sin\beta$$

$$= \frac{1}{2}[\sin(\omega t + \delta + 2\beta) + \sin(\omega t - 2\beta)]$$

$$= \cos(\frac{\delta}{2} + 2\beta)\sin(\omega t + \frac{\delta}{2} + 2\beta). \qquad \text{(A.10)}$$

The transmittance exiting from the second polarizer P_2 is

$$\tau_{\parallel} = \cos^2(\frac{\delta}{2} + 2\beta) = \cos^2(\pi\mu d/\lambda + 2\beta) = \cos^2(\sigma\pi + 2\beta). \qquad \text{(A.11)}$$

This is Eq. 2.14.

APPENDIX B

CALCULATIONS OF SYSTEMATIC ERRORS DUE TO THE AXES OF OPTICAL COMPONENTS

In this appendix, the transmittance deviation due to the axes of polarizers and calcite plates are considered. Figure B.1 is a scheme of an element of a birefringent filter.

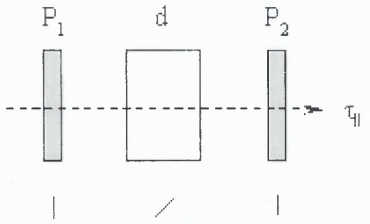

Figure B.1 A rotating half waveplate element.

Let P_1 be at 90°, the birefringent crystal d at 45° +Δα and P_2 at 90° +Δβ. Let a light beam passing the first polarizer P_1, and the amplitude of vibration be:

after P_1 : $a = \cos(\omega t)$. (B.1)

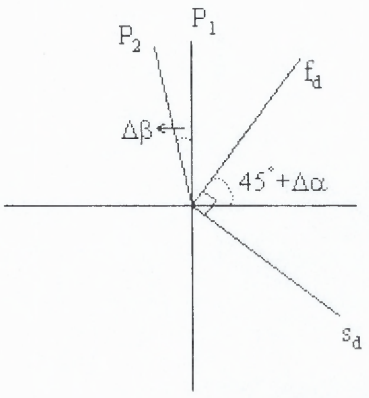

Figure B.2 Axes of all the components.

Its direction is along P_1 in Fig. B.2. Inside the birefringent crystal d, the beam could be split into two beams, one is faster (f_d) and the other is slower (s_d). The phase difference is $\delta=2\pi\mu d/\lambda$. After passing d:

$$f_d = \cos(45^o - \Delta\alpha)\cos(\omega t + \delta) \tag{B.2}$$

$$s_d = -\cos(45^o + \Delta\alpha)\cos(\omega t). \tag{B.3}$$

The amplitude of the light passing through the second polarizer, P_2, will be:

$$\begin{aligned}
P_2 &= f_d \sin(45^o + \Delta\alpha - \Delta\beta) - s_d \cos(45^o + \Delta\alpha - \Delta\beta) \\
&= \cos(45^o - \Delta\alpha + \Delta\beta)\cos(45^o - \Delta\alpha)\cos(\omega t + \delta) \\
&\quad + \cos(45^o + \Delta\alpha - \Delta\beta)\cos(45^o + \Delta\alpha)\cos\omega t \\
&= \frac{1}{2}\left[\cos(90^o - 2\Delta\alpha + \Delta\beta) + \cos(\Delta\beta)\right]\cos(\omega t + \delta) \\
&\quad + \frac{1}{2}\left[\cos(90^o + 2\Delta\alpha - \Delta\beta) + \cos(\Delta\beta)\right]\cos\omega t \\
&= \frac{1}{2}\{\cos(\Delta\beta)[\cos(\omega t + \delta) + \cos\omega t] + \sin(2\Delta\alpha - \Delta\beta)[\cos(\omega t + \delta) - \cos\omega t]\} \\
&= \cos(\Delta\beta)\cos(\frac{\delta}{2})\cos(\omega t + \frac{\delta}{2}) - \sin(2\Delta\alpha - \Delta\beta)\sin(\frac{\delta}{2})\sin(\omega t + \frac{\delta}{2}) \\
&= \sqrt{\cos^2(\Delta\beta)\cos^2(\frac{\delta}{2}) + \sin^2(2\Delta\alpha - \Delta\beta)\sin^2(\frac{\delta}{2})}\cos(\omega t + \frac{\delta}{2} + \Phi).
\end{aligned} \tag{B.4}$$

where $\cos\Phi = \dfrac{\cos(\Delta\beta)\sin(\frac{\delta}{2})}{\sqrt{\cos^2(\Delta\beta)\sin^2(\frac{\delta}{2}) + \sin^2(2\Delta\alpha - \Delta\beta)\cos^2(\frac{\delta}{2})}}$

$$\sin\Phi = \frac{\sin(2\Delta\alpha - \Delta\beta)\cos(\frac{\delta}{2})}{\sqrt{\cos^2(\Delta\beta)\sin^2(\frac{\delta}{2}) + \sin^2(2\Delta\alpha - \Delta\beta)\cos^2(\frac{\delta}{2})}}$$

The transmittance existing from the second polarizer P_2 is:

$$\tau_{\parallel} = \cos^2(\Delta\beta)\cos^2(\frac{\delta}{2}) + \sin^2(2\Delta\alpha - \Delta\beta)\sin^2(\frac{\delta}{2}). \quad \text{(B.5)}$$

This is a general formula of the transmittance for one element with arbitrary directions of birefringent crystal and the second polarizer. There are a few cases discussed below.

(1) If $\Delta\alpha = 0$, $\Delta\beta = 0$, Eq. B.5 gives,

$\tau_{\parallel} = \cos^2(\frac{\delta}{2})$. This is just the normal formula of transmittance of an element.

(2) If $\Delta\alpha = 0$, $\Delta\beta \neq 0$, we have:

$$\tau_{\parallel} = \cos^2(\frac{\delta}{2})\cos^2(\Delta\beta) + \sin^2(\Delta\beta)\sin^2(\frac{\delta}{2}). \quad \text{(B.6)}$$

The modeling of $\tau_{\parallel}$ in Eq. B.6 is shown in Fig. B.3. We can conclude from Fig. B.3 that (a) although values of maximum and minimum are changed, their positions of wavelength are not changed; (b) FWHM is not changed.

(3) If $\Delta\alpha \neq 0$, $\Delta\beta = 0$, we have

$$\tau_{\parallel} = \cos^2(\frac{\delta}{2}) + \sin^2(2\Delta\alpha)\sin^2(\frac{\delta}{2}). \quad \text{(B.7)}$$

The modeling of $\tau_{\parallel}$ in Eq. B.7 is shown in Fig. B.4. We can conclude from Fig. B.4 that (a) although value of minimum is changed, the positions of wavelength of the peaks (maximum values) are not changed; (b) FWHM is changed.

The error analyses of transmittance due to the axis errors of polarizer and crystal indicate that there are no changes in wavelength positions of the maximum value even if there are some errors on the optical axis of birefringent crystal and polarization direction of the polarizers. It is very important for measurement of the birefringent index of calcite because, in principle, measuring the wavelength positions of the peaks is critical.

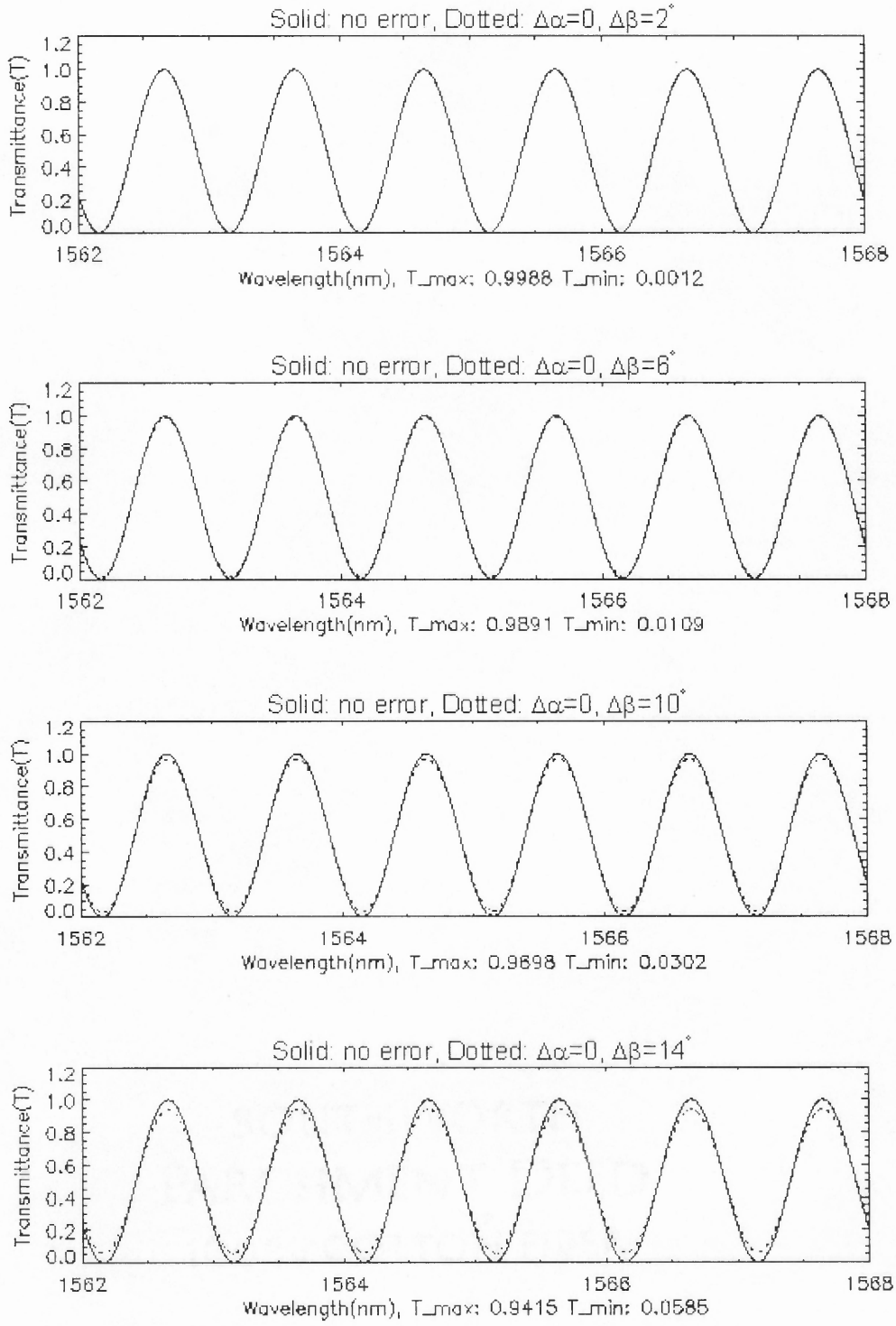

Figure B.3 Numerical modeling of transmittance of an element with $\Delta\alpha = 0$, $\Delta\beta \neq 0$. Solid line: no error, dashed line: error with $\Delta\beta$.

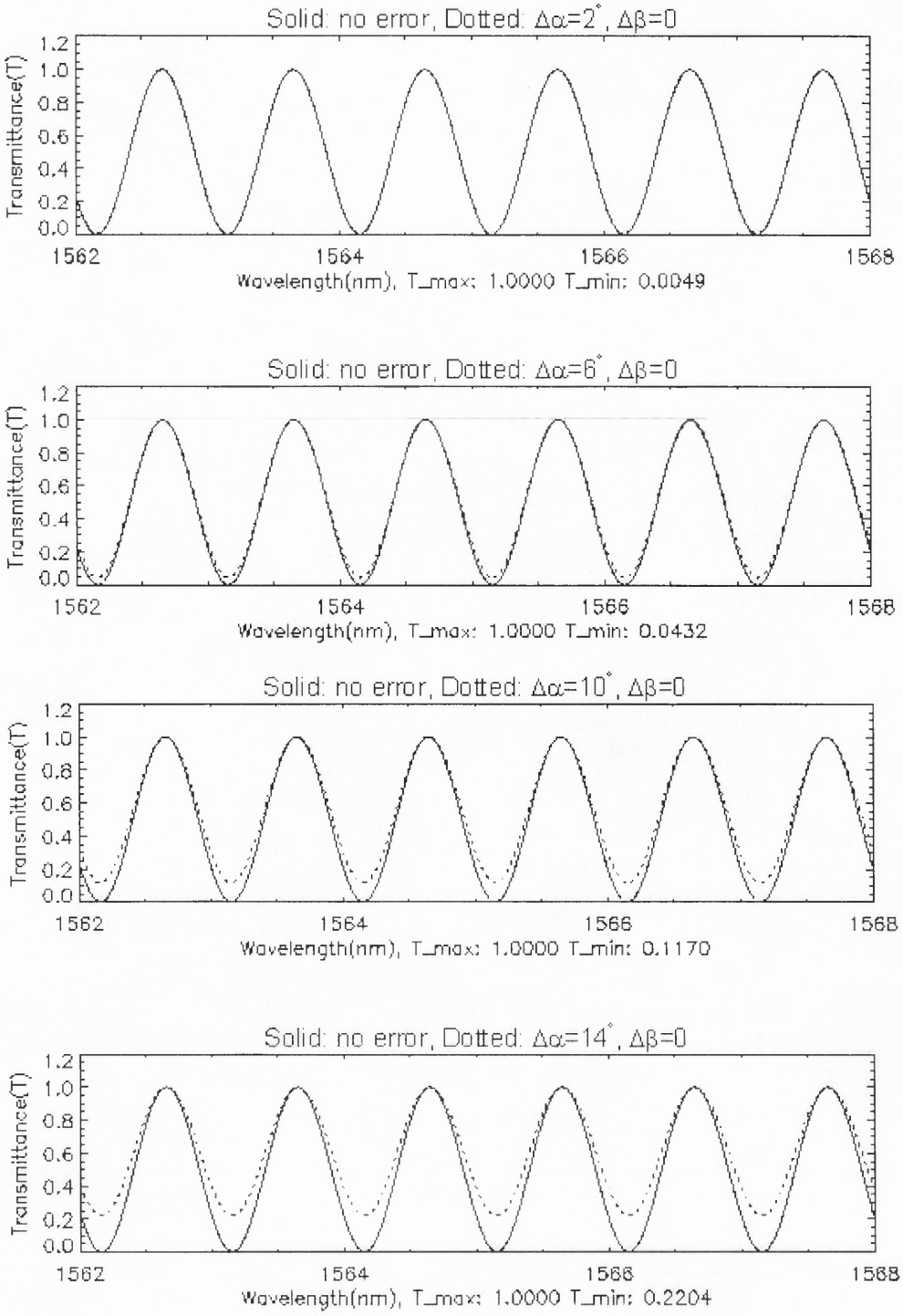

Figure B.4 Numerical modeling of transmittance of an element with $\Delta\alpha \neq 0$, $\Delta\beta = 0$. Solid line: no error, dashed line: error with $\Delta\alpha$.

REFERENCES

1. J. T. Schmeltz and J. C. Brown, "The Sun: A Laboratory for Astrophysics", Kluwer Academic Publishers, 1992.

2. H. Lin, "On the distribution of the solar magnetic fields," Astrophys. J., vol. **446**, pp. 421-430, 1995.

3. D. Rabin, "Spatially extended measurements of magnetic field strength in solar plages," Astrophys. J., vol. **391**, pp. 832-844, 1992.

4. D. Rabin, "A true-field magnetogram in a solar plage region," Astrophys. J., vol. **390**, pp. L103-L106, 1992.

5. S. K. Solanki, I. Rnedi and W. Livinston, "Infrared lines as probes of solar magnetic features. II - Diagnostic capabilities of Fe I 15648.5 Å and 15652.9 Å," Astron. Astrophys., vol. **263**, pp. 312-322, 1992.

6. Max Born and Emil Wolf, "Principles of Optics", Pergamon Press, 1980.

7. D. T. Runkle, "Optical assembly", October 24, 1999. Retrieved April 6, 2001 from the World Wide Web: http://www.astrorat.com/amateur/equipment/optical_assembly.htm.

8. Harold Zirin, "Astrophysics of the Sun", Cambridge University Press, 1989.

9. B. Lyot, Comptes Rendus, vol. **197**, pp.1593, 1933.

10. B. Lyot, "The Birefringent filter and its applications in solar physics", Ann. Astrophys., vol. **7**, pp. 31, 1944.

11. Y. Öhman, "A new monochromator", Nature, vol. **141**, No. 3560, pp. 157, 1938; Nature, vol. **141**, No. 3563, pp. 291, 1938.

12. J. W. Evans, "The birefringent filter", J. Opt. Soc. Am., vol. **39**, pp. 229-242, 1949.

13. Ivan Solc, "Chain birefringent filters", J. Opt. Soc. Am., vol. **39**, pp.612, 1949.

14. J. W. Evans, "Solc birefringent filter", J. Opt. Soc. Am., vol. **39**, 1958.

15. J. M. Beckers, L. Dickson, and R. S. Joyce, "A fully tunable Lyot-Öhman filter", AFCRL-TR-75-0090, 1975.

16. G. Ai and Y. Hu, "Multi-channel birefringent filter. I --- Principle and video spectrograph", Acta Astrophysica Sinica, vol. **7**, pp. 305, 1991.

17. G. Ai and Y. Hu, "Multi-channel birefringent filter. II --- The total transmission filter", Acta Astrophysica Sinica, vol. **7**, pp. 316, 1991.

18. Jingshan Wang, G. Ai, F. He, Y. Deng, Weijun Mao, G. Song, Bin Zhang, X. Ye, "Solar multi-channel birefringent filter", Optical Technology, Supplement, pp. 41 1995.

19. D. Bonaccini, F. Cavallini, G. Ceppatelli and A. Righini, "High resolution solar bidimensional spectroscopy with a Universal Birefringent Filter in tandem with a Fabry-Perot interferometer," Astron. Astrophys., vol. **217**, pp. 368-374, 1989.

20. D. Bonaccini and F. Stauffer, "High resolution solar bidimensional spectroscopy with a Universal Birefringent Filter in tandem with a Fabry-Perot interferometer: tests and experimental results," Astron. Astrophys., vol. **229**, pp. 272-278, 1990.

21. C. A. Gullixson, S. L. Keil and K.S. Balasubramaniam, "Design considerations for a near infrared imaging vector magnetograph," HO-755-96, 1996.

22. Craig A. Gullixson, "Characteristics of available Fabry-Perot filters", Technical Memorandum of NSO/SP, April 15, 1998.

23. Jingshan Wang, Haimin Wang, T. Spirock, Chik-Yin Lee, N. M. Ravindra, Jun Ma, P. R. Goode and C. Denker, "Optical design of a near-infrared birefringent filter system and measurement of birefringent index of calcite at 1.56μm", Optical Engineering, vol. **42**, no. 6, 2001, in press.

24. G. E. Hale, "The 150-Foot Tower Telescope of the Mount Wilson Solar Observatory", Pub. A.S.P., vol. **24**, pp.223, 1912.

25. George E. Hale, F. Ellerman, S. B. Nicholson and A. H. Joy, "The magnetic polarity of sun-spots", Astrophys. J., vol. **49**, pp.153, 1919.

26. George E. Hale and S. B. Nicholson, "The law of sun-spot polarity", Astrophys. J., vol. **62**, pp.270, 1925.

27. H. W. Babcock, "The solar magnetograph", Astrophys. J., vol. **118**, pp.387, 1953.

28. H. W. Babcock and H. D. Babcock, "The Sun's magnetic field, 1952-1954", Astrophys. J., vol. **121**, pp.349, 1955.

29. R.C. Smithson, "Videomagnetograph studies of solar magnetic fields I: Magnetic field diffusion in weak plage regions", Solar Physics, vol. **29**, pp. 365, 1973.

30. Jingshan Wang, Guoxiang Ai, Yuanyong Deng: "Determination of the crystal elements' orientation arrangement in wavelength-tunable birefringent filter", Acta Astrophysica Sinica, vol. **11**, pp. 383, 1991.

31. Jingshan Wang, Haimin Wang, T. Spirock, Chik-yin Lee, N. M. Ravindra, Jun Ma, Philip R. Goode and Carsten Denker, "Optical design of a near-infrared birefringent filter system and measurement on birefringent index of calcite at 1.56μm", Proceedings of SPIE's 45th Annual Meeting, vol. **4093B**, pp. 481-489, 2000.

32. Jingshan Wang, Guoxiang Ai, Guofeng Song, Bin Zhang, Xiangming Ye, Y. Nie, T. Chieveh, W. Tsay and H. Li, "Universal birefringent filter with a new double passband mode", Solar Physics, vol. **161**, pp. 229-239, 1995.

33. M. Bass, E. W. Van Stryland, D. R. Williams and W. L. Wolf, *Handbook of Optics*, 2nd ed., McGraw-Hill, Inc., pp. 33.52-33.70, 1995.

34. Walter G. Driscoll and William Vaughan, *Handbook of Optics*, McGraw-Hill, Inc., pp. 7-78, 1995.

35. Jun Ma, "Mechanical design of the heater used in near infrared filter", Thesis of Master Degree, New Jersey Institute of Technology, 2000.

36. T. J. Spirock, P. R. Goode and H. Wang, AGU Meeting, Boston, SH52H-01, 1998.

37. L. Delbouille, G. Roland, et al, (1981), "High resolution solar spectrum", http://mesola.obspm.fr/form_spectre.html.

38. Alen M. Title, "Improvement of birefringent filter I: Reduction of scatter in polaroid materials", Solar Physics, vol. **33**, pp.521-523, 1973.

39. "User's Guide of Queensgate Servo-Stabilized Interferimeter System: CS100 Controller, ET Series II and EC Series Etalons", SDL Queensgate Ltd, 2000.

40. J. I. García de la Rosa, in The Role of Fine-Scale Magnetic Fields on the Structure of the solar Atmosphere, ed. E. H. Schröter, M. Vázquez and A. A. Wyller, Cambridge Univ. Press, pp. 140, 1987.

41. M. Sobotka, J. A. Bonet and M. Vázquez, "A high-resolution study of inhomogeneities in sunspot umbrae", Astrophys. J., vol. **415**, pp.832-846, 1993.

42. U. Grossmann-Doerth, W. Schmidt and E. H. Schroeter, "Size and temperature of umbral dots", Astron. Astrophys., vol. **156**, pp. 347-353, 1986.

43. M. W. Ewell, "Near-infrared CCD observations of umbral dots", Solar Physics, vol. **137,** 215-223,1992.

44. E. Wiehr, "The height variation of sunspot umbral dots", Astron. Astrophys., vol. **287**, pp.L1-L4, 1994.

45. M. Sobotka, J. A. Bonet and M. Vázquez, "On the relation between the intensities of bright features and the local background in sunspot umbrae", Astron. Astrophys., vol. **257**, pp.757-762, 1992.

46. A. Adjabshirzadeh and S. Koutchmy, "Photometric analysis of sunspot umbral dots. III Spectrophotometry and preliminary model of a 2-component umbra", Astron. Astrophys., vol. **122**, pp.1-8, 1983.

47. E. Wiehr and D. Degenhardt, "The Evershed effect in penumbral fine structures II. Sptial correlation analysis", Astron. Astrophys., vol. **287**, pp.625-632, 1994.

48. K. D. Pahlke and E. Wiehr, "Magnetic field, relative Doppler shift and temperature for an inhomogeneous model of sunspot umbrae", Astron. Astrophys., vol. **228**, pp.246-256, 1990.

49. W. Schmidt and H. Balthasar, "Polarimetry and spectroscopy of a simple sunspot. 3: Velocity and magnetic field of sunspot umbral dots", Astron. Astrophys., vol. **283**, pp.241-246, 1994.

50. E. N. Parker, "Sunspots and the physics of magnetic flux tubes. IX - Umbral dots and longitudinal overstability", Astrophys. J., vol. **234**, pp.333-347, 1979.

51. A. R. Choudhurri, "The dynamics of magnetically trapped fluids. I - Implications for umbral dots and penumbral grains", Astrophys. J., vol. **302**, pp.809-825, 1986.

52. E. Knobloch and N. O. Weiss, "Convection in sunspots and the origin of umbral dots", Royal Astronomical Society, Monthly Notices, vol. **207**, pp.203-214, 1984.

53. D. Degenhardt and B. W. Lites, "The magnetohydrodynamics of umbral flux tubes. I - Theoretical model", Astrophys. J., vol. **404**, pp.383-393, 1993.

54. A. Ferriz-Maz, M. Schüssler and V. Anton, "Dynamics of magnetic flux concentrations - The second-order thin flux tube approximation", Astron. Astrophys., vol. **210**, pp.425-432, 1989.

55. T. J. Spirock, C. Denker, J. S. Wang, H. Chen, H. Wang and P. R. Goode, "New vectormagnetographs at the Big Bear Solar Observatory", American Astronomical Society Meeting 194, #**76.07**, Chicago, May, 1999.

56. R. Muller, "Étude morphologique et cinématique des structures fines d'une tache solaire", Solar Physics, vol. **29**, pp.55-73, 1973.

57. R. Muller, "Characteristics of the displacement of the penumbral bright grains of sunspots", Solar Physics, vol. **48**, pp.101, 1976.

58. K. Tönjes and H. Wöhl, "Motions and lifetimes of the penumbral bright grains in sunspots", Solar Physics, vol. **75**, pp. 63-69,1982.

59. H. Wang and H. Zirin, "Flows around sunspots and pores", Solar Physics, vol. **140**, pp. 41-54, 1992.

60. M. W. Ewell, "Near-infrared CCD observations of umbral dots", Solar Physics, vol. **137**, pp. 215-223, 1992.

61. R. Molowny-Horas, "Proper motion measurements of umbral and penumbral structure", Solar Physics, vol. **154**, pp. 29-39, 1994.

62. M. Sobotka, J. A. Bonet, M. Vázquez and A. Hanslmeier, "On the dynamics of bright features in sunspot umbrae", Astrophys. J., vol. **447**, pp.L133-L134, 1995.

63. J. H. Thomas and N. O. Weiss, in "Sunspots: Theory and Observations", ed. J. H. Thomas and N. O. Weiss, pp. 3, 1992.